

Summer 2017

Influence of Tides and Mesoscale Eddies in the Ross Sea

Stefanie Lynn Mack
Old Dominion University

Follow this and additional works at: https://digitalcommons.odu.edu/oeas_etds



Part of the [Oceanography Commons](#)

Recommended Citation

Mack, Stefanie L.. "Influence of Tides and Mesoscale Eddies in the Ross Sea" (2017). Doctor of Philosophy (PhD), dissertation, Ocean/Earth/Atmos Sciences, Old Dominion University, DOI: 10.25777/c0en-7b20
https://digitalcommons.odu.edu/oeas_etds/9

This Dissertation is brought to you for free and open access by the Ocean, Earth & Atmospheric Sciences at ODU Digital Commons. It has been accepted for inclusion in OEAS Theses and Dissertations by an authorized administrator of ODU Digital Commons. For more information, please contact digitalcommons@odu.edu.

**INFLUENCE OF TIDES AND MESOSCALE EDDIES IN THE
ROSS SEA**

by

Stefanie Lynn Mack
B.S. May 2010, Westminster College, PA

A Dissertation Submitted to the Faculty of
Old Dominion University in Partial Fulfillment of the
Requirements for the Degree of

DOCTOR OF PHILOSOPHY

OCEANOGRAPHY

OLD DOMINION UNIVERSITY
August 2017

Approved by:

John Klinck (Director)

Chet Grosch (Member)

Eileen Hofmann (Member)

Fang Hu (Member)

Dennis McGillicuddy (Member)

Laurie Padman (Member)

ABSTRACT

INFLUENCE OF TIDES AND MESOSCALE EDDIES IN THE ROSS SEA

Stefanie Lynn Mack
Old Dominion University, 2017
Director: Dr. John Klinck

The Ross Sea is the most biologically productive region in the Southern Ocean. Primary production is controlled by dissolved iron (dFe), a limiting micronutrient. The main focus of this thesis, motivated by the PRISM-RS project, is to investigate how tides and mesoscale eddies affect the pathways of dFe to the surface ocean.

A regional ocean model with four hindcast simulations are used. Tidal forcing is added to simulations and mesoscale eddies are resolved by changing the horizontal grid resolution from 5 to 1.5 km. Simulations cover 1.5 years, ending at the time of the PRISM-RS cruise in early 2012. An extended 20 year simulation provides an estimate of model variability and significance. The model is validated using hydrographic data from the PRISM-RS cruise and climatological values of water mass volumes. Compared to observations, simulations show a salinity offset at depth, that can be attributed to freshening of the Ross Sea in recent years. The model represents water mass volumes well, but has a reduced amount of Ice Shelf Water. Analysis of eddy formation in the model indicates that the weak stratification produces small and short-lived mesoscale eddies in the Ross Sea. The increased resolution approximately doubles the number of eddies seen in one year of simulation and significantly increases the baroclinic eddy kinetic energy.

The effect of tidal forcing on sea ice is investigated using a new method to extract a diurnal signal from satellite swath data. In the northwest corner of the Ross Sea continental shelf, strong tidal divergence causes the sea ice to decrease by 20% in winter. Simulation results show a strong heat flux that generates sea ice during spring tide conditions.

The supply of dFe in simulations is calculated using four passive tracer dyes representing sources of dFe: sea ice, glacial ice, Circumpolar Deep Water, and benthic supply. The simulation without tides at 5 km resolution estimates the total supply of dFe to the surface at $6.63 \mu\text{mol m}^{-2} \text{ yr}^{-1}$. Tides increase this by 20%, eddies decrease it by 15%, and the net change from both is not significant. Spatially, the pattern of dFe supply varies significantly between all simulations.

Copyright, 2017, by Stefanie Lynn Mack, All Rights Reserved.

To my sidekick,
who spent as much effort supporting me as I did writing this.

ACKNOWLEDGMENTS

For a document with a single author, there are a significant number of people who helpfully contributed to this dissertation. It would not be the same without you.

My thanks to my advisor and committee members, for guiding my research and helping refine my thesis; the Antarctic modeling research group, esp. Mike, for hashing out the every day research issues with me; Scott and Susan from ESR for additional modeling expertise; and the PRISM-RS project group for supplying a broader context to my work and being a great example of collaborative research.

Thanks also go to those who contributed to my growth as a scientist: the faculty and staff at OEAS, fellow graduate students at ODU and in the larger oceanography community, and some pretty awesome postdocs.

Finally, thanks to Julia for helping me push through the final stretch.

The data used in this paper from the PRISM-RS project are archived at the Biological and Chemical Oceanography Data Management Office: www.bco-dmo.org/project/2155. The research presented in this thesis was funded by NSF's Antarctic Research Program (ANT-0944174) and NASA grant NNX08AN676, and was supported by the Turing High Performance Computing Cluster at Old Dominion University.

TABLE OF CONTENTS

	Page
LIST OF TABLES	ix
LIST OF FIGURES.....	xiv
1. INTRODUCTION	1
1.1 CONTEXT	3
1.2 RESEARCH OBJECTIVES	12
Chapter	
2. METHODS.....	14
2.1 INTRODUCTION	14
2.2 OBSERVATIONS	14
2.3 MODEL DETAILS	17
2.4 MODEL DRIFT	24
2.5 MODEL ANALYSIS TOOLS	26
2.6 CONCLUSION.....	31
3. MODEL VALIDATION.....	32
3.1 INTRODUCTION	32
3.2 METHODS	32
3.3 RESULTS AND DISCUSSION	34
3.4 CONCLUSION.....	42
4. MESOSCALE EDDIES.....	45
4.1 INTRODUCTION	45
4.2 EDDY THEORY	46
4.3 METHODS	55
4.4 RESULTS AND DISCUSSION	58
4.5 CONCLUSION.....	66
5. SEA ICE & TIDES.....	68
5.1 INTRODUCTION	68
5.2 DATA AND METHODS	70
5.3 RESULTS AND DISCUSSION	76
5.4 CONCLUSION.....	81
6. IRON TRANSPORT PATHWAYS.....	83
6.1 INTRODUCTION	83
6.2 METHODS	84
6.3 RESULTS	88

6.4 DISCUSSION & CONCLUSIONS	101
7. CONCLUSION	106
7.1 SYNTHESIS OF STUDIES	106
7.2 SIGNIFICANCE OF RESULTS	107
7.3 IMPLICATIONS FOR FUTURE RESEARCH	109
REFERENCES	113
APPENDICES	
A. ACRONYMS & VARIABLES.....	127
A.1 VARIABLES	127
A.2 ACRONYMS & ABBREVIATIONS.....	128
B. GLOSSARY	131
B.1 OCEANOGRAPHIC TERMS	131
VITA	132

LIST OF TABLES

Table	Page
1 Definitions of continental Ross Sea water masses using neutral density(γ_n), temperature(θ), and salinity(S) restrictions. Adapted from <i>Orsi and Wiederwohl [2009]</i>	9
2 Relevant PRISM-RS cruise meta-data and approximate horizontal resolution. See Figure 3. T = Temperature; S = Salinity; F = Fluorescence; V = Velocity; W = Wind; I = Dissolved iron; LOPC = Laser Optical Plankton Counter	15
3 Details of simulations used. *Simulation S5 is a special case of 5 with repeat yearly forcing for 20 years.	23
4 Fit parameters and confidence intervals of Equation 1 for sea ice area (km^2 , cols 2-3) and sea ice volume (km^3 , cols 4-5). Parameter G is given as $\text{km}^2 \text{ yr}^{-1}$, or $\text{km}^3 \text{ yr}^{-1}$, respectively.	25
5 Radius of deformation minimum, maximum, and mean for August and February in km. Corresponds with Figure 14.	49
6 Amplitudes of major tidal harmonics at the test site centered on 72°S, 172.5°E in the northwest Ross Sea (see Figure 21 for location). Column 2 lists component periods in hours. Columns 3 and 4 give amplitudes for sea surface elevation and barotropic cross-slope tidal current, respectively, from the RossTIM barotropic tidal inverse model. Column 5 lists amplitudes of variability in C_{ice} from the present study. Column 6 is the tidal analysis of a synthetic signal created using O1 and K1 signals only, processed, and analyzed as described in Section 5.2. NS, nonsignificant.	71
7 Simulation-derived amplitudes of tidal harmonics O1 and K1 at the test site centered on 72°S, 172.5°E in the northwest Ross Sea (see Figure 21 for location). Column 2 lists component periods in hours. Columns 3-5 list amplitudes of variability in sea ice concentration, ice-ocean mass flux, and surface heat flux from T_Tide analysis. NS is not significant.	79
8 End member concentrations for model passive tracer dyes.	87
9 Average mixed layer depths (MLDs) on the continental shelf for January through February 2012 from simulations, PRISM-RS cruise data, and global climatologies [Kara <i>et al.</i> , 2003], given with standard deviations (Stdev). SSC for simulations is shown as the percentage SSC times the average MLD.	97

10	Total dFe in the SML for each simulation from each source on the continental shelf (inshore of 700 m, averaged over DJF). Units are $\mu\text{mol m}^{-2} \text{ yr}^{-1}$. Final row shows the total dFe supplied from each simulation.	102
----	---------------------------------------------------------------------------------------------------------------------------------------------------------------------------------------------------------------------------------------------------	-----

LIST OF FIGURES

Figure	Page
1 Map of the Ross Sea, Antarctica bathymetry. Black lines are bathymetry contours, gray line is the ice shelf front. CA: Cape Adare; CB: Crary Bank; IB: Iselin Bank; MB: Mawson Bank; PB: Pennell Bank; RB: Ross Bank; TNB: Terra Nova Bay.	4
2 Map of the Ross Sea and west Antarctic Peninsula showing large scale circulation patterns. ACC is Antarctic Circumpolar Current.	7
3 Domain for Ross Sea model (1.5 km resolution). Color bar is depth in meters. Black lines are bathymetry contours for 0, 200, 400, 600, 800, 1000, 2000, and 3000 meters. Thick gray line is the ice shelf edge. Red line is the PRISM-RS cruise track with CTD stations marked as dots.	16
4 Box plot showing the statistical distribution of the thickness in meters of the top(left) and bottom(right) model layers. Shelf break is defined as 700 meters.	19
5 Sea ice volume timeseries (black dots) from simulation S5 to test model drift. Blue line is a fit of an annual cycle, offset, and linear trend.	26
6 STL analysis of Ice Shelf basal melt rates over the 20 year simulation. From top to bottom: original signal (dots) with STL fit (line); nonlinear trend; annual cycle; sub-annual variability (residuals)	27
7 STL analysis of salt content(kg) on the continental shelf from the 20 year simulation. From top to bottom: original signal (dots) with STL fit (line); nonlinear trend; annual cycle; sub-annual variability (residuals)	28
8 Conservative Temperature and Absolute Salinity depth profiles from PRISM-RS CTD casts (gray lines). Thick solid lines are average profiles for CTD casts and simulations 5 and 5T	34
9 Differences between depth profiles from CTD and simulation 5 . Thick red line is the average difference. Positive values indicate simulation is warmer or saltier than observations.	36
10 Temperature-Salinity diagram. Gray points are sub-sampled on-shelf values from simulation 5 for Jan-Feb 2012. Darker gray indicates values under the ice shelf. Red points are PRISM-RS CTD measurements. Dashed contours are constant potential density lines, blue dashed line is freezing temperature at surface conditions.	37

11	Volume of water masses (km^3). Solid line is from simulation 5 ; dashed from 5T ; thin dash dot from <i>Orsi and Wiederwohl [2009]</i> . Note the scales in each panel change to better illustrate the variability of each.	39
12	Amount of dye_{CDW} on the continental shelf (inshore of 700 meter isobath) for simulation 5 , its distribution across water masses. Dye is given as dye units times volume, where dye units are treated as an arbitrary concentration. Date is given as month, year.	41
13	Fraction of dye_{CDW} on the continental shelf (inshore of 700 meters that is present in each water mass for simulation S5. Dates represent model years; forcing is repeated from the first year.	42
14	Radius of deformation (km) calculated from simulation 5 . Inset shows histogram of values over model domain. a) August 15, 2011. b) February 15, 2012.	50
14	Radius of deformation (km) calculated from simulation 5 . Inset shows histogram of values over model domain. a) August 15, 2011. b) February 15, 2012.	51
15	Diffusion time scales: Equation 5 plotted as a function of horizontal distance scaled by grid spacing (Δx) for 1.5 and 5 km grids.	54
16	Kinetic Energy (normalized by volume) for simulations 5 and 1 in February and August on the continental shelf. Solid lines are the KE from each component: overall total, barotropic, baroclinic, and the interaction term. Barotropic and baroclinic KE are further split into time mean (dashed) and time varying (dotted) portions.	59
17	The percent of total KE contained in each component (barotropic time mean KE; barotropic EKE; baroclinic time mean KE; baroclinic EKE) for simulations 5 and 1 averaged over August and February. Note that the interaction KE term contributes less than 0.02% for each and is not shown.	60
18	Map of eddy tracks during the last year of simulation for simulation 5 (a), and 1 (b). Black lines are bathymetry, gray line is ice shelf front.	62
19	Histograms of eddy characteristics for the last year of simulation for 5 (column A) and 1 (column B). Rows are: 1) Eddy radius (km); 2) Eddy height (cm); 3) Model day eddy first appeared; 4) Number of days the eddy persisted.	63
20	Eddies identified from the eddy tracking software (black contours) plotted over model variables (Sea Surface Height (SSH), in-situ density, and relative vorticity (scaled by coriolis parameter f)) for simulations 5 and 1 on February 15, 2012 . . .	65

21	Probability of non-exceedance of sea ice concentration (C_{ice}) in the Ross Sea for a threshold of $C_{ice} = 0.95$ for all AMSR-E daily-averaged data for April November inclusive, years 2002 - 2009. Data were processed with the NASA Team 2 algorithm [Markus and Cavalieri, 2009]. High values imply frequent occurrences of partial open water (leads or polynyas). White lines are 500, 1000, and 2000 m isobaths. The test site is indicated as a black box just to the east of Cape Adare, northwest Ross Sea.	69
22	Frequency of swath passes over the study location over the course of 1 year. The irregular satellite sampling leaves 12 consecutive hours unsampled.	70
23	Sea ice concentration (C_{ice}) and tidal properties for year 2004 for a site in the northwest Ross Sea east of Cape Adare; see Figure 21 for location. (a) Measured values of $C_{ice}(t)$ for each swath, spatially averaged in a 25 x 25 km box. Vertical thin lines show period for which tidal analysis was performed with T_Tide (see Table 6). Vertical thick lines demarcate time interval shown in (b)-(d). (b) Values of C_{ice} for each swath (dots), tidal contribution based on T_Tide fit (continuous light line), and tidal contribution associated with long-period tides (continuous heavy line). (c) Residual C_{ice} anomaly after removal of tidal fit. (d) Cross-slope velocity v (m s ⁻¹) evaluated with the RossTIM barotropic tidal inverse model [Erofeeva et al., 2005].	72
24	(top) Comparison of synthesized signal (O1+K1) with signal retrieved by our analysis procedure assuming data available at the actual times of C_{ice} acquisition (red dots) from the AMSR-E swath data set. (bottom) Comparison of daily averaged C_{ice} values for the same time series, computed as the 24-h running mean of the synthesized time series (black) and the daily average at the times of AMSR-E swath sampling (red).	73
25	Frequency distribution of amplitudes of (a) O1 and (b) K1 from 1000 Monte Carlo type simulations of noise-only time series that were randomly sampled from a normal distribution with a standard deviation of 0.1.	75
26	(left, top and middle) Phase and amplitude of C_{ice} variability for the O1 tidal constituent from T_Tide analysis of AMSR-E swath data in 25 x 25 km boxes. Boxes with a SNR<3 (determined by T_Tide) are not plotted. Amplitude has been scaled by 1.2 to account for signal reduction associated with interpolation of the irregular time series of swath data (see Table 6). (left, bottom) Amplitude of C_{ice} variability based on the barotropic inverse tide model RossTIM, using 25 x 25 km boxes to calculate horizontal divergence of O1 tidal currents ($\Delta_h \dot{u}_{ocean}$), and assuming free drift of sea-ice. Values < 0.005 are not plotted. (right) Same as left, but for K1 tidal constituent. In all panels, black contours are 500, 1000, and 2000 m isobaths.	78

27	Time series from simulations, averaged over the box shown in Figure 21. a) C_{ice} ; b) Surface heat flux (W m^{-2}), negative is out of the ocean; c) Ice-ocean mass flux (cm day^{-1}), positive values indicate sea ice formation; d) Sea surface height (meters) from 5T . For a,b,c) bold line is from simulation 5 , light line is simulation 5T	80
28	DFe measurements below 200 m from casts where bottom depth was greater than 400 m, given as a function of distance from the seafloor. Color bar is total water column depth in meters. Black line is exponential fit from Equation 17. Adapted from <i>Marsay et al. [2014]</i>	86
29	STL (Seasonal Trend using Loess) [<i>Cleveland et al., 1990</i>] decomposition of dye_{GM} from simulation S5 with annually repeating forcing. a) Dots are original time-series normalized by the maximum value, solid line is the fit (trend plus seasonal cycle). b) Non-linear trend. c) Seasonal cycle. d) Sub-annual variability.	89
30	Monthly snapshots of dye_{bdFe} in the bottom model layer for the last year of simulation 5 . Color bar is in dye units, where the dye was initialized at 100. Black lines are bathymetry contours, gray line is the ice shelf front. X/Y axes indicate simulation grid points.	90
31	Average amount (DJF) of benthic dye in bottom model layer. a) Results from simulation 5 ; b,c,d) Difference between simulation 5 and 5T, 1, 1T , respectively. Positive values indicate more dye in that simulation, negative values indicate less. Colorbar is in dye units; black lines are bathymetry; gray line is the ice shelf front. X/Y axes indicate simulation grid points from 5 km grid.	92
32	Monthly snapshots of dye_{bdFe} in the top model layer for the last year of simulation 5 . Colorbar is in dye units, where the dye is initialized at 100. Black lines are bathymetry contours, gray line is the ice shelf front. X/Y axes indicate simulation grid points. Note the color bar scale is different from Figure 30	93
33	Average amount (DJF) of benthic dye in surface model layer. a) Results from simulation 5 ; b, c, d) Difference between simulation 5 and 5T, 1, 1T , respectively. Positive values indicate more dye in that simulation, negative values indicate less. Colorbar is in dye units; black lines are bathymetry; gray line is the ice shelf front.	95
34	Average mixed layer depth for simulations for January/February. a) Background is simulation 5 ; dots are MLDs from PRISM-RS CTD stations. b, c, d) Differences between simulation 5 and 5T, 1, 1T , respectively. Positive values indicate increased MLD, negative indicate decreased.	96
35	Simulation mixed layer depth (MLD) from simulation 5 at CTD stations and times plotted against CTD observations of MLD. Colors indicate general area of observations.....	98

36	Box plot showing the distributions of wind speeds from PRISM-RS data and from ERA-Interim used to force the model.	98
37	Bar graph showing the contribution of each dFe source to the total amount in the SML on the continental shelf (inshore of 700 m). Units are moles dFe. Error bars are SSC. a) November, b) December, c) January, d) February.	100
38	Dissolved iron supply (nM) in the surface mixed layer on the continental shelf (inshore of 700 m) for January. a) Simulation 5 . b, c, d) Differences between simulation 5 and simulations 5T , 1 , 1T , respectively. Positive values indicate more dFe in the simulation, negative values indicate less.	102
39	Color indicates dominant source of surface layer dFe for January 2012 for simulations a) 5 , b) 5T , c) 1 , d) 1T . Speckled areas indicate that source provides at least 75% of dFe. Solid black lines are bathymetry; white line is ice shelf front.	103

CHAPTER 1

INTRODUCTION

The Ross Sea, a marginal sea bordering Antarctica (Figure 1), is home to an extensive ecosystem [Smith Jr. *et al.*, 2007] and is the most productive sector of the Southern Ocean [Arrigo *et al.*, 2008]. Primary production in the Ross Sea is controlled by light, which is directly related to the seasonal cycle and sea ice coverage, and by the availability of dissolved iron (dFe) [Sedwick *et al.*, 2000]. As a limiting micronutrient, dFe availability in the surface waters of the Ross Sea when sea ice is not present determines the magnitude of the phytoplankton bloom, and consequently, the amount of biomass available to support higher trophic levels. Concentrations of dFe in the surface waters are controlled by the sources available in the Ross Sea, including ice melt, fluxes from sediments, remineralization from sinking organic matter, atmospheric deposition, and water masses originating outside the region (i.e., Circumpolar Deep Water (CDW)). The transport of dFe to the surface waters and the subsequent characteristics of the spring bloom are influenced by local physical processes, such as icebergs, sea ice melt, and eddies [Boyd *et al.*, 2012], and also by advection, diffusion, and mixing.

Future climate change in the Ross Sea may affect the physical processes that control the supply of dFe, and thus the entire ecosystem. Significant, recently observed changes to the Ross Sea climate include lengthening of the sea ice season [Stammerjohn *et al.*, 2008], increase in sea ice extent and net ice export [Comiso *et al.*, 2011], and freshening of the deep shelf waters [Jacobs *et al.*, 2002; Jacobs and Giulivi, 2010]. A projection of future changes to winds and atmospheric temperatures suggests that levels of primary production in the Ross Sea may increase by 2100 [Smith *et al.*, 2014] due to shallower summer mixed layers, but also estimates a decrease in the supply of dFe-rich CDW to the upper 50 m.

The uncertainty of the effect of climate change on the supply of dFe is due in part to the extreme conditions in the Ross Sea and the difficulty obtaining enough observations to fully characterize current physical processes. Observations are mostly restricted to the summer months, with limited or sparse observations during the winter. Satellites provide good spatial coverage of the surface (ocean or ice), but visual imagery is restricted during (frequent) times of cloud cover. Ship-based measurements obtain information at varying depths, but are restricted in horizontal range, frequency, and season. Moorings gather high

frequency vertical profiles in single locations, but lack horizontal coverage and encounter hazards from passing icebergs. Autonomous floats such as gliders are one way to obtain observations with fine horizontal and vertical detail, but they cannot transmit data and location information while under ice, limiting their use to the sea-ice free summer months. While there is a good variety of data available from these various methods, there is not a lot of detail known about processes at smaller length and time scales, particularly over the winter months.

One partial solution to address the issue of limited observations and understanding of processes is to use regional ocean modeling. The general objective is to fill in the details between sparse observations and to evaluate the effect of specific processes by turning them on and off in the model. Observations are used to initialize and provide information at the boundaries of the model, as well as to validate model output. In the interior of the model domain, the governing equations of fluid dynamics determine the behavior of the ocean, providing information at instances where there are no observations. While this theoretically fills in gaps in observations, especially at short time and small spatial scales, regional ocean models are not an exact representation of reality. The accuracy of the model can only be as good as the observations used to initialize and drive it, which are limited in this case. Computational costs and run time create the need to balance resolution in time and space with simulation length and model domain size. Higher spatial and temporal resolution simulations take longer to run and require more disk space to store. The specific details of the model, including domain size, resolution, and governing equations, determines which physical processes will be well represented.

The main objective of this thesis is to use a regional ocean model of the Ross Sea to investigate the role of physical processes on the supply of dFe. Specifically, I will look at the effect of tides and mesoscale eddies. Previous research has indicated that tides in the Ross Sea are important for mixing, dense water formation [*Padman et al.*, 2009], exchange of waters at the shelf break [*Wang et al.*, 2013] and melting of the ice shelf [*Arzeno et al.*, 2014]. Mesoscale eddies are not as well studied in the Ross Sea, but in general eddies influence vertical mixing [*McWilliams*, 2008] and often have a positive effect on primary production [*McGillicuddy Jr.*, 2016]. Both of these processes likely play an important role in the supply of dFe. Investigating their effects will help to better characterize the current state of dFe supply to the Ross Sea ecosystem and eventually allow us to make better predictions based on future climate change scenarios.

The structure of this thesis is as follows: The remainder of this chapter is devoted to a

more in-depth overview of the physical processes in the Ross Sea, the sources of dFe, and the state of current research in these areas. Chapter 2 describes the methods used, including observations from a recent cruise and the details of the regional ocean model design. Chapter 3 is a validation of the model with climatology using water mass analysis techniques. As mesoscale eddies are not well studied in the Ross Sea, Chapter 4 provides an overview of current theories as they apply to the Ross Sea and investigates how well the regional ocean model represents mesoscale eddies. Then, Chapter 5 takes an in-depth look at how tides influence sea ice, one of the potential sources of dFe. Chapter 6 addresses the main objective of this thesis: how tides and mesoscale eddies affect the supply of dFe. The final Chapter 7 summarizes and synthesizes the results of all the studies presented and comments on their significance as well as on directions for future research.

1.1 CONTEXT

1.1.1 IRON-LIMITED ECOSYSTEM

Ecosystem Structure

The Ross Sea is home to a unique and fragile ecosystem (See *Smith Jr. et al.* [2007] for a complete and comprehensive overview). Each spring, there is a significant phytoplankton bloom that starts in the Ross Sea Polynya and spreads to other areas as the sea ice melts and allows light to reach the surface ocean. Satellite estimates of primary production around the Southern Ocean show that the Ross Sea is the most productive sector (mean of 503 Tg C per year on the continental shelf), and also has the most interannual variability in peak production [*Arrigo et al.*, 2008]. The phytoplankton are dominated by diatoms and *Phaeocystis spp.*, which provide food for larger plankton, such as krill, a keystone species of the Ross Sea food web. These lower trophic levels support a variety of top predators, including penguins, seals, fish, birds, and whales.

Due in part to its location and extreme weather conditions, the Ross Sea ecosystem is considered the least impacted by humans globally [*Halpern et al.*, 2008]. This diagnosis led to recommendations from scientists to designate a Marine Protected Area (MPA) covering most of the Ross Sea, intended to preserve the ecosystem from disruption by human activities [*Ballard et al.*, 2012]. As a response, the members of the Commission for the Conservation of Antarctic Marine Living Resources (CCAMLR) voted to establish large portions of the Ross Sea as a MPA by December 2017 [CCAMLR, 2016]. The Ross Sea ecosystem is now

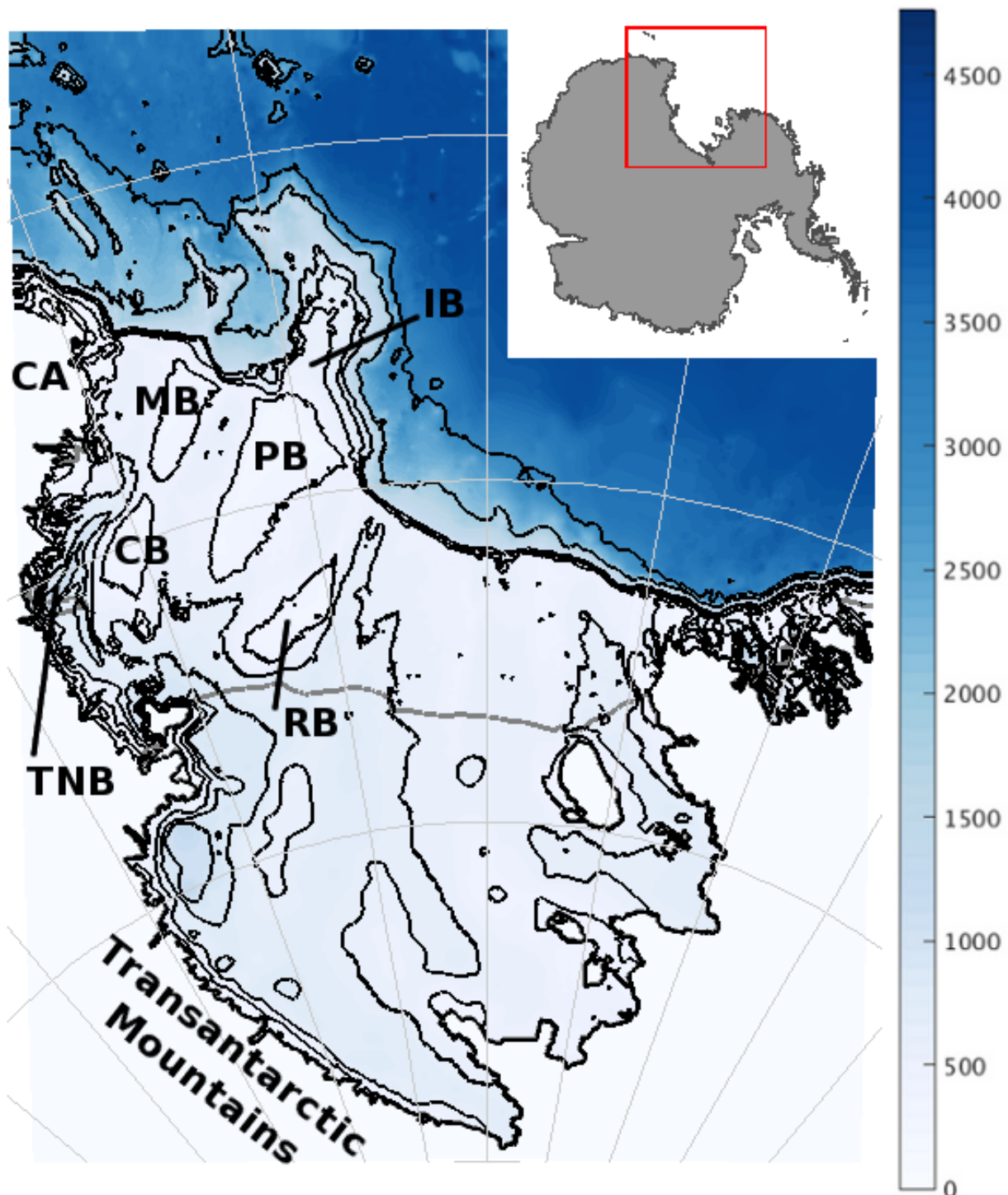


Figure 1. Map of the Ross Sea, Antarctica bathymetry. Black lines are bathymetry contours, gray line is the ice shelf front. CA: Cape Adare; CB: Crary Bank; IB: Iselin Bank; MB: Mawson Bank; PB: Pennell Bank; RB: Ross Bank; TNB: Terra Nova Bay.

well-protected from human interference, with the exception of non-local human induced climate change. Monitoring the ecosystem in the Ross Sea in the future will indicate how this particular system and other similar ones around Antarctica respond to climate change.

Iron Limitation

Iron limitation research in the Southern Ocean originated with the development of the "iron hypothesis" [Martin, 1990]: that productivity in the Southern Ocean is limited by iron availability, and the higher levels of dFe-containing atmospheric dust during the Last Glacial Maximum (about 25,000 years ago) indicate more primary production, more carbon storage in the ocean, and thus lower levels of CO₂ in the atmosphere. Originally designed as a way to explain higher CO₂ drawdown by phytoplankton and lower atmospheric levels, research following the publication of the iron hypothesis focused on determining if primary production in the Southern Ocean at present is limited by iron availability. Bottle enrichment experiments showed that when iron was added to bottles containing phytoplankton in seawater, primary production increased (e.g., by 2-10 times in Ross Sea samples [Martin *et al.*, 1990]). Larger scale experiments consisted of adding iron directly to the ocean in large patches, i.e., direct iron fertilization. These studies (e.g. Boyd *et al.* [2000]) confirmed that iron addition increased phytoplankton biomass and photosynthesis rates, but not necessarily the increased carbon export expected from the iron hypothesis. Other studies focused more on directly measuring the amount of iron available to phytoplankton and comparing it with the size and progression of the spring bloom. For example, in the Ross Sea, Sedwick *et al.* [2000] found that ambient concentrations of dFe are adequate for phytoplankton growth in spring and early summer, but low concentrations later limit growth. An excellent overview of iron limitation of primary production around the Southern Ocean is covered in Boyd [2002].

After this initial period of confirming that large portions of the Southern Ocean, including the Ross Sea, are iron limited, researchers began to focus on two specific aspects of iron limitation. The first is directly related to climate and to the second half of the iron hypothesis: whether or not increasing primary production through iron fertilization would also increase ocean carbon storage in the Southern Ocean. This aspect has direct implications for potential geoengineering projects: if adding iron to the Southern Ocean increases drawdown and storage of carbon from the atmosphere, then that is a way to partially reverse anthropogenic-driven climate change. However, as one group of researchers found using an ocean circulation model, even if iron fertilization increased carbon uptake and that carbon was exported to depth in the Southern Ocean, it will not necessarily stay there long enough

to have an impact on climate [*Robinson et al.*, 2014].

The second aspect of iron limitation research in the Southern Ocean is on the question of supply. Now that iron is widely accepted as a key factor limiting primary production in the Southern Ocean, the next issue to address is where the iron originates. Known sources of iron include terrestrial sources in dust and dirt that can be released into the ocean through melting of glacial ice that has scraped over rocks or through atmospheric deposition of dust onto sea ice that then melts. Sediments at the ocean floor may also contain iron, creating a potential supply from the ocean bottom. Water masses that originate in other locations not limited by iron are also a potential source. Finally, iron that is taken up by phytoplankton and is contained within organic matter can be remineralized and re-used. Around the Southern Ocean, these sources have varying impacts on primary production based on location and physical processes. *Boyd et al.* [2012] illustrates this by comparing maps of iron supply with primary production to examine where iron inputs are and how that does not necessarily match with where iron utilization by phytoplankton occurs. They note that the transport of dFe to the surface waters and the subsequent characteristics of the spring bloom are influenced by small scale local processes, including the presence of icebergs and mesoscale eddies.

1.1.2 PHYSICAL CHARACTERISTICS AND RELEVANT PROCESSES

All potential iron sources to the surface ocean are controlled by local physical ocean processes and source origin. In order to investigate how iron is supplied in the Ross Sea, it is necessary to establish the relative location of sources, and the physical processes that affect transport and total supply.

Circulation

The Ross Sea [*Smith et al.*, 2012] is adjacent to the Southern Ocean and bounded by the Antarctic continent to the South (Figure 2). It is characterized by a relatively deep continental shelf (average of 500 m) that shallows to the north to create a raised sill, after which the bottom depth increases down the continental slope reaching abyssal depths of 4000 m. To the north, in the open ocean portion of the Ross Sea, are the Ross Gyre and the Ross Gyre extension. The Ross Gyre is a cyclonic flow that, on its southern side, brings westward flowing waters from the adjacent Amundsen Sea towards the continental shelf, and on its northern side connects Ross Sea waters to the eastward flowing Antarctic Circumpolar Current (ACC). The Ross Gyre extension is technically the second cell of the double celled

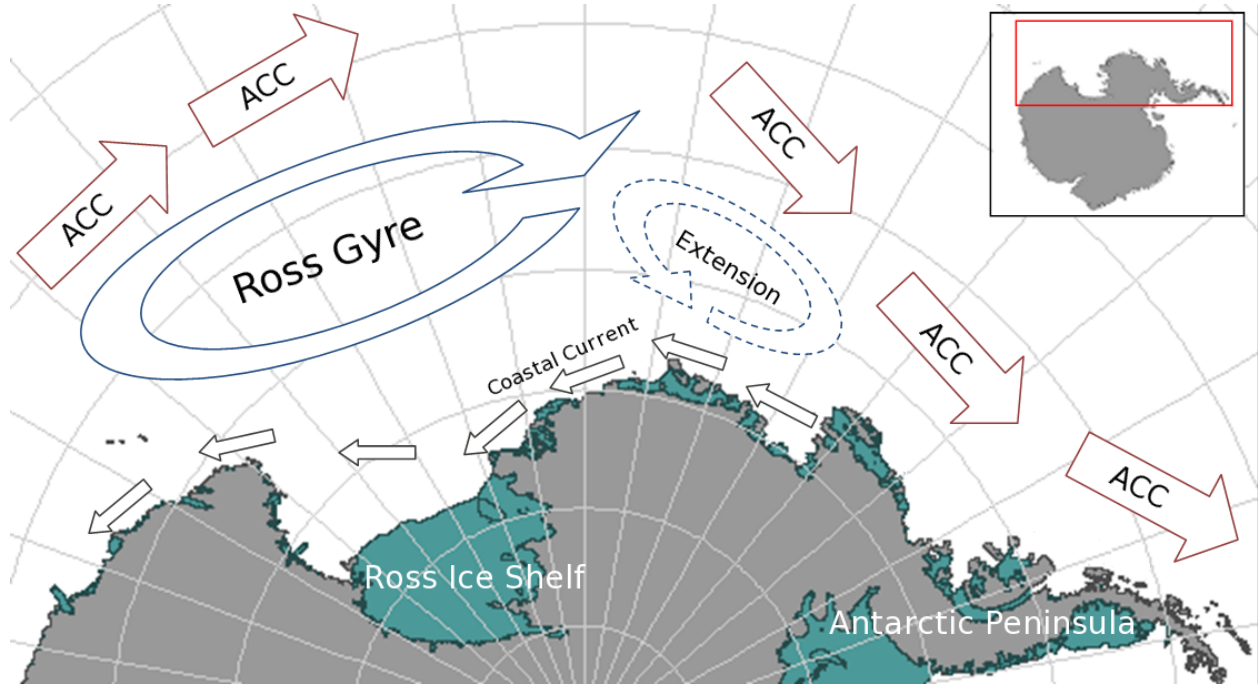


Figure 2. Map of the Ross Sea and west Antarctic Peninsula showing large scale circulation patterns. ACC is Antarctic Circumpolar Current.

Ross Gyre, having an anticyclonic flow, with about half the transport as the primary cell. Its western side coincides with the east edge of the Ross Gyre, and it is thought to extend as far as the West Antarctic Peninsula to the east [Locarnini, 1994]. The total transport and exact location of the Ross Gyre is still an open question, as only a few estimates from observations have been made [Assmann and Timmermann, 2005].

On the continental shelf, the westward flowing coastal current enters from the east and splits in two. Part of this current traces the outline of the shelf break at the surface, and the rest follows the front of the ice shelf and the western land boundary, where it merges into one current once more, exiting the Ross Sea to the northwest. Flows at mid and deeper depths consist mainly of northward flowing water from the continental shelf staying on the west side of bathymetric troughs and southward flowing water from off-shelf flowing in on the opposite side [Smith *et al.*, 2012]. Once the currents carrying shelf water northwards reach the shelf break, the water sinks and is carried westward by the coastal current and the lower portion of the Ross Gyre.

Ice processes

At the southern end of the Ross Sea lies the Ross Ice Shelf (Figure 1), a floating extension of the Antarctic Ice Sheet and the largest ice shelf in Antarctica. The adjacent continental shelf is considered a cold water shelf, as it is separated from the warmer waters in the ACC by the Ross Gyre as well as the width of the Ross continental shelf. Despite the contact with relatively cold water, the base of the Ross Ice Shelf still melts, though at less than 1 m yr^{-1} [Moholdt *et al.*, 2014], and is a source of cold, fresh water and dFe. Around the edges of the continental shelf, several other small ice shelves and glaciers protrude over ocean water, including Drygalski Tongue in the west by Terra Nova Bay.

For most of the year, the Ross Sea is covered by first year sea ice. During austral fall, increasingly cold air, brought by katabatic winds from the continent, causes sea ice to form over most of the open areas of the Ross Sea. As winter progresses, the katabatic winds, blowing seaward from the Transantarctic Mountains, push the sea ice away from the ice shelf front, allowing more ice to form. This constant formation of sea ice, and its associated brine rejection, contributes to the amount of dense water on the continental shelf and stimulates deep mixing. These winds initiate the formation of the Ross Sea Polynya [Bromwich *et al.*, 1993], an area of open water north of the ice shelf. The polynya opens and spreads northward, first by wind forcing, then from ice melt, until the majority of the Ross Sea is ice free for a few months in the summer. A similar effect is seen along the western coast, where smaller polynyas, such as the one in Terra Nova Bay, also open due to local wind forcing. The winds blowing from the continent, especially those that pass over ice-free land, also deposit dust containing iron on the sea ice, which is released into the water when the ice melts in austral summer.

Water Masses

The Ross Sea is one of the few locations around the Southern Ocean where Antarctic Bottom Water (AABW), the densest water mass in the ocean, is produced [Orsi *et al.*, 1999, 2002]. The Ross Sea version of AABW [Jacobs *et al.*, 1970], together with similar components from the Weddell Sea [Foldvik *et al.*, 1985] and other locations around Antarctica [Fukamachi *et al.*, 2010; Williams *et al.*, 2010; Ohshima *et al.*, 2013], descends to fill the bottom of the Southern Ocean and then flows northward as part of the lower limb of the meridional overturning circulation. This dense water mass is thought to be one of the drivers of global ocean circulation, yet its formation in and export from the Ross Sea depends on smaller

Water Mass	Neutral Density	Temperature	Salinity
AASW	$\gamma_n < 28.0$	All	All
(M)CDW	$28.0 < \gamma_n < 28.27$	All	All
MSW	$\gamma_n > 28.27$	$\theta > -1.85$	All
HSSW	$\gamma_n > 28.27$	$-1.95 < \theta < -1.85$	$S > 34.62$
LSSW	$\gamma_n > 28.27$	$-1.95 < \theta < -1.85$	$S < 34.62$
ISW	$\gamma_n > 28.27$	$\theta < -1.95$	All

Table 1. Definitions of continental Ross Sea water masses using neutral density(γ_n), temperature(θ), and salinity(S) restrictions. Adapted from *Orsi and Wiederwohl [2009]*.

scale, local processes [*Gordon et al., 2009; Padman et al., 2009*].

The dynamics of the Ross Sea, including sea ice formation processes, and its connection to the Ross Ice Shelf and the ACC determine the water masses (Table 1) that are formed. Specific definitions of these water masses use neutral density [*Jackett and McDougall, 1997*], temperature, and salinity to partition Ross Sea water into different types [*Orsi and Wiederwohl, 2009*]. Ice Shelf Water (ISW) is formed when relatively warm ocean water melts the bottom of the Ross Ice Shelf. ISW is extremely cold, below the freezing point of sea water at the surface (due to the increased pressure underneath the ice shelf), fresh, and a source of dFe.

On the continental shelf, the formation of sea ice and associated brine rejection contributes to the formation of the salty, cold water at the bottom of the water column known as Shelf Water (SW). The combination of cold ISW and salt from sea ice formation makes SW the densest water mass on the continental shelf. It is separated into two main categories: High Salinity Shelf Water (HSSW), found on the western side of the Ross Sea where the sea ice formation rate is higher, and Low Salinity Shelf Water (LSSW), found in the east. HSSW is the water mass that cascades over the shelf break in the west, mixes with ambient waters on the way down, and becomes AABW.

Two other water masses act as end members for mixing in the Ross Sea, but are not solely created there. CDW is a relatively warm, salty, and nutrient rich (including dFe) water mass which intrudes onto the continental shelf at mid-depths after being brought close to the shelf break by the circulation of the Ross Gyre. Antarctic Surface Water (AASW) is a catchall definition for water that is less dense than shelf waters, and includes a range of temperatures and salinities affected by sea ice formation and melting, as well as surface heating and cooling. AASW is partly influenced by processes specific to the Ross Sea, but also is advected from the east by surface currents.

The remaining water mass types in the Ross Sea are defined as mixtures between AASW, SW, and CDW. Mixing between CDW and SW forms Modified Shelf Water (MSW) on the shelf, but if this mixing occurs specifically between CDW and HSSW on the continental slope, the resulting water mass is AABW. CDW also mixes with both AASW and SW, to form Modified Circumpolar Deep Water (MCDW). Technically, any CDW that makes it to the Ross Sea continental slope is considered MCDW, as it is already significantly colder and fresher than the CDW found in the ACC, although still warmer and saltier than the water masses on the continental shelf. It is, of course, possible for CDW to mix solely with AASW and not with SW. However, there is no defined intermediate water mass for this interaction; after a significant loss in salinity and temperature, it is simply classified as AASW. These intermediate water masses, MSW and MCDW, are useful in determining which water masses in the Ross Sea are mixing, and to what extent.

Tides

Tides are high frequency (periods of about half to one day) phenomena driven by gravitational forces from the Moon and Sun. In the Ross Sea, tides are primarily diurnal [*Johnson and van Woert, 2006; Erofeeva et al., 2005*], and the main tidal components are O1 and K1, with periods of 25.82 h and 23.96 h, respectively [*Padman et al., 2009*]. Tidal velocities are strongest near the northwest continental shelf break, with speeds up to 1 m s^{-1} . Tides in this region are strongly bathymetrically controlled and change in intensity over features such as banks and the ice shelf front. Because of this topographic control, tidal currents can change substantially over length scales of 10-100 km. Previous studies have demonstrated that tides play a key role in the production of AABW, by keeping the dense bottom layer intact, and by sloshing this dense water over the shelf break [*Guan et al., 2009; Muench et al., 2009; Ou et al., 2009; Padman et al., 2009*]. An increased flow off the shelf break from tides implies an increased flow on-shelf at a different depth or location, perhaps mixing more CDW onto the shelf [*Wang et al., 2013*]. At the surface near the shelf break, tidal divergence can significantly change sea ice concentrations in the winter [*Mack et al., 2013*]. Though weaker in the interior of the Ross Sea continental shelf, tides increase local mixing in the water column, and are thought to play a role in ice shelf processes, including melting [*MacAyeal, 1984, 1985; Makinson et al., 2011; Arzeno et al., 2014*].

Tides have the potential to affect several different sources of dFe, and are one of the main foci of this thesis. Their role in the shelf-break exchange of water, including dFe-rich CDW, may influence the amount of dFe for the spring phytoplankton bloom. Likewise, by increasing

vertical mixing in the water column, tides can increase the amount of dFe supplied from deep waters, including input from sediments, deep remineralization, and waters containing ISW or CDW. Finally, as tidal rectification increases the melt rate of the Ross Ice Shelf, it can increase the amount of dFe supplied from ISW. Overall, tidally-influenced processes in the Ross Sea are expected to increase the amount of dFe available in the surface ocean.

Mesoscale Eddies

Mesoscale eddies are a small length scale process and typically persist for weeks to months, although observations of eddies in the Ross Sea are sparse. Eddy size is characterized by the baroclinic Rossby radius of deformation, which is the ratio of the long gravity wave speed to the Coriolis frequency. The size of eddies depends on the total depth of the water column, density variations with depth, and latitude. For summer conditions on stratified Antarctic continental shelves, eddy radii are estimated to range between 3-6 km. A more in depth analysis of expected eddy size and duration in the Ross Sea is presented in Chapter 4.

Eddies are formed from instabilities that take energy from a fast moving laterally and/or vertically shear flow. Perturbations from surface forcing or flow interaction with local bathymetry, land boundaries, or ice shelf fronts can initiate eddy formation. Eddies can be either barotropic, where the eddy extends over the entire water column, or baroclinic, confined to specific density layers. In general, baroclinic eddies are smaller than barotropic, and are often the type considered when looking at the mesoscale.

Eddies stir nearby waters, cause local upwelling and downwelling, and trap water in their center while moving, leading to a variety of impacts on larger time and space scales than the eddies themselves. There is some documentation that eddies along the ACC transport water properties across fronts [*Phillips and Rintoul*, 2000] and are responsible for increasing mixing of warmer CDW up onto the continental shelf [*Moffat et al.*, 2009; *Nøst et al.*, 2011; *Zhang et al.*, 2011; *Martinson and McKee*, 2012]. Eddies have also been found to be localized areas of enhanced primary production (“hot spots”) by bringing deep nutrient rich water to the surface [*Smith et al.*, 1996; *Kahru et al.*, 2007]. Eddy processes on Southern Ocean continental shelves have not been deeply studied, but simulation results indicate the need for models to properly resolve mesoscale eddies in order to capture certain relevant processes and interactions [*St-Laurent et al.*, 2013].

Mesoscale eddies are the other main focus of this thesis. In most other parts of the world ocean, eddies locally increase primary production by bringing nutrient rich waters to the surface. They also act to re-stratify the water column, keeping phytoplankton near the

surface and increasing light availability (see *McGillicuddy Jr.* [2016] for a comprehensive overview of eddy dynamics and primary production). Only in eastern boundary current systems have eddies been found to decrease primary production, mainly by transporting nutrients away from the coast towards the open ocean [*Gruber et al.*, 2011]. It is likely that mesoscale eddies in the Ross Sea will work to increase primary production, by increasing the amount of dFe supplied from deep sources, including sediment sources and dense waters below the surface. Likewise, by re-stratifying the water column, they will tend to keep dFe from sea ice melt in the surface ocean where it is available for uptake by phytoplankton.

1.2 RESEARCH OBJECTIVES

The primary objective of this thesis is to investigate the effect of tides and mesoscale eddies on the supply of dFe from various sources in the Ross Sea by regional ocean modeling. Previous research has established that dFe is a limiting micronutrient in the Ross Sea, and, together with light availability, controls the amount of primary production and influences the availability of food for higher trophic levels [*Sedwick et al.*, 2011]. Current research is focused on determining what the primary sources of dFe are in various parts of the Ross Sea, including over Mawson and Pennell Bank [*Hatta et al.*, 2016], in the Ross Sea polynya [*Gerringa et al.*, 2015], and over large parts of the western and central continental shelf [*McGillicuddy et al.*, 2015]. A modeling study of the transport of iron from its various sources to the surface mixed layer over the course of a year will illuminate the effect various physical processes have on iron supply in the Ross Sea.

To address the question of iron supply, this thesis analyzes dynamical processes associated with tides and mesoscale eddies. Tides are a well understood phenomenon, and as early as 1898, observations indicated that sea ice coverage is influenced by the tidal cycle [*Nansen*, 1898]. As sea ice is a source of dFe, this connection is further investigated in the Ross Sea. Specifically, a new analysis method is developed and explained in Chapter 5 that measures the effect of tides on sea ice concentration using satellite observations and compares it with simulations.

Mesoscale eddies are less well-studied, particularly in the Ross Sea. Observations consist primarily of transects of individual eddies during cruises in the ice-free summer, and satellite color observations during rare ice and cloud free times. To further explore eddy dynamics in the Ross Sea, Chapter 4 uses theories of two dimensional turbulence to predict typical eddy characteristics, and investigates how well these eddies are represented in a regional ocean model.

These three main studies - eddy dynamics, tide effects on sea ice concentration, and dFe supply - each use a regional ocean model. The design of this model is explained in a methods chapter (Chapter 2), which also covers the cruise data used to refine the model, long-term model stability, and a new method to estimate error when comparing simulations. Once the model set-up is explained, Chapter 3 presents the validation of the model, comparing simulations with recent cruise data as well as with a climatology of water mass volumes. Finally, Chapter 7 discusses the major results across all studies presented in this thesis, their significance to current research efforts, and the implications for future research directions.

CHAPTER 2

METHODS

2.1 INTRODUCTION

The main objective of this thesis is to answer the central question - how does dissolved iron reach the surface ocean in the Ross Sea, and what are the effects of tides and mesoscale eddies on iron pathways - using a regional ocean model complemented by observations. The ocean model provides a level of detail unavailable from observations alone, and the observations provide some measure of validating the model.

”All models are wrong, but some are useful” [Box and Draper, 1987] is a rather famous quote discussing statistical models. The general premise applies to ocean models as well: no model is an exact representation of reality and no model can say exactly what happened in the past or what will happen in the future. However, if designed correctly, model results can provide insight into physical processes, how they interact, and their relative magnitudes.

To answer the central question of this thesis, the ocean model needs to sufficiently represent reality at the time and spatial scales of interest. It should include key processes, specifically tides and mesoscale eddies, and also represent advection, diffusion, and mixing, as well as other physical processes, such ice melting and freezing. The model domain size needs to be sufficiently large to capture the region, but as small as reasonable, to not waste computation resources. Finally, the model must have appropriate initial conditions and input from the boundaries for the time it is running.

This chapter describes first the observations used to support this work, including a recent cruise to the Ross Sea with the Process Regulating Iron Supply at the Mesoscale - Ross Sea (PRISM-RS) project and climatological data of interest. Then the ocean model used in this work is detailed, including the model geometry, a coupled sea ice model, initial and boundary conditions, as well as modifications for tides and mesoscale eddies. The performance of the model is tested by running a much longer simulation to examine model behavior over time and quantify any model drift. Finally, I describe two tools used with the simulations: passive dye tracers to track individual water masses and iron sources, and a significance criterion developed to determine if two similar simulations are significantly different from one another.

Instrument	Resolution	Data Collected	Depth Range
Underway	500 m	T,S,F,V,W	Surface only
CTD	10-20 km	T,S,F,I	All
MVP	2-5 km	T,S,F,LOPC	10-300 m
VPR	1 km	T,S,F,images	10-150 m

Table 2. Relevant PRISM-RS cruise meta-data and approximate horizontal resolution. See Figure 3. T = Temperature; S = Salinity; F = Fluorescence; V = Velocity; W = Wind; I = Dissolved iron; LOPC = Laser Optical Plankton Counter

2.2 OBSERVATIONS

2.2.1 PRISM-RS CRUISE

The project Processes Regulating Iron Supply at the Mesoscale - Ross Sea (PRISM-RS) [McGillicuddy *et al.*, 2015] undertook an oceanographic cruise aboard RVIB Nathaniel B. Palmer from December 24, 2011 to February 28, 2012 (Figure 3). The purpose of this project is to investigate the potential sources of iron during the spring bloom and to assess their roles in supporting the Ross Sea ecosystem. To this end, the cruise focused on hydrographic and trace metal measurements (Table 2), along with biological surveys of phytoplankton processes, and surveyed portions of the continental shelf in the western half of the Ross Sea. Specifically, the data collected included temperature and salinity measurements from a variety of instruments including CTD casts, the ship's underway system, and a Moving Vessel Profiler (MVP). Iron measurements were made in samples collected using a trace metal CTD and towfish underway system. A towed Video Plankton Recorder (VPR) was used to collect information on phytoplankton distributions.

Observations from this cruise are used to support and verify results from the regional ocean model in a variety of ways. Temperature and salinity vertical profiles are used to calculate mixed layer depth (MLD) and compared with model estimates of MLD. Wind velocity and direction from the ship's underway system is compared with the larger scale smoothed atmospheric reanalysis data used to force the model. Dissolved iron (dFe) measurements from the trace metal CTD samples [Marsay *et al.*, 2014] are used to estimate the concentration of dFe in waters at the sea floor and subsequently estimate the amount of dFe that reaches the surface ocean by vertical mixing. These direct model-observation comparisons are detailed as part of Chapter 6.

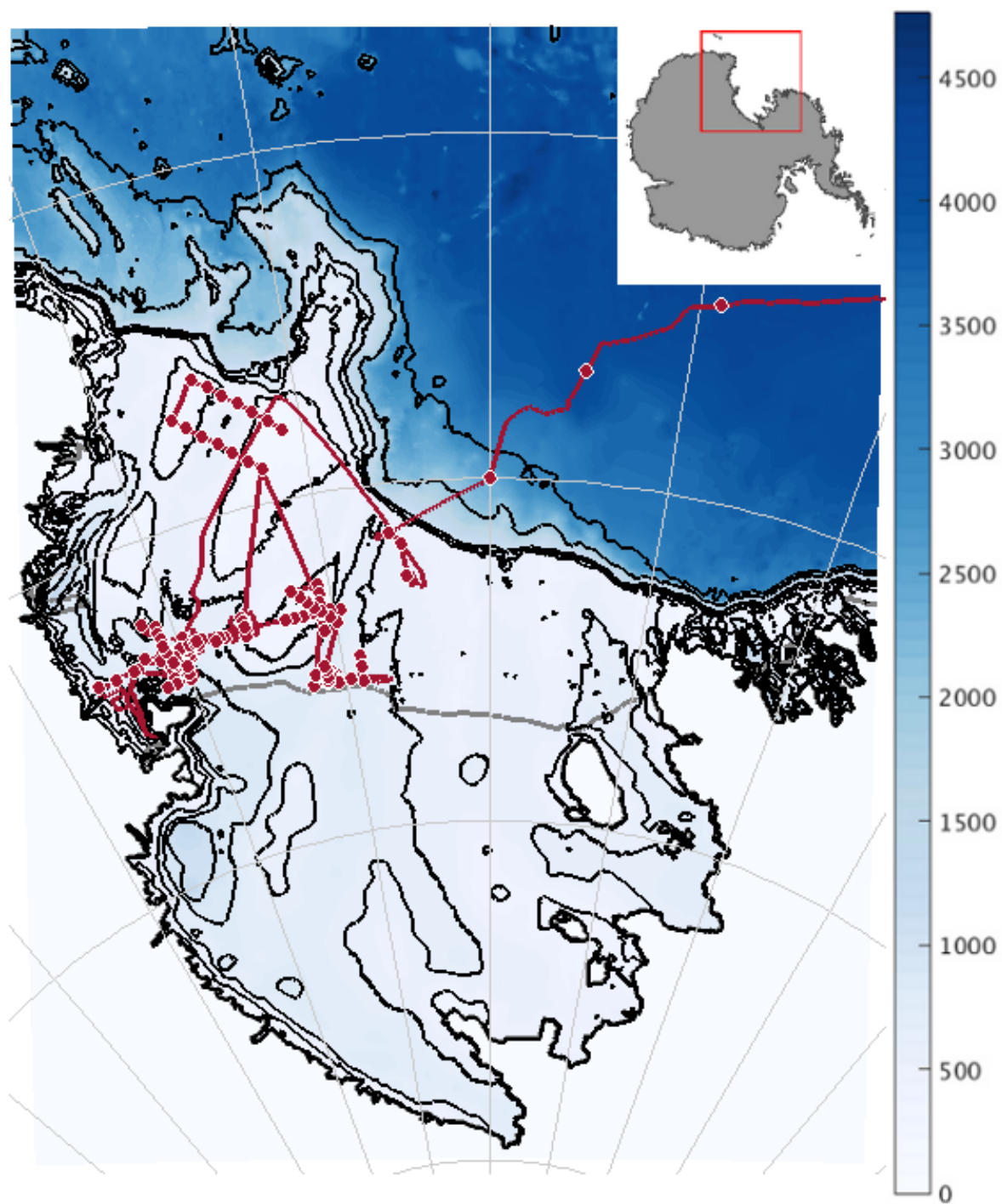


Figure 3. Domain for Ross Sea model (1.5 km resolution). Color bar is depth in meters. Black lines are bathymetry contours for 0, 200, 400, 600, 800, 1000, 2000, and 3000 meters. Thick gray line is the ice shelf edge. Red line is the PRISM-RS cruise track with CTD stations marked as dots.

2.2.2 OTHER OBSERVATIONS

Two other sets of observations are used in this thesis to compare with model results. The first is a series of hydrographic measurements from 1976 through 2004. *Orsi and Wiederwohl [2009]* used this collection of temperature and salinity data to estimate the volume of various water masses, each defined by specific temperature and salinity ranges, on the Ross Sea continental shelf. These data provide an estimate of the conditions in the Ross Sea averaged over decades. Most relevant to this study, the distribution of water into specific temperature and salinity bins is affected by many of the physical processes in the Ross Sea, including ice melt and freezing rates, mixing between water masses, advection and diffusion of water masses, and the influence of boundary forcing. Thus, comparing the volume distribution of water masses in simulations with this climatology is a way to validate the overall behavior of the model. This model validation is the main subject of Chapter 3.

The last set of observations used are passive microwave satellite data of sea ice concentration (percent cover of sea ice in a grid cell). These observations make up the core of Chapter 5, where a new analysis method is developed to extract tidal frequencies from satellite data. The results of this analysis provide an estimate of the variability in sea ice concentration that is due to tidal forcing. Sea ice behavior in the model is compared with the satellite record and the results of tidal forcing of sea ice are explored further, including increased ice production in areas with strong tides.

2.3 MODEL DETAILS

2.3.1 THE REGIONAL OCEAN MODELING SYSTEM

The ocean model used in this thesis is the Regional Ocean Modeling System (ROMS) framework, a complex code freely available for download and use by the scientific community since around 2002 (see myroms.org). ROMS is a hydrostatic primitive equation ocean model that uses finite differencing schemes and a split time stepping scheme with a predictor corrector algorithm. The ROMS grid is relatively uniform in the horizontal, with each grid box the same size, and uses a land mask to differentiate between open ocean and land grid points. In the vertical, ROMS uses terrain-following levels, also referred to as sigma coordinates. Regardless of ocean depth, each grid cell has the same number of vertical layers that are stretched or compressed as a function of depth. This allows for higher resolution near the surface or bottom and lower resolution at mid-depth as required. The benefit to

the sigma coordinate system is that it uses less computational resources to obtain similar resolution where it matters than models with evenly spaced vertical levels (z-levels). It also tends to do a better job resolving dense flows that follow bottom bathymetry, especially down steep slopes. However, it can introduce pressure gradient errors, as two grid cells that are horizontally adjacent may be at different depths, and horizontal exchange between the two would introduce a vertical component. ROMS is designed to minimize this error, but it may still be an issue at abrupt changes in bathymetry, such as an ice shelf front.

One of the benefits to ROMS is the large array of options, configurations, and coupled models available. In this application, ROMS is configured to use relatively high order schemes for the advection of momentum and tracers: third order upstream in the horizontal and fourth order centered in the vertical. Vertical mixing of tracers and momentum is determined with the K-profile parameterization (KPP) scheme [*Large et al.*, 1994], with the option of a bottom boundary layer parameterization [*Durski*, 2004]. I also make use of a sea ice model and an ice shelf parameterization. It would be possible to expand the model configuration described below to couple an atmospheric or biological model, to change the mixing or advection scheme, or to nest a smaller grid within the base grid, among other options. The choice to activate features of ROMS mainly stems from the specific application goals, as well as a cost benefit analysis weighing computational resources against impact.

2.3.2 ROSS SEA MODEL CONFIGURATION

Model Geometry

The Ross Sea model configuration was originally developed by Mike Dinniman and co-authors [*Dinniman et al.*, 2015, 2011, 2007, 2003], and has been used to support several recent studies related to this work [*Marsay et al.*, 2014; *McGillicuddy et al.*, 2015; *Kustka et al.*, 2015]. The model domain includes the cavity under the Ross Ice Shelf, the continental shelf and slope region, and portions of the abyssal Ross Sea (Figure 3). From this version, the bathymetry and under ice shelf topography were updated using the International Bathymetry Chart of the Southern Ocean (IBCSO) [*Arndt et al.*, 2013] and Bedmap2 [*Fretwell et al.*, 2013], respectively, to more accurately reflect current knowledge. Both the bathymetry products were smoothed, first with a Shapiro filter and then by hand, to eliminate pressure gradient force errors in regions with steep changes in bathymetry or topography with respect to the total depth. This includes a shallowing of the ice shelf draft along the ice shelf front.

Next the sigma coordinate system is modified and adjusted to represent processes of

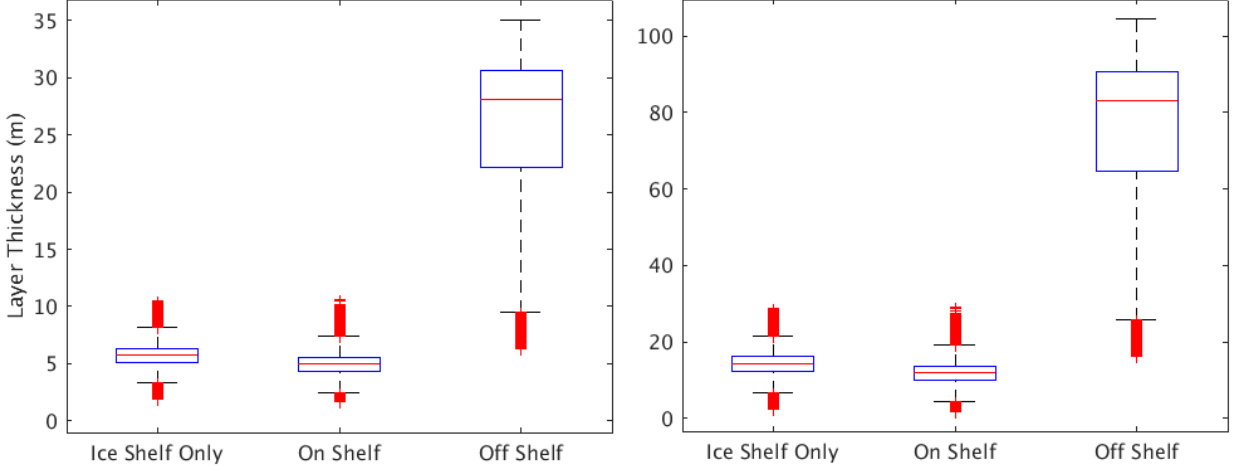


Figure 4. Box plot showing the statistical distribution of the thickness in meters of the top(left) and bottom(right) model layers. Shelf break is defined as 700 meters.

interest in the water column without introducing large pressure gradient errors. Specifically, the layers need to be clustered at the surface and bottom to resolve the vertical variations near the ocean boundaries. The surface mixed layer determines what water is directly influenced by exchange with the atmosphere or ice shelf base, while the bottom mixed layer defines in part the amount of Antarctic Bottom Water (AABW) that is exported. Previous work gives a variety of answers, few based on observations, for the thickness of the bottom and surface mixed layers in the Ross Sea, which vary seasonally. The bottom mixed layer near the shelf break can range from 68 to 484 meters thick [Muensch *et al.*, 2009]. In a model study using a similar ROMS configuration with 40 vertical layers, the bottom mixed layer on-shelf was found to range from 20 to 150 meters [Padman *et al.*, 2009]. Likewise, in another model study, the bottom mixed layer was found to range from 150 meters with tidal forcing to 30 meters without [Guan *et al.*, 2009]. Observations show that surface mixed layers in the Ross Sea are on the order of 100 meters, with smaller variations approximately 10 to 30 meters in scale [Jacobs *et al.*, 1970].

From this, the bottom-most model level should be no thicker than 20 meters, and the surface level no thicker than 10-30 meters to contain these mixed layers at their minimum thicknesses. The sigma coordinate system is set to have 24 vertical levels, using the original ROMS transformation equation and the stretching function defined in *Song and Haidvogel* [1994], with parameters $\Theta_s = 4$, $\Theta_b = 0.9$, and the critical depth set to 200 m. A statistical analysis of the thickness of the top and bottom model layer in this configuration shows

that grid points on the continental shelf (inshore of the 700 meter isobath) fall within these restrictions (Figure 4). Overall, the configuration is sufficient to resolve the mixed layers at both surface and bottom on the continental shelf. If this model configuration is to be used in future to examine surface or bottom layer processes off-shelf, or with a coupled biological model, the number of vertical levels needs to increase to provide the appropriate resolution, particularly at the surface for biological processes. However, an increase in vertical layers and surface resolution requires more lateral smoothing and a less abrupt ice shelf front.

Horizontal Grid Resolution

The issue of horizontal grid resolution in regional ocean models of Antarctic shelf seas is a subject of current research, with many studies finding that increased horizontal resolution is necessary to represent important physical processes, particularly mesoscale eddies and ice shelf basal melt rates (e.g., *St-Laurent et al.* [2013]; *Årthun et al.* [2013]). For these simulations, two horizontal grid resolutions are used: 5 and 1.5 km. The intent is that the coarser grid resolution is eddy-permitting, i.e., mesoscale eddy effects are simulated but the eddies are not fully resolved, are not necessarily the correct size, and would tend to dissipate rather than remain coherent and propagate, and that the finer resolution is eddy-resolving. It turns out that this assumption is mostly true for the Ross Sea, but due to the relatively weak stratification compared to other Antarctic shelf seas, resolving mesoscale eddies is a complicated topic. Chapter 4 is devoted to an analysis of mesoscale eddy dynamics in the Ross Sea and their relative representation at different horizontal grid resolutions in the model.

Ice Shelf

Part of the model domain includes the Ross Ice Shelf cavity. The Ross Ice Shelf front moves at about 1 km yr^{-1} , with a mean basal melt rate of about $10 \pm 10 \text{ cm yr}^{-1}$ [*Rignot et al.*, 2013]. Compared to ocean circulation over timescales of days to several years, the ice shelf can be considered static. In the model, the ice shelf is represented by a spatially varying ice shelf draft (the portion of ice that is below the sea surface). The direct effects of the ice shelf on the ocean water are parameterized in the following ways. Mechanically, the floating ice shelf applies the same pressure as would the same amount of water, and is parameterized based on the depth of the ice shelf and an estimate of the density of water equivalent to that amount of ice, as described in *Dinniman et al.* [2007]. Thermodynamically, the ice shelf basal melt rate is a function of ice shelf temperature, ocean temperature, salinity,

frictional velocity, and freezing temperature for that depth and salinity, and is parameterized based on equations from *Holland and Jenkins* [1999] with transfer coefficients for frictional velocity from *Schmidt et al.* [2004]. Additions of melt water to the top ocean layer is not a volume flux, as the ice shelf does not change position, but instead is a negative salt flux, proportional to the volume of freshwater that would be added from ice melt. A surface heat flux is calculated to account for heat transfer as ice melts. This parameterization is also described in detail in *Dinniman et al.* [2007].

Sea Ice Model

Another feature of ROMS that is useful for this specific application is the built-in coupled sea ice model [*Budgell*, 2005] that simulates the sea ice that covers the Ross Sea for most of the year and modulates the exchange between the ocean and the atmosphere. In this model, the sea ice is partitioned into four layers: two ice layers, a snow layer that insulates but holds no heat, and a molecular sub-layer under the ice that is in direct contact with the ocean. This configuration allows for realistic estimates of melting, refreezing, and brine rejection. The sea ice model also includes a parameterization for surface melt ponds and tracks sea ice thickness and age.

Initial Conditions

The initial conditions for the simulations are from a six year spin up, described in *Dinniman et al.* [2011]. Model conditions are initialized with climatology values of temperature and salinity from World Ocean Atlas 2001. The spin up simulation is forced with a two year repeating cycle of daily winds from the Antarctic Mesoscale Prediction System (AMPS), monthly AMPS climatologies of humidity, sea level pressure, air temperature, and precipitation, with cloud cover from the International Satellite Cloud Climatology Product (ISCCP). The spin up allows subsequent simulations to start from a stable model configuration with general flow patterns and temperature and salinity variations already established. As the spin up is driven by climatology values, it is a reasonable starting point for hindcast simulations covering various time periods. In this case, simulations are run for 1.5 years, allowing the model six months to adjust to the specific year forcing, with analysis constrained to the last year of simulation.

Boundary Conditions

One of the obvious benefits of using a regional ocean model is that it is regional: it is designed to focus on smaller areas in greater detail than a global ocean or basin scale model. However, this introduces added complications at open ocean boundaries. Information is needed along all ocean boundaries at all depths and at all times to correctly represent flow speed and the characteristics of water passing through the boundaries. Boundary conditions need to be set to specify water properties, including temperature, salinity, and velocity (and sea ice, in this case), and also to handle outgoing flows.

Here, temperature and salinity at the boundaries are set by climatology values from World Ocean Atlas 2001 and are controlled by a radiative nudging open boundary condition. Any outgoing flows ignore the boundary conditions, and the properties of the water passing through the open boundary are what is set internally by model processes. Incoming flows propagate the values set at the boundaries into the model and do so incrementally. Over a buffer zone of ten grid points, the temperature and salinity is adjusted to the incoming value at the boundaries, known as nudging. This creates a smooth adjustment between the boundary conditions and the interior model values, eliminating any sharp changes and un-physical flows caused by discontinuous density gradients.

Velocity boundary conditions are applied barotropically, as one velocity to the entire water column, and are obtained from the Ocean Circulation and Climate Advanced Model (OCCAM). The boundary condition here is also radiative nudging, where incoming flows are nudged to boundary values over ten grid points and outgoing flows are allowed to radiate away at the speed of local gravity waves. In the case of tidal forcing of velocity at the boundaries, the boundary condition follows *Flather* [1976] and radiates away only the portion of the flow that deviates from what is set at the boundaries.

Sea ice concentration (percent coverage) at the boundaries is derived from Special Sensor Microwave Imager (SSM/I) satellite data and interpolated to the model grid. On inflow, the sea ice values are clamped at the boundaries and not allowed to change. On outflow, the boundary is set to a gradient condition, meaning the gradient across the boundary is set to zero, allowing the outflow to be determined by the model. Sea ice velocities are set to a gradient condition on both inflow and outflow.

For this relatively small model domain, tidal forcing is applied at the open boundaries, rather than as a body force over the entire domain. Forcing for tidal constituents O1, K1, M2, and S2 is added as both sea surface height and velocity. The amplitude and phase of the tidal constituents come from the Circum-Antarctic Tidal Simulation (CATS2008) tidal

Simulation	Tidal Forcing	Horizontal Resolution
5	No	5 km
5T	Yes	5 km
1	No	1.5 km
1T	Yes	1.5 km
S5*	No	5 km

Table 3. Details of simulations used. *Simulation **S5** is a special case of **5** with repeat yearly forcing for 20 years.

model (an update of the model described by *Padman et al.* [2002]) and are nodally corrected, meaning that not only are the phases and amplitudes of the constituents correct, but the timing is adjusted to be accurate to the specific time of simulation.

Forcing

Similar to the side boundaries, the state of the atmosphere above the ocean or sea ice surface needs to be specified. There are several ways to do this including coupling an atmospheric model, setting the state of the atmosphere at the ocean surface, or imposing the flux of heat and freshwater into the top ocean layer. In this case, the best option is to set the state of the atmosphere at the ocean surface and calculate the fluxes across the ocean or sea ice surface boundary within the model. This avoids the unnecessary computational expense of a coupled atmosphere and the lack of detail from prescribing atmospheric fluxes. The atmospheric forcing is from ERA-Interim reanalysis data [*Dee et al.*, 2011] and includes six hourly winds and atmospheric temperatures, and monthly climatologies of humidity, precipitation, and cloud cover.

2.3.3 SIMULATION DESIGN

Hindcast simulations cover the time from September 15, 2010 to February 27, 2012. The year and a half simulation gives a six month adjustment from the initial spin-up conditions to the atmospheric and boundary forcing for this specific time period and one year of simulation for analysis. The last two months of simulation overlap the time of the PRISM-RS cruise (Section 2.2.1), allowing for a direct comparison with observations from that project.

The specific objective of this thesis is to trace pathways of dissolved iron from their sources to the surface ocean, and examine the effects of tides and mesoscale eddies on those pathways. To this end, a series of four simulations is designed, two simulations at each

horizontal grid resolution (5 and 1.5 km), one with tidal forcing included, and one without (Table 3). The simulations are referred to in the text by a bold number - **5**, for 5 km, and **1**, for 1.5 km horizontal resolution - and with a “T” designation, to indicate that tidal forcing is included.

One additional simulation is designed to test model stability and quantify variability of model variables over time as a measure of significance, which are both covered later in this chapter. This simulation, **S5** (where the “S” is for either special, stability, or significance), is a special case of simulation **5**, with repeat forcing from the year September 15, 2010 to September 15, 2011, applied for twenty years.

2.4 MODEL DRIFT

One of the key questions that arose during the configuration of the regional ocean model was, how stable is the final model configuration? For a regional ocean model with no conservation of tracers (temperature and salinity), no volume conservation when tidal forcing is added, and external forcing through the open boundaries that is not necessarily a net-zero change, examining computational stability explicitly does not make sense. Generally, the advection schemes used in ROMS are stable and a time step was chosen to ensure an appropriate Courant number (i.e., given the fastest velocities in a simulation, the time step must be small enough that a water particle cannot travel a distance of more than one grid point in one time step). This necessitates a more frequent time step with higher resolution and with the faster flows from tidal forcing.

Apart from these considerations, it is useful to examine the response of the model over long time scales, to determine if trends observed are realistic, or are a product of unrealistic model adjustment of initial conditions to applied forcing. Simply put, if the model is run for many years, do the results stabilize and become consistent, or is there a measure, perhaps unphysical, of model drift? In this situation, there are three possible responses of the model to repeat forcing over many years. Simulation output can show exponential changes over time, suggesting that there is a mismatch between the model configuration, the initial conditions, and the applied forcing. If there is a linear change over time in the simulation output, then the forcing applied to the model is non-zero over the course of a year and is driving the output to a new state. This indicates that either the initial conditions may not be fully appropriate for the applied forcing, or that the forcing from that year is different enough from climatology values to induce a shift in the model state. The final possibility is a steady or repeating pattern, indicating that while the forcing causes perturbations in the simulation

Parameter	Ice Area	95% CI	Ice Volume	95% CI
A	-2.427e5	[-2.461e5, -2.393e5]	-64.87	[-69.37, -60.36]
B	5.022e5	[4.988e5, 5.056e5]	435.5	[431, 440]
C	2.194e5	[2.160e5, 2.228e5]	108.7	[104.2, 113.2]
D	-2.135e5	[-2.169e5, -2.101e5]	-102.6	[-107.1, -98.1]
E	-1.060e5	[-1.094e5, -1.026e5]	0	N/A
F	6.547e4	[6.208e4, 6.886e4]	0	N/A
G	-550.8	[-966.7, -135.0]	-0.2072	[-0.7586, 0.3442]
H	1.037e6	[1.032e6, 1.042e6]	580.8	[574.4, 587.2]

Table 4. Fit parameters and confidence intervals of Equation 1 for sea ice area (km^2 , cols 2-3) and sea ice volume (km^3 , cols 4-5). Parameter G is given as $\text{km}^2 \text{ yr}^{-1}$, or $\text{km}^3 \text{ yr}^{-1}$, respectively.

output, the overall response is stable over time.

Simulation **S5** is designed to address this specific issue, using the 5 km grid, no tidal forcing, and repeat yearly forcing from September 15, 2010 to September 15, 2011. The adjustment of model variables from initial conditions to the applied forcing differ depending on the variable chosen: how strongly affected it is by forcing and the time it takes to respond. Four variables are chosen as diagnostics to cover a range of responses. Sea ice area and sea ice volume have relatively short adjustment times and are strongly affected by forcing. Ice shelf basal melt rates have a slower adjustment time, expected to be several years, as input from the boundaries and ocean surface must propagate under the ice shelf. Total on-shelf salt content is expected to be the most resistant to change, and at the same time, provides a comprehensive diagnostic of many processes that affect the salinity on the continental shelf, including sea ice formation, flow onto the shelf at the boundaries or at the shelf break, atmospheric forcing, and ice shelf melt.

For each of the diagnostic variables, time series analysis tools are used to examine the seasonal cycle and any long term trend. The sea ice area and volume timeseries are fit with an annual cycle, offset, and linear trend,

$$\begin{aligned} & A \sin(2\pi t) + B \cos(2\pi t) + C \sin(4\pi t) + D \cos(4\pi t) + \\ & E \sin(6\pi t) + F \cos(6\pi t) + Gt + H \end{aligned} \tag{1}$$

where t is time in years (sea ice volume timeseries and fit is shown in Figure 5 as an example). The fit parameters for sea ice volume indicate that there is no long term trend, with G not significantly different from zero (Table 4). Sea ice area shows a significant long term trend,

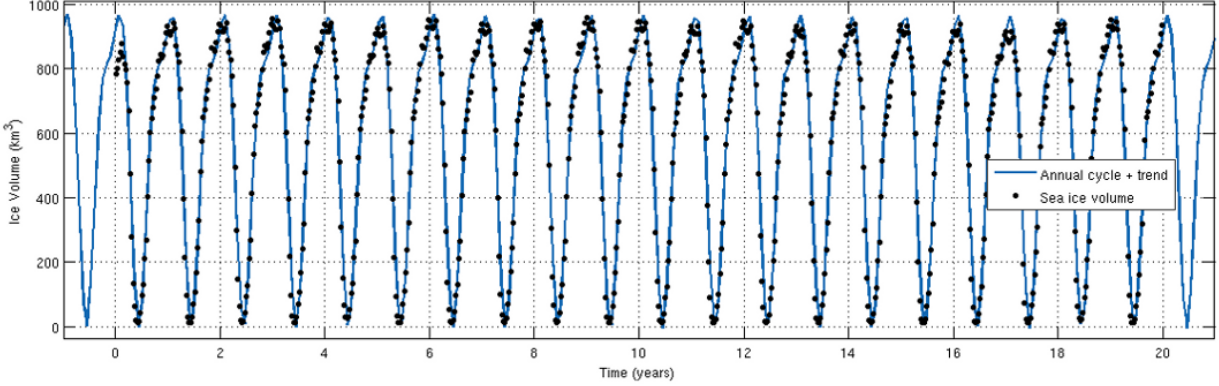


Figure 5. Sea ice volume timeseries (black dots) from simulation **S5** to test model drift. Blue line is a fit of an annual cycle, offset, and linear trend.

with $G = -550.8 \text{ km}^2 \text{ yr}^{-1}$, but the magnitude of this trend is quite small, less than 1% of the total signal over 20 years. This indicates the forcing induces more sea ice coverage each year than the initial conditions allow for, but the trend is small and can be considered negligible for simulations of 1-2 years.

The other two diagnostic variables, ice shelf basal melt and on-shelf salt content, are too complex to be easily fit by a simple annual cycle. Instead, STL (Seasonal Trend with Loess [*Cleveland et al., 1990*]) is used to partition the signal into a seasonal cycle, a nonlinear trend, and residuals (as shown in Figures 6 and 7 for basal melt and salt content, respectively). Fitting a line to the nonlinear trends obtained from STL gives negligible slopes five orders of magnitude smaller than the original signal for basal melt rate, and eight orders of magnitude smaller for salt content. The trend for basal melt rate comes to an asymptote after an initial adjustment, and for the last 7 years of simulation there is no significant linear trend, indicating that the applied forcing increases basal melt rates from initial conditions then stabilizes. The salt content trend shows a long term oscillation of about 12-14 years. A much longer simulation would be needed to resolve this long term oscillation, but unnecessary in this case, as the amplitude of oscillation is small compared to the total signal (0.1%).

In summary, the four diagnostic variables show either negligible or zero trends over the course of 20 years of simulation. As expected, sea ice area and volume adjust quickly to model forcing, while ice shelf basal melt takes longer. On-shelf salt content also shows a slow adjustment, which manifests as a low frequency oscillation. This analysis confirms the appropriateness of the model configuration, initial conditions, and forcing, and indicates there will be no significant effects from model drift over timescales of 1-2 years.

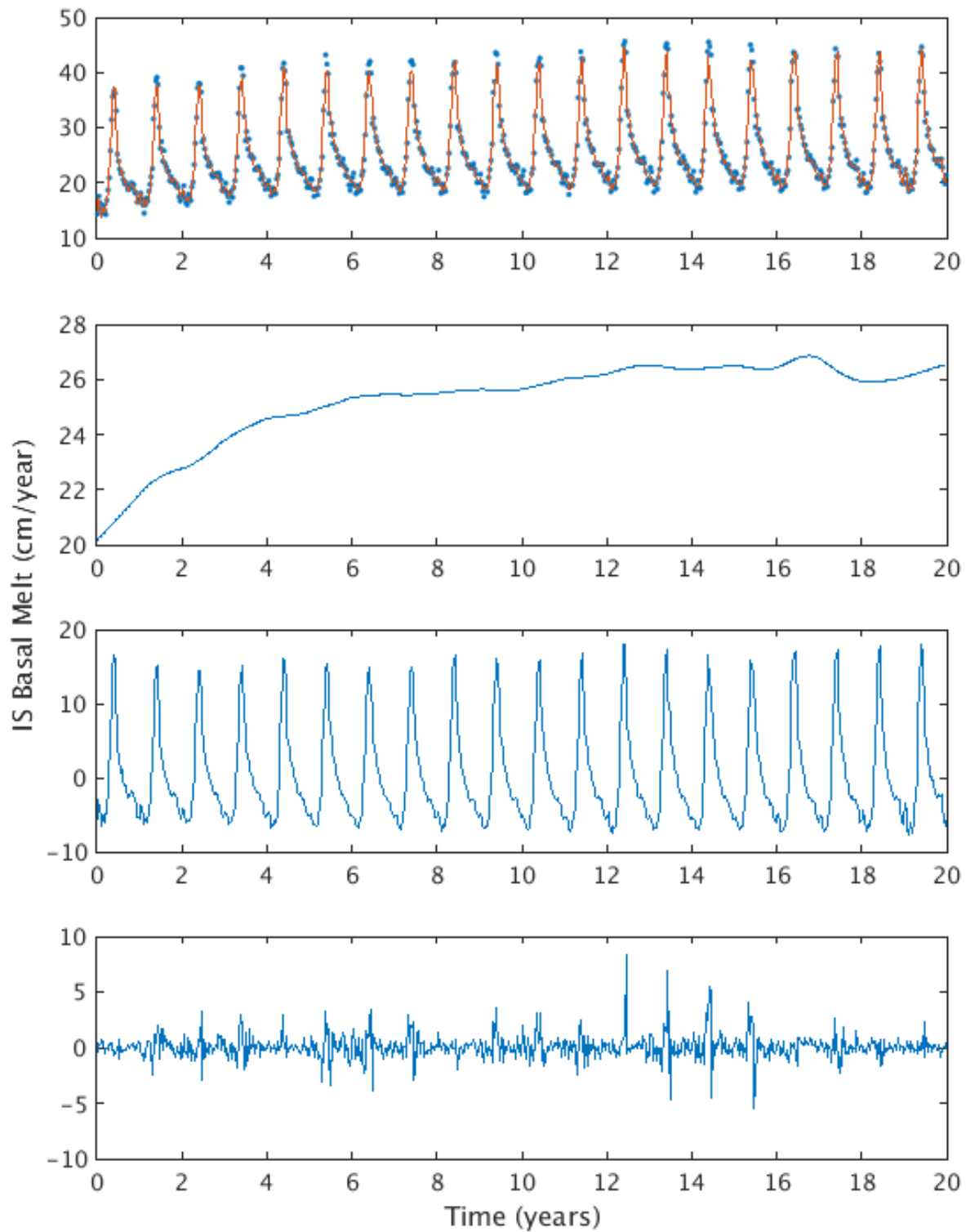


Figure 6. STL analysis of Ice Shelf basal melt rates over the 20 year simulation. From top to bottom: original signal (dots) with STL fit (line); nonlinear trend; annual cycle; sub-annual variability (residuals)

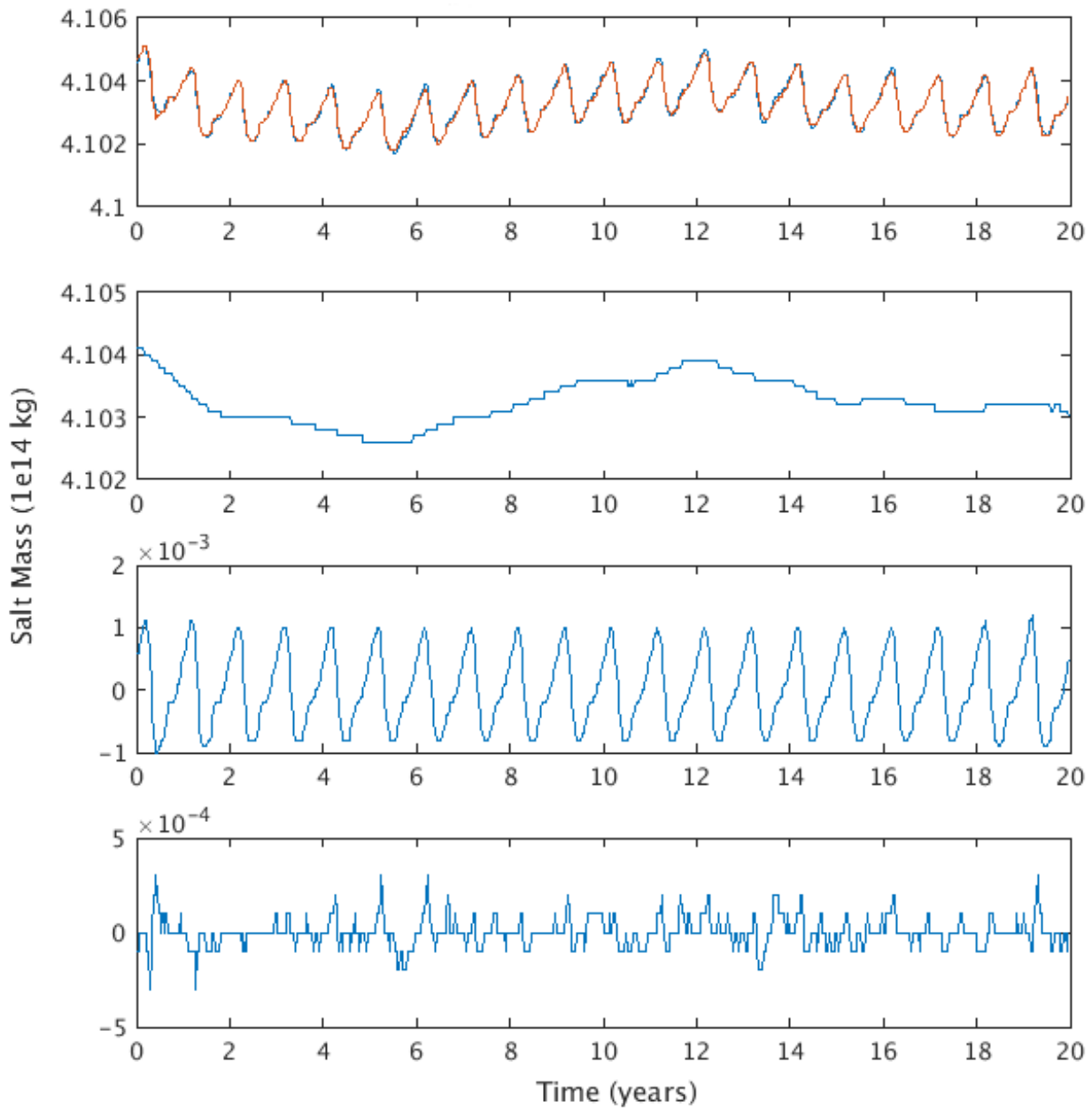


Figure 7. STL analysis of salt content(kg) on the continental shelf from the 20 year simulation. From top to bottom: original signal (dots) with STL fit (line); nonlinear trend; annual cycle; sub-annual variability (residuals)

2.5 MODEL ANALYSIS TOOLS

Two specific model tools are used to improve analysis of model behavior and compare simulations. The first is the passive tracers that are included in the ROMS code. These tracers act as Lagrangian dyes that are advected and diffused throughout the model domain, illuminating pathways of flow and tracing water masses through transformations. For this research, a passive tracer dye is specified for each potential source of dissolved iron and provides information about iron concentration without coupling a biological model to the regional ocean model. The second tool is a newly developed method that sets a significance criterion for comparing similar simulations by quantifying the sub-annual variability of a model variable and determining if the difference between simulations is greater than that variability. This tools provides a way of directly comparing two simulations without using ensemble statistics or (often non-existent) observations.

2.5.1 PASSIVE TRACER DYES

Each simulation includes four passive tracer dyes representing different water masses and/or physical processes in the model and correspond with a potential source of dFe. Here I describe the physical meaning and motivation behind each tracer dye; the translation to dFe concentration is covered in Chapter 6.

The first dye, dye_{CDW} is a proxy for Circumpolar Deep Water (CDW). It is initialized at 100 arbitrary dye units in off-shelf waters, where off-shelf is defined as seaward from the 800 meter isobath, in waters that match the characteristics of CDW (warmer than 0 °C [Dinniman *et al.*, 2011]). The dye tracks intrusions of CDW on the continental shelf throughout the simulation and its transformation to other water mass types. With the exception of fresh water inputs, i.e., melt water from the ice shelf and precipitation, all on-shelf water is thought to have originated as CDW. Thus, a long enough simulation will fill up the continental shelf with dye_{CDW} , as is examined in Chapter 3.

The next two dyes, dye_{SIM} and dye_{GM} represent melt water, from sea ice and glaciers, respectively. Both are initially zero in the whole model domain and are introduced into the top model layer as a factor of positive melt rate. Note that a negative melt rate, i.e. freezing, does not produce a negative dye flux. The glacial melt dye, dye_{GM} includes melt from both the Ross Ice Shelf and other neighboring glaciers in the model domain. These two dyes, as well as dye_{CDW} , have been included in past versions of the Ross Sea model, e.g. Dinniman *et al.* [2011].

The final dye, dye_{bdFe} , is designed specifically for this thesis to represent benthic sources of dFe. It is initialized at the start of the last year of simulation at select locations on the continental shelf, following observations described in *Marsay et al.* [2014]. The dye is held constant at 100 arbitrary dye units in the bottom model layer in-shore of the 700 meter isobath, at locations that are deeper than 400 meters, which excludes shallow major banks on the continental shelf. Although the formulation of this dye is specific to representing benthic sources of dFe, physically it traces pathways of dense on-shelf waters as they cascade off-shelf, shows the mixing and advection of deep waters over the banks, and highlights areas of strong modeled vertical mixing.

2.5.2 DETERMINING SIGNIFICANCE BETWEEN SIMULATIONS

One of the major issues with the design of these studies is how to determine significance when comparing two simulations, i.e., at what point does the difference in simulation output become meaningful? There are several limitations to using high resolution regional ocean models that make commonly used methods of estimating significance unworkable. Global climate models determine a level of significance between models by using ensemble statistics, which requires a sufficiently large number of simulations, more than is reasonable given the computation cost and available resources for this model design. Single model simulations determine significance by direct comparison with observations, which are very limited in this region. Thus, an alternate measure of significance is needed to compare simulations, referred to here as a Simulation Significance Criterion (SSC), designed specifically for similar simulations that use the same base model configuration.

Computation of the SSC uses the 20 year simulation with repeat yearly forcing (**S5**). The general premise of the SSC is that, using long timeseries from **S5**, the sub-annual variability of any model variable can be estimated and represented as a portion of the total signal. Results for a given variable from two different simulations are considered the same if they fall within the range of the sub-annual variability. However, if they are different by more than that, then the difference between simulations for that variable can be considered significant.

To illustrate the specific computation, the SSC for ice shelf basal melt is calculated as an example. STL is used to decompose the twenty year basal melt rate timeseries from **S5** into a nonlinear trend, a seasonal cycle, and sub-annual variability (or residuals). The root-mean-square (RMS) of the sub-annual variability is divided by the RMS of the rest of

the signal (seasonal cycle plus nonlinear trend) to obtain a fraction (or percent) variability:

$$SSC = \frac{RMS(\text{subannual})}{RMS(\text{trend} + \text{fit})} \times 100\%. \quad (2)$$

The timeseries of ice shelf basal melt rate and its decomposition by STL is shown in Figure 6. From this decomposition, the RMS of the sub-annual variability is 1.15 and the RMS of the remainder of the signal is 26.15, giving an SSC of 4.40%. Now, if the basal melt rates from two other simulations are compared, say **5** and **1**, and the difference is more than 4.40%, then those simulations have significantly different basal melt rates. For this example, the ice shelf basal melt rate over the last year of simulation is 21.42 cm yr^{-1} for **5** and 22.47 cm yr^{-1} for **1**. Applying the SSC gives melt rate bounds of [20.47, 22.36] for **5** and [21.48, 23.49] for **1**. This 5% increase in basal melt rate is considered not significant as the bounds given by the SSC overlap for the two simulations.

In general, the SSC can be applied to any variable expressed as a timeseries. For this thesis, it is specifically applied to average mixed layer depth, basal melt rate, amount of dye in the surface mixed layer, among other quantities.

2.6 CONCLUSION

The design of the Ross Sea model using the ROMS framework is appropriate for examining the effects of tides and mesoscale eddies over the course of one year. The general structure of the model includes the physical processes of interest, such as melt water from sea ice and glaciers, passive tracers for specific water masses, and forcing from the atmosphere and from the ocean along the open boundaries. Analysis of the 20 year simulation **S5** shows no significant model drift over timescales of interest (1-2 years) and provides a mechanism to directly compare simulations and determine significance between them. The rest of this thesis will compare the various simulations described here and examine results from them all, including **S5**, and draw conclusions about the significance of the results using the SSC developed for direct simulation comparison.

CHAPTER 3

MODEL VALIDATION

3.1 INTRODUCTION

Generally, observations of the Ross Sea are scarce, particularly in winter months, which provides motivation for using a regional ocean model. While this statement is mostly true, there are sufficient observations and compilations of climatologies available to validate the model prior to using it to investigate the pathways of dissolved iron and the effect of tides and mesoscale eddies.

Model validation is typically the second step of a two part process that confirms the model behaves in a reasonable and expected manner. The first part, verification, checks if the processes being modeled are implemented correctly. This step, for a community model such as ROMS, has already been done. The second part, validation, checks how accurately the model represents reality. As models are only approximations of reality, perfect accuracy is not expected. The simulations should reasonably match observations and, ideally, mismatches can be attributed to specific assumptions or limitations of the model design.

For this thesis, I split the model validation into two parts. First, I examine if the model reasonably represents the specific hindcast period covering the PRISM-RS cruise, i.e., single year summer conditions at select locations. This can be determined using observations from the PRISM-RS cruise, specifically CTD casts with vertical profiles of temperature and salinity. Then, I investigate if the model reasonably represents the Ross Sea conditions over the continental shelf over all seasons. To address this part of the model validation, climatological observations of the Ross Sea over many years and seasons are used, in the form of a water mass volumetric census.

3.2 METHODS

Validation I: PRISM-RS observations

The PRISM-RS cruise observations, described in section 2.2.1, provide information about the state of the Ross Sea at specific locations and times in January and February 2012. For

this portion of model validation, CTD casts of temperature and salinity are directly compared with simulation output. It is unlikely that there will be a direct match between simulation and observations. However, if the model is realistic, the temperature and salinity pairs from the CTD casts should exist in the simulation, perhaps offset in space and/or time or a smoothed representation.

For the point comparison, a series of stations were defined in simulations that matched the exact location of the PRISM-RS CTD stations (i.e., not snapped to the model grid). High frequency (hourly instead of daily) output of model variables was recorded at these stations, creating detailed timeseries. This degree of accuracy in matching the time of the CTD casts is not a reflection of how accurate I expect the model to be, but is the best way to match the tidal cycle and amount of solar radiation to the observation conditions. Simulations **5** and **5T** were both used for this comparison. Temperature and salinity from the model and from observations are used to calculate the standard Conservative Temperature (Θ) and Absolute Salinity (S_A), as defined by the 2010 updated Equation of State (TEOS-10) [IOC *et al.*, 2010].

Validation II: Water Mass Volumetric Census

To validate the model beyond the point locations during the time of the PRISM-RS cruise, I use a climatological water mass volumetric census for all waters on the continental shelf from *Orsi and Wiederwohl* [2009]. Data from a series of research cruises to the Ross Sea from 1976 through 2004 were compiled to estimate the volume of each water mass on the continental shelf. These data are biased towards austral summer, the time of most cruises, and do not contain any estimates of temporal variability. Despite this, they are an excellent baseline, derived from direct observations, and provide an important diagnostic for the Ross Sea model. Further description of the water mass census climatology can be found in *Orsi and Wiederwohl* [2009], hereafter OW09.

A detailed description of Ross Sea water masses and their formation and modification is in Section 1.1.2 and the associated Table 1. To briefly recap: Water masses are separated first by neutral density [*Jackett and McDougall*, 1997] categories, with the lightest broadly defined as Antarctic Surface Water (AASW). Mid-range density waters include Circumpolar Deep Water (CDW), which is called Modified CDW (MCDW), if found on the continental shelf (in-shore of 700 meters). The densest water masses are subdivided into three categories, based on temperature. The warmest is Modified Shelf Water (MSW), and the coldest Ice Shelf Water (ISW). The mid-range, known simply as Shelf Water, is further separated into

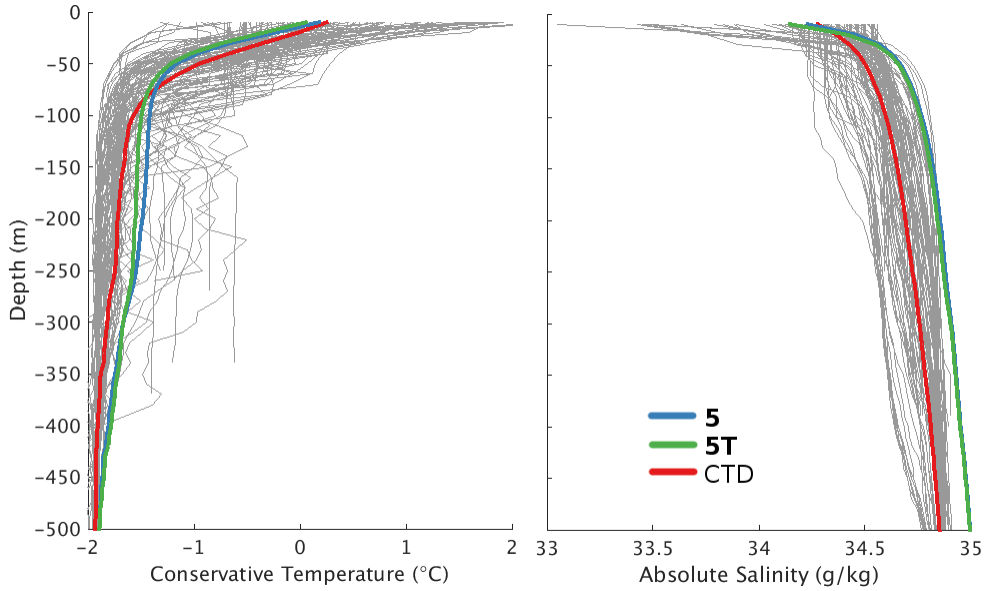


Figure 8. Conservative Temperature and Absolute Salinity depth profiles from PRISM-RS CTD casts (gray lines). Thick solid lines are average profiles for CTD casts and simulations **5** and **5T**.

two distinct types based on salinity: Low Salinity Shelf Water (LSSW) and High Salinity Shelf Water (HSSW).

A water mass census is calculated for simulations **5**, **5T**, and **S5** following the guidelines in Table 1. Every model grid cell in-shore of the 700 meter isobath is tagged with a water mass type based on neutral density, temperature, and salinity. Note that the temperature and salinity thresholds here are given as potential temperature and practical salinity (psu), as OW09 predates the introduction of Conservative Temperature and Absolute Salinity. Then, the volume of the cells tagged with each water mass type are summed to obtain a timeseries of water mass volumes on-shelf for these three simulations. These timeseries are compared to the climatological values presented in OW09. Results from simulation **S5** are used to calculate the Simulation Significance Criterion (SSC), which determines if simulations are significantly different from one another (see Section 2.5.2).

3.3 RESULTS AND DISCUSSION

3.3.1 VALIDATION I: PRISM-RS OBSERVATIONS

Conservative Temperature and Absolute Salinity depth profiles from each PRISM-RS

CTD station on the continental shelf and from the corresponding simulated station are compared by calculating an average profile for each (Figure 8, with individual PRISM-RS profiles shown in gray to illustrate the range of conditions sampled). The results from simulations **5** and **5T** are not significantly different from each other. In general, depth profiles show a similar pattern between simulations and observations. Comparing Conservative Temperature, the simulations have a slightly shallower surface mixed layer, leading to a sharper gradient between the mixed layer and mid-depths, with slightly warmer waters below the base of the thermocline. For Absolute Salinity, values at the surface ocean are similar, but there is a consistent offset at depth, with simulation values saltier than observations.

To further examine the differences in depth profiles at CTD stations between the simulations and observations, each PRISM-RS depth profile is subtracted from the corresponding model station profile (Figure 9) for simulation **5**. Conservative Temperature in the simulation is cooler than observations near the surface, slightly warmer below 100 meters, and shows no difference below about 500 meters. Absolute Salinity values are similar at the surface, after which the simulation results show a consistent offset from observations. The net offset at depth (below 100 meters) is about 0.14 g kg^{-1} , and is consistent across all stations. The depth-averaged salinity for each station, with only one exception, is greater in the model than in the PRISM-RS observations.

The salinity offset between simulations and observations first suggested a systematic error in either the salinity measurements or in the model calculation. Once this was ruled out, simulation values used for the comparison are expanded to include all values on the continental shelf in January and February 2012 (Figure 10). Overlaying the observations on the simulation output in Temperature-Salinity space highlights a few combinations of temperature and salinity that were observed but are not present in the simulation. Specifically, the CDW end member ($S_A = 35 \text{ g kg}^{-1}$; $\Theta = 1.5^\circ\text{C}$) is warmer in observations than in the simulation, and there are some warmer AASW observations as well. For the dense, cold waters below the surface freezing point of seawater, the observations cover a region of temperature-salinity space that is either colder than the simulation values, or less saline. Waters with these characteristics are only found underneath the ice shelf in simulation **5**, not on the continental shelf. This suggests that the deep shelf waters are consistently more saline in the simulation and not an artifact of the point by point comparison with observations.

There are several possible reasons why salinity is higher in the simulation: too much sea ice is produced, initial conditions are too saline and do not have time to adjust to forcing, or boundary conditions are too saline and maintain the offset over time. A quick estimation

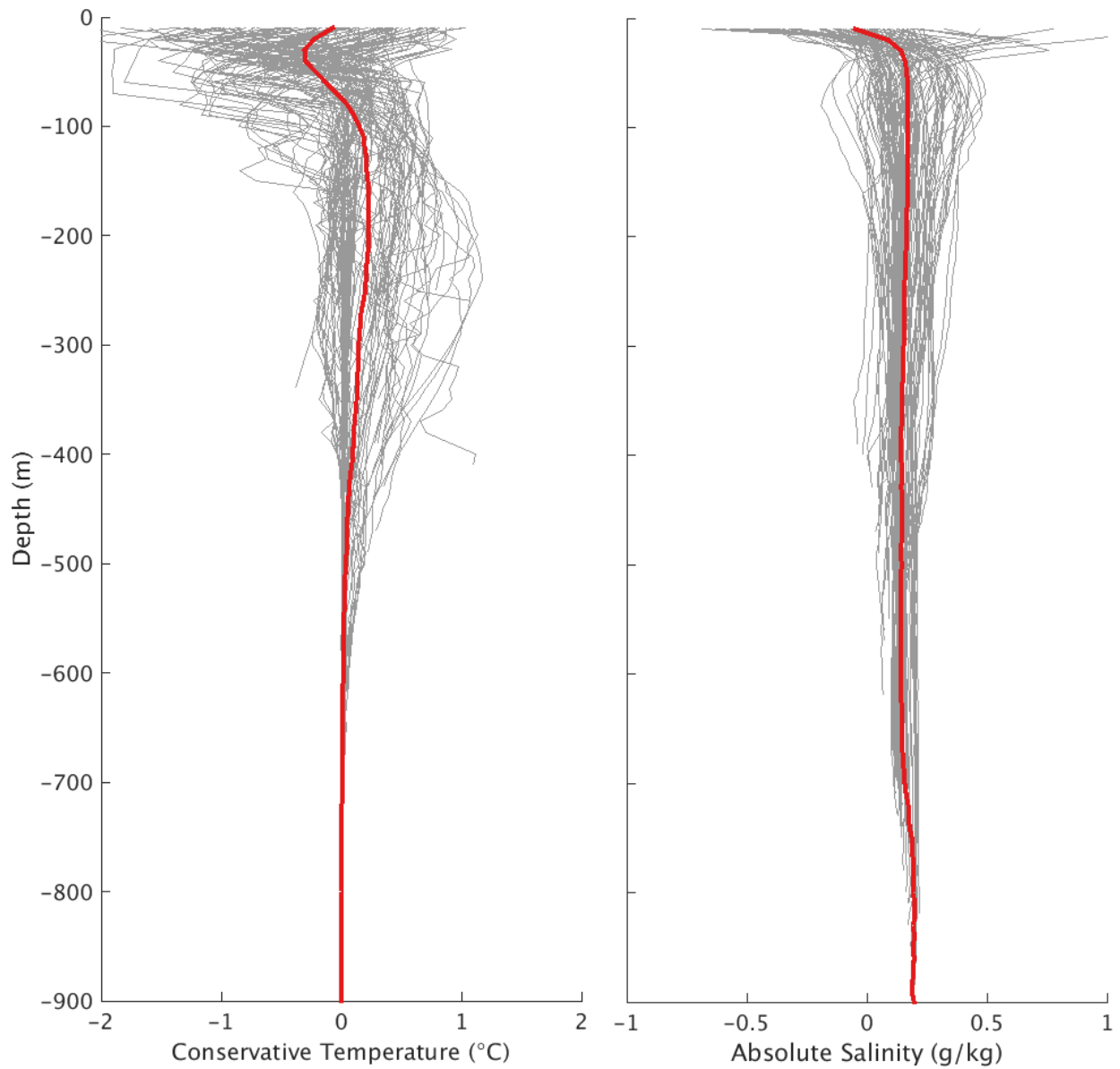


Figure 9. Differences between depth profiles from CTD and simulation 5. Thick red line is the average difference. Positive values indicate simulation is warmer or saltier than observations.

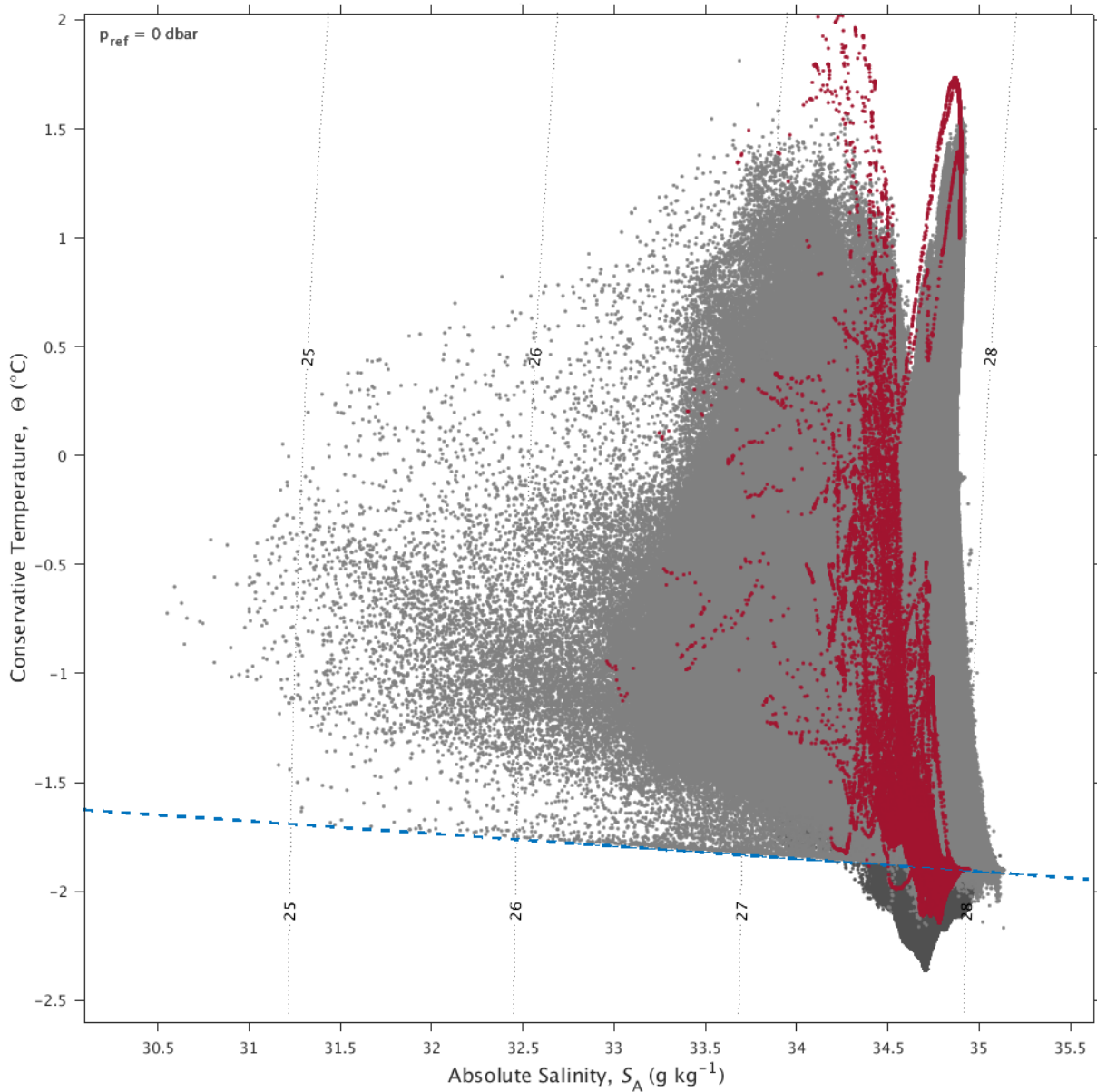


Figure 10. Temperature-Salinity diagram. Gray points are sub-sampled on-shelf values from simulation 5 for Jan-Feb 2012. Darker gray indicates values under the ice shelf. Red points are PRISM-RS CTD measurements. Dashed contours are constant potential density lines, blue dashed line is freezing temperature at surface conditions.

shows that every grid point on the continental shelf would need to make approximately 2 meters less sea ice to freshen the deep waters sufficiently to match observations. This is clearly not the issue, as a reduction of that magnitude in sea ice production would have profound effects on simulation output beyond deep on-shelf salinity values.

If the initial conditions contain a salinity offset at depth, the simulation would adjust over time and correct that offset. Results from the 20 year repeat simulation, **S5**, show that this is not the case, as the offset remains constant. The final, and most likely, scenario is that the boundary conditions are too saline: the model is forced and maintains a steady salinity offset at depth over time. The boundary conditions are obtained from climatology values from over 10 years before the PRISM-RS observations. In that time, the Ross Sea has been freshening, caused in part by input from the Amundsen Sea to the east [Jacobs *et al.*, 2002]. A recent study estimates that the Ross Sea is freshening by 0.03-0.08 per decade [Jacobs and Giulivi, 2010]. As the data used to create the boundary condition climatology may range in age from one to several decades old, the constant salinity offset of 0.14 g kg^{-1} can be attributed to the Ross Sea freshening in recent years.

3.3.2 VALIDATION II: WATER MASS VOLUMETRIC CENSUS

Timeseries of water mass volumes on the continental shelf from simulations **5** and **5T** are compared with the climatological estimate (a single number for each water mass) from OW09 (Figure 11). For every water mass, except ISW, there exists a point in time where the OW09 estimate and the simulation value is the same. This match up between simulation and data does not occur at the same time for each water mass, nor does it occur only during the summer months, when most of the climatological observations were taken. This indicates, that to a first order approximation, the model matches observations. Discrepancies can be partially attributed to the non-uniformity of the data used to construct the climatology, both in space and in time. The volume of ISW does not match the climatological data; although the amount of ISW appears to increase with time, results from simulation **S5** (not shown) show the values remain similar to those at the end of simulation **5**.

Comparing simulation **5** to the OW09 climatology shows that the simulation generally has less AASW, MCDW, HSSW, and ISW than in observations, but more LSSW and MSW. The simulation appears to still be adjusting to initial and boundary conditions, as the amount of MSW generally decreases over the 1.5 year simulation, while the amount of AASW increases. The overestimate of LSSW and underestimate of HSSW indicates that the deep on-shelf waters in the simulation are fresher than the climatological values, possibly an artifact of

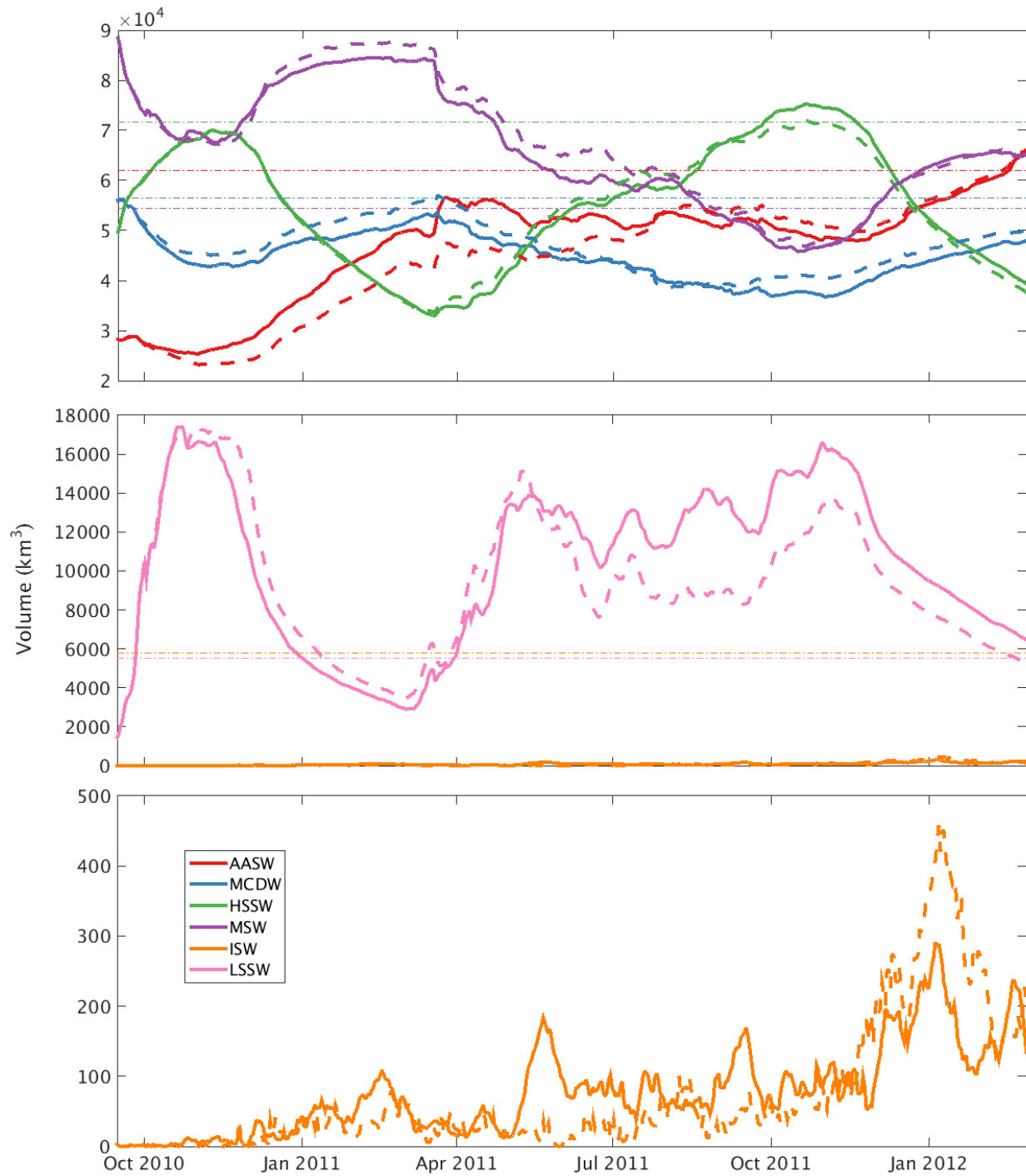


Figure 11. Volume of water masses (km^3). Solid line is from simulation 5; dashed from 5T; thin dash dot from *Orsi and Wiederwohl* [2009]. Note the scales in each panel change to better illustrate the variability of each.

the freshening of the Ross Sea over time.

Ice Shelf basal melt rates

The lack of ISW on the continental shelf suggests that the model either does not produce enough ISW or that the ISW is not transported correctly to the ice shelf front. A proxy for the production of ISW is the annual average basal melt rate of the Ross Ice Shelf. Recent estimates put the basal melt rate of the Ross Ice Shelf at around $10 \pm 10 \text{ cm yr}^{-1}$ [Rignot *et al.*, 2013]. The model overestimates this melt rate, with 21.4 cm yr^{-1} for simulation **5** and a significant 13.8% increase to 24.4 cm yr^{-1} for simulation **5T** (SSC = 4.4%). This indicates that the model is producing a excess amount of ISW through basal melting of the ice shelf, and the lack of ISW on the continental shelf is not due to low melt rates.

The low amount of ISW on the continental shelf could be attributed to the spatial pattern of ice shelf basal melt. Melt water from the ice shelf front is upwelled and incorporated into AASW as it exits the cavity. If the melt water originated further back in the cavity, it gains density through refreezing and entrainment of ambient waters, and exits the cavity as a plume at mid-depth. Previous work [Dinniman *et al.*, 2011] using an earlier version of this model found that the ISW plume at depth is in the same location and has a similar temperature to climatological values from OW09, but is smaller in cross-sectional area, indicating less ISW is exiting the cavity at depth. As melt rates are higher in the model than in observations, the production of ISW is not suppressed. ISW is likely entering the continental shelf region already transformed into another water mass, as AASW near the surface, or as HSSW or LSSW at depth.

3.3.3 CIRCUMPOLAR DEEP WATER TRANSFORMATION

All water masses on the Ross Sea continental shelf, with the exception of ISW, were once off-shelf CDW. Processes on the shelf provide the mechanisms by which CDW transforms into the other water masses, including cooling from interaction with the atmosphere and from sea ice and glacial ice melting, freshening from ice melt, and increasing salinity from brine rejection. The spatial and temporal variance of these processes, as well as mixing, determines the relative amounts and locations of water masses. For example, higher sea ice formation and brine rejection on the western side of the shelf leads to HSSW, while lower salinities in the east are associated with more LSSW.

The transformation of CDW to other water mass types over time is tracked in the simulations by calculation the amount of the passive tracer dye dye_{CDW} in each water mass

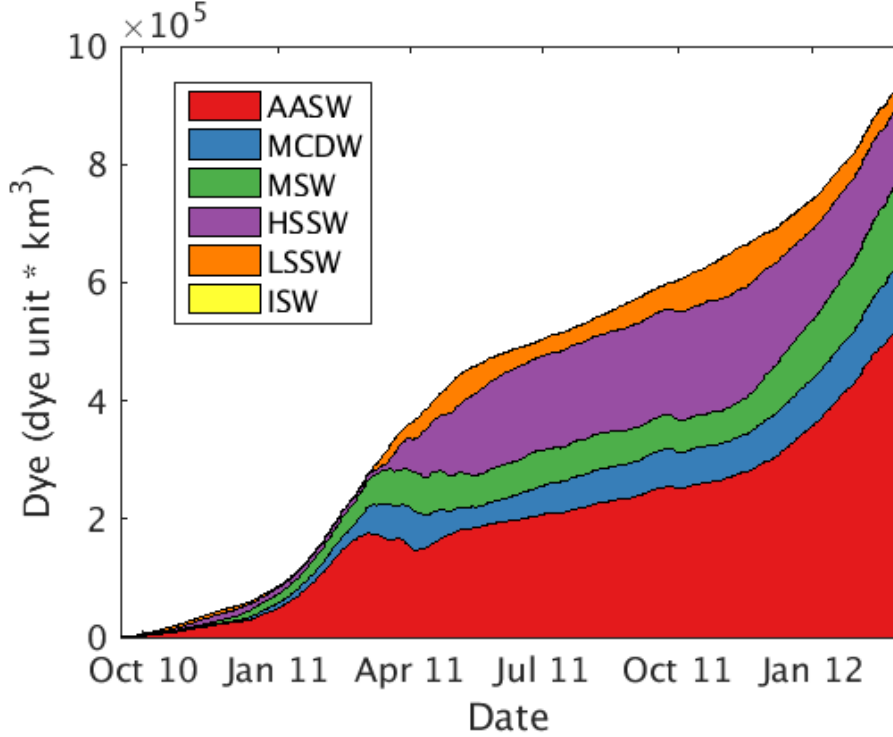


Figure 12. Amount of dye_{CDW} on the continental shelf (inshore of 700 meter isobath) for simulation 5, its distribution across water masses. Dye is given as dye units times volume, where dye units are treated as an arbitrary concentration. Date is given as month, year.

on the continental shelf. This dye starts at zero on the continental shelf, and is initialized at 100 arbitrary dye units in all off-shelf waters deeper than 300 meters and warmer than 0° (see Section 2.5.1 for details). As the simulation progresses, the dye follows specific water parcels as they transform and dilutes through mixing in diffusion, acting as a concentration of water that started as CDW.

Results from simulation 5 show that the amount of dye_{CDW} starts at zero on the continental shelf and increases over time as more CDW intrudes (Figure 12). The rate of dye accumulation on the shelf is higher during the summer (January through March), and lower the rest of the year (April through December). This indicates a seasonality to CDW intrusions or to the export of other water masses containing dye_{CDW} . In the first six months of simulation (September - March), dye_{CDW} mostly appears in AASW, but also in MCDW and MSW. The transformation to these three water masses is primarily through mixing processes: as the CDW intrudes on the shelf, it loses heat to become MSW, and mixes with cold, fresh AASW to form both MCDW and more AASW. The start of sea ice formation at the end of

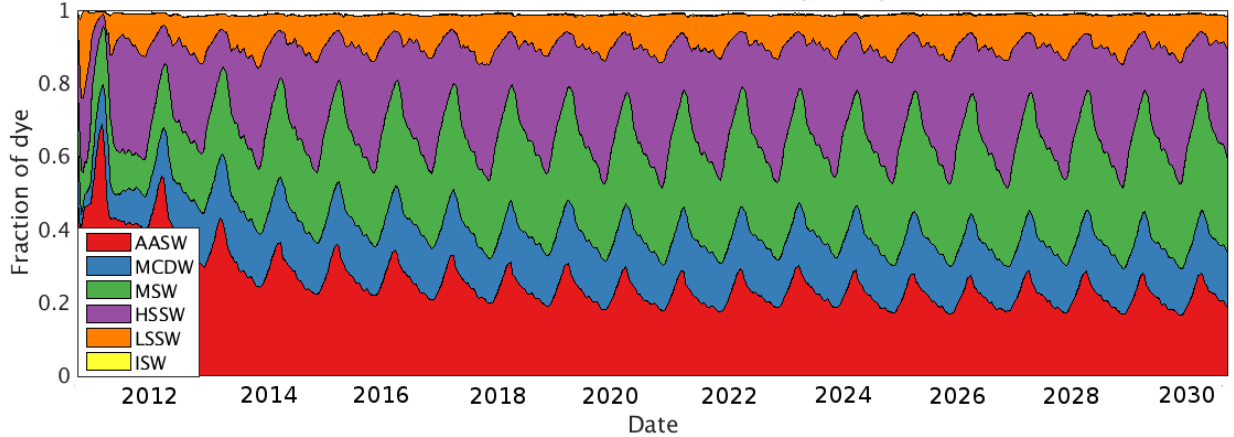


Figure 13. Fraction of dye_{CDW} on the continental shelf (inshore of 700 meters that is present in each water mass for simulation S5. Dates represent model years; forcing is repeated from the first year.

the first simulation summer is very noticeable, as dye_{CDW} makes a significant appearance in HSSW and LSSW, created through brine rejection mixed with CDW and some ISW. As the simulation progresses, the amount of dye_{CDW} in MCDW and MSW stays relatively constant, while that in AASW continues to increase. Results from simulation **5T** are not significantly different from **5**.

The continued evolution of dye_{CDW} on the continental shelf is seen in results from simulation **S5**, the 20 year simulation with repeat annual forcing. After six to eight years of simulation time, the total amount of dye_{CDW} on the shelf reaches a steady state, but the fraction of dye in each water mass varies seasonally, matching the seasonal variation of water mass volumes (Figure 13). In late summer and early autumn, the fraction of dye_{CDW} in HSSW and LSSW increases, as seen in simulation **5** due to the onset of sea ice formation. Once brine rejection ceases, mixing processes increase the fraction in modified water masses: AASW, MCDW, and MSW. Overall, the fraction of dye in each water mass is similar to the fraction of on-shelf volume for each, as calculated from the water mass volumetric census (i.e., Figure 11). This implies that the model is using CDW as its source water mass for all on-shelf waters (except ISW), and the physical processes and applied forcing in the model accurately transform CDW into the relative amounts of each.

3.4 CONCLUSION

Observations from the PRISM-RS cruise and from climatological data indicate that the

Ross Sea model design is a sufficient representation of the processes controlling temperature and salinity variations and water mass volumes. The validation process brought to light several issues with the model, including the too saline boundary conditions and the low amount of ISW present on the continental shelf. These issues indicate places where simulation results are less likely to accurately represent reality and should be kept in mind when analyzing model output. Generally, the validation provided justification that the simulation can be used to infer details about physical processes at times and locations that are unobserved.

Aside from model validation, the comparison of temperature and salinity vertical profiles with recent observations illustrates how recent climate change in the Ross Sea affects model design. Specifically, the freshening of Ross Sea waters, due in part to increased ice shelf melt in the neighboring Amundsen Sea, is substantial enough that there is an obvious difference between the boundary controlled deep simulation salinities and salinities from more recent observations on the shelf. The model boundary conditions are from a climatology from 2001, which is a compilation of observations from years prior to 2001, while the PRISM-RS data is from 2012, giving an offset of over a decade. This suggests that for conditions known to be affected by climate change, using climatological data to drive models is not the best approach. Given the amount of information needed to determine model boundary conditions, it is not practical to avoid using climatologies on the open boundaries. One potential solution is to adjust the boundary conditions to account for climate change; freshening them in this case.

The further validation of the model with the water mass volumetric census illustrates the seasonal variability of water mass volumes. In the OW09 dataset, the water mass volumes are climatologies, calculated from observations at different times of the year over several decades. There are not sufficient observations to estimate water mass volumes on the continental shelf over a smaller time period, much less at multiple times per year. A basic understanding of processes on the Ross Sea shelf, along with simulation results, indicates that the volumes of water masses vary seasonally and interannually. Future work to further explore this variability could include hindcast simulations to re-create a simulated version of the water mass climatology. Then, the simulation-derived climatology could be compared with seasonal and interannual variability to determine if the OW09 climatology is a representation of a yearly average or of summer conditions, and to characterize how much each water mass volume varies seasonally and interannually.

The water mass volumetric census also demonstrates that the model does not have enough ISW on the continental shelf. As basal melt rates from simulations exceed observational estimates, the trouble is that the ISW signal is partially mixed away before it exits the

cavity. There are two primary ways glacial melt water exits the ice shelf cavity. Melt near the ice shelf front is close to the surface and is mixed into AASW instead of contributing to the dense shelf waters. Melt from further back under the ice shelf is deeper and therefore colder than melt near the surface. This water makes its way to the ice shelf front, following the upward sloping ice shelf base. As it rises, it reaches a pressure at which it begins to freeze again. Frazil ice crystals form along the ice shelf bottom, which increases the salinity of the remaining melt water. This increase in density causes the ice shelf water to detach from the ice shelf bottom at several hundred meters down and flow seawards as a coherent plume. The model does not represent this plume, and thus the amount of ISW on the continental shelf, correctly. This could be due to the spatial distribution of ice shelf melt: too much near the ice shelf front and not enough deep in the cavity. It could also be due to the lack of a frazil ice parameterization in the model, causing the ISW plume to not separate from the ice shelf base and exit the cavity close to the sea surface instead of several hundred meters down. In a similar model of the Amery Ice Shelf in East Antarctica, a parameterization for frazil ice was used to improve refreezing of melt water and ISW plume export [Galton-Fenzi *et al.*, 2012]. This is a potential way to improve the Ross Sea model for future work.

CHAPTER 4

MESOSCALE EDDIES

4.1 INTRODUCTION

Mesoscale oceanic eddies, originating from instabilities, play a role in ocean mixing and energy transfer. Eddies act to stir the water column and enhance localized diffusion by creating filaments of water along their edges. Non-locally, eddies retain and transport water in their cores, sometimes over large distances (e.g., the Gulf Stream rings). In terms of vertical mixing, eddies induce localized upwelling and downwelling through eddy intensification or eddy-induced Ekman pumping. Interactions between eddies and the wind also lead to strong vertical transports [Niiler, 1969; Stern, 1965]. Generally, mesoscale eddies act to erode fronts and re-stratify the surface ocean [Boccaletti *et al.*, 2007], converting the available potential energy in horizontal density gradients to kinetic energy (KE). Global distributions of eddies analyzed with satellite data show that mesoscale eddies tend to have higher sea surface height (SSH) amplitudes near strong currents, such as western boundary currents [Chelton *et al.*, 2007].

Eddy effects in the ocean have a significant influence on ecosystems, from surface chlorophyll distributions to the patchiness of higher trophic levels [McGillicuddy Jr., 2016]. Mesoscale eddies operate at the same spatial scale as phytoplankton and zooplankton dynamics [Dickey, 1991], and localized enhancement of primary production at the mesoscale establishes the patchiness and distribution of higher trophic level species. Eddies play a role in nutrient transfer through eddy advection or diffusion processes, which can oppose or complement one another [Lee and Williams, 2000]. In most cases, mesoscale eddies enhance primary production and near surface chlorophyll as the associated vertical mixing brings more nutrients to the surface and the re-stratification increases exposure to solar radiation [Gaube *et al.*, 2014]. However, in upwelling systems, particularly in eastern boundary areas, eddies act to suppress primary production by transporting nutrients away from the coastal area to the open ocean [Gruber *et al.*, 2011].

In the Southern Ocean, eddies are a persistent feature of the Antarctic Circumpolar Current (ACC) [Rintoul *et al.*, 2001]. Eddies in the ACC transport wind-induced momentum

vertically until it is dissipated by bottom form drag [*Johnson and Bryden*, 1989]. This leads to a southward eddy-induced transport of heat that compensates for heat lost to the atmosphere south of the Polar Front [*Phillips and Rintoul*, 2000]. Eddies in the ACC also have an effect on surface chlorophyll. In the area near South Georgia, for example, cyclonic eddies are associated with an increase in surface chlorophyll at their centers while anticyclonic eddies have low amounts in the center but enhanced levels along the outer edge of the eddy [*Kahru et al.*, 2007].

South of the ACC and closer to the continent, eddies play a role in transporting warm off-shelf water onto the continental shelf. An idealized model of an Antarctic shelf sea with an ice shelf cavity illustrates how eddy effects are necessary in simulations to properly advect warm water on-shelf [*St-Laurent et al.*, 2013]. Specifically, eddies affect basal melting of the Fimbul Ice Shelf in the Weddell Sea by inducing an overturning of the Antarctic Slope Front and allowing relatively warm Weddell Deep Water onto the continental shelf [*Nøst et al.*, 2011; *Hattermann et al.*, 2014]. Eddies affect approximately one third of the Antarctic overturning circulation; the rest is wind-driven [*Thompson and Heywood*, 2014]. Likewise, along the west Antarctic Peninsula, intrusions of warm Upper Circumpolar Deep Water on the shelf are dominated by eddy processes [*Moffat et al.*, 2009; *Martinson and McKee*, 2012]. This effect may occur at locations that are favorable to deep water formation all around the continent [*Stewart and Thompson*, 2015].

One of the main hypotheses of the PRISM-RS project (Section 2.2.1) is that mesoscale eddies, due to their demonstrated physical effects on mixing, advection, and vertical transport of nutrients, would have a similar impact in the Ross Sea, specifically on the transport of the limiting nutrient dissolved iron (dFe) to the surface ocean. The main objective of this chapter is determine the expected scope and behavior of mesoscale eddies in the Ross Sea, represent them in a regional ocean model, and estimate their net effects using an energy budget and eddy tracking software. The direct impacts of mesoscale eddies on the supply of dFe is presented later in Chapter 6.

4.2 EDDY THEORY

A key parameter to consider when examining eddy dynamics is the Rossby radius of deformation, the horizontal scale at which rotation effects are as important as buoyancy effects:

$$a = \frac{c}{|f|}. \quad (3)$$

Here f is the Coriolis frequency and, in the barotropic case, c is the gravitational wave speed. For baroclinic applications in a stratified water column, c is a function of the baroclinic mode and can be estimated following *Chelton et al.* [1998]:

$$c_m = \frac{1}{m\pi} \int_{-H}^0 N(z) dz, \quad (4)$$

where N is the buoyancy frequency, H is the total water column depth, and m is the baroclinic mode.

A second key definition in eddy dynamics is the mesoscale. Dynamically, the mesoscale is the horizontal scale at which the flow is quasi-geostrophic, turbulence is two dimensional, and non-hydrostatic effects are small. Following *McWilliams* [2008], mesoscale eddy flows have small Rossby numbers, Froude numbers, and aspect ratios. A lower limit on the mesoscale can be set by the aspect ratio, which is the water depth over the horizontal length scale. To keep the aspect ratio small in the Ross Sea, where typical on-shelf depths are around 500 meters, the length scale should be at least 5 km. It is less straight forward to set an upper limit to the mesoscale. Considering that, non-dynamically, the mesoscale is used to refer to processes smaller than basin scale, an appropriate upper limit for the Ross Sea is an order of magnitude below the width of the continental shelf, or around 100 km. Thus, for the purposes of this chapter, the mesoscale is defined to be the horizontal scale between 5 and 100 km. Note that, for the Ross Sea continental shelf (average depth of 500 m and average latitude of 75°S), the barotropic radius of deformation is approximately 500 km, putting it outside this operational definition of mesoscale.

4.2.1 EDDY SCALES

There are several classic baroclinic instability problems (e.g. *Charney* [1947]; *Eady* [1949]) that examine the progression and behavior of instabilities formed under specific, idealized circumstances. In general, in the strongly unstable limit, the horizontal scale at which the eddy forms, and the approximate duration of the eddy, can be predicted as a function of the mean state [*Smith and Vallis*, 2002]. The scale of eddy formation is directly related to the radius of deformation. For example, in the Eady problem [*Eady*, 1949], the most unstable wavelength is four times the radius of deformation, while in the Charney problem [*Charney*, 1947], it is the same as the radius of deformation. Observations using satellite data confirm this scale, showing a kinetic energy source near the radius of deformation [*Scott and Wang*, 2005], and an ocean eddy size around 2-5 times larger than the scale of the most

unstable waves [*Stammer*, 1998].

Time scales of eddy duration are more difficult to determine. They are directly proportional to the radius of deformation and inversely so to the mean flow speed (see *Vallis* [2006] for a comprehensive overview of instability problems and associated scales), but this assumes a steady state system, where energy put into eddies is replenished in the mean flow, and eddies do not travel to another region, i.e., there are no non-local effects. Global observations of eddies [*Chelton et al.*, 2007] show eddy durations of weeks to months, with a few exceptions. Notably, almost half of eddies poleward of 10° last for less than three weeks, but Meddies (generated from Mediterranean inflow into the North Atlantic) can persist for years.

4.2.2 ENERGY CASCADE

Energy in the ocean is exchanged at all scales. The classic view on energy cascade is that energy travels from large scales to smaller scales through nonlinear turbulent interactions and the breaking of internal waves until it dissipates. This transfer is necessary to maintain a balance with energy input from winds, surface heating, and tides. However, energy in mesoscale ocean eddies also moves in an inverse cascade, from high mode baroclinic eddies to low mode baroclinic eddies, and then from low mode baroclinic to barotropic [*Ferrari and Wunsch*, 2009]. The transfer to a lower mode occurs when a baroclinic eddy reaches the size of the radius of deformation for its current mode [*Charney*, 1971]. Non-uniform stratification interferes with this processes, causing the transfer of energy between modes to be less direct and efficient and leaving the energy concentrated around the radius of deformation [*Smith and Vallis*, 2001]. The general theory of geostrophic turbulence and the inverse energy cascade does not take into account interactions with topography and the presence of large scale potential vorticity gradients (such as near an ice shelf front) that can modify the energy cascade [*McWilliams*, 2008].

4.2.3 APPLICATION TO ROSS SEA

The expected horizontal scale, duration, and energy cascade behavior for eddies in the Ross Sea cannot be explicitly determined from geostrophic turbulence theory. However, considering the general conclusions and the specific state of the Ross Sea, it is possible to estimate expected eddy behavior. The Ross Sea continental shelf can be considered to have two main states: a mostly barotropic state that dominates when deep mixing is stimulated on-shelf due to sea ice formation and brine rejection or strong wind forcing in the absence

Month	Region	Min	Max	Mean
August	All	0.0 km	8.4 km	4.2 km
	on-shelf	0.0 km	4.1 km	1.7 km
	off-shelf	0.0 km	8.4 km	6.4 km
February	All	0.0 km	9.4 km	5.2 km
	on-shelf	0.0 km	5.1 km	2.5 km
	off-shelf	3.0 km	9.4 km	7.5 km

Table 5. Radius of deformation minimum, maximum, and mean for August and February in km. Corresponds with Figure 14.

of ice, and a mostly baroclinic state when the water column re-stratifies after deep winter convection, typical in summer. There is very little theoretical background for the behavior of eddies in a system that switches between mostly barotropic and mostly baroclinic; *Smith and Vallis* [2002] notes that the ratio of barotropic to baroclinic energy is reduced as the pycnocline becomes stronger and stratification is surface intensified. Thus, while the mostly barotropic state is expected to have relatively more barotropic energy, it is best to treat the two states as separate systems and analyze them individually.

The radius of deformation (equation 3), which determines the horizontal scale of eddy formation, is calculated for the first baroclinic mode using the Gibbs Seawater Toolbox [*McDougall and Barker*, 2011] to determine N and equation 4 with $m = 1$ to determine the velocity. Output from simulation 5 is used to obtain density profiles for calculating N for August (mostly barotropic) and February (mostly baroclinic) conditions, and the spatially varying radius of deformation is shown in Figure 14. Spatially, there are two distinct regions with differing radii of deformation: off-shelf, and on-shelf (including the ice shelf cavity). These regions appear in a histogram as a bimodal distribution (Figure 14 insets), where the mean of each approximately corresponds with one of the peaks (compare with Table 5). In general, a is smaller in the mostly barotropic state (August) than the mostly baroclinic state (February) for the entire model domain as well as in the on-shelf and off-shelf regions separately (Table 5).

In general, the expected eddy size at the time of formation is anywhere from 0 km up to 40 km (off-shelf in February, with a potential eddy scale four times the radius of deformation). Locations with $a = 0$ indicate places where baroclinic eddies cannot form. The lack of stratification in the water column restricts the transfer of potential energy to eddy kinetic energy when instabilities form. Based on the dynamic definition of mesoscale, eddies that are smaller than 5 km fall into the submesoscale regime, where turbulence is no longer quasi-2D

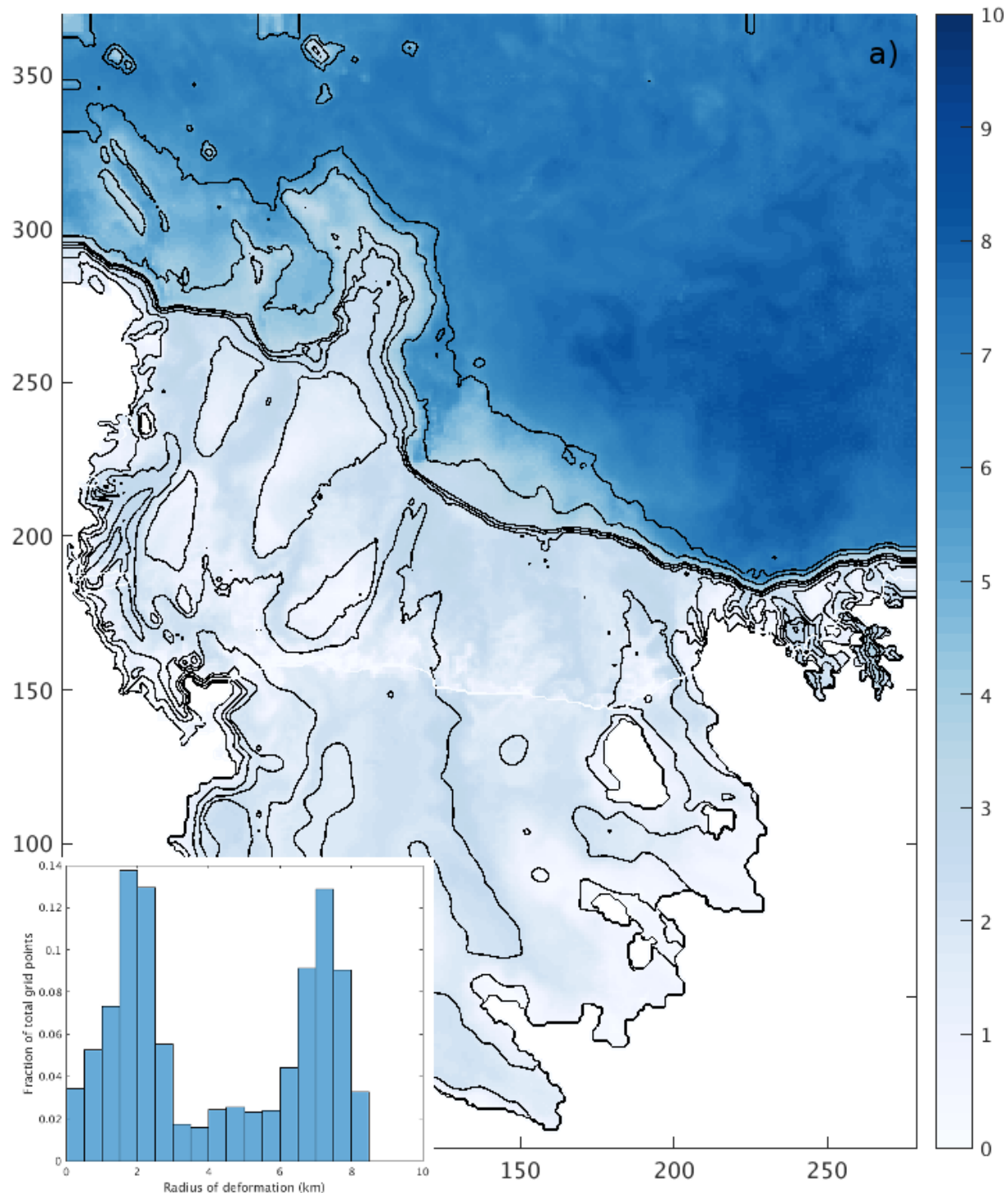


Figure 14. Radius of deformation (km) calculated from simulation 5. Inset shows histogram of values over model domain. a) August 15, 2011. b) February 15, 2012.

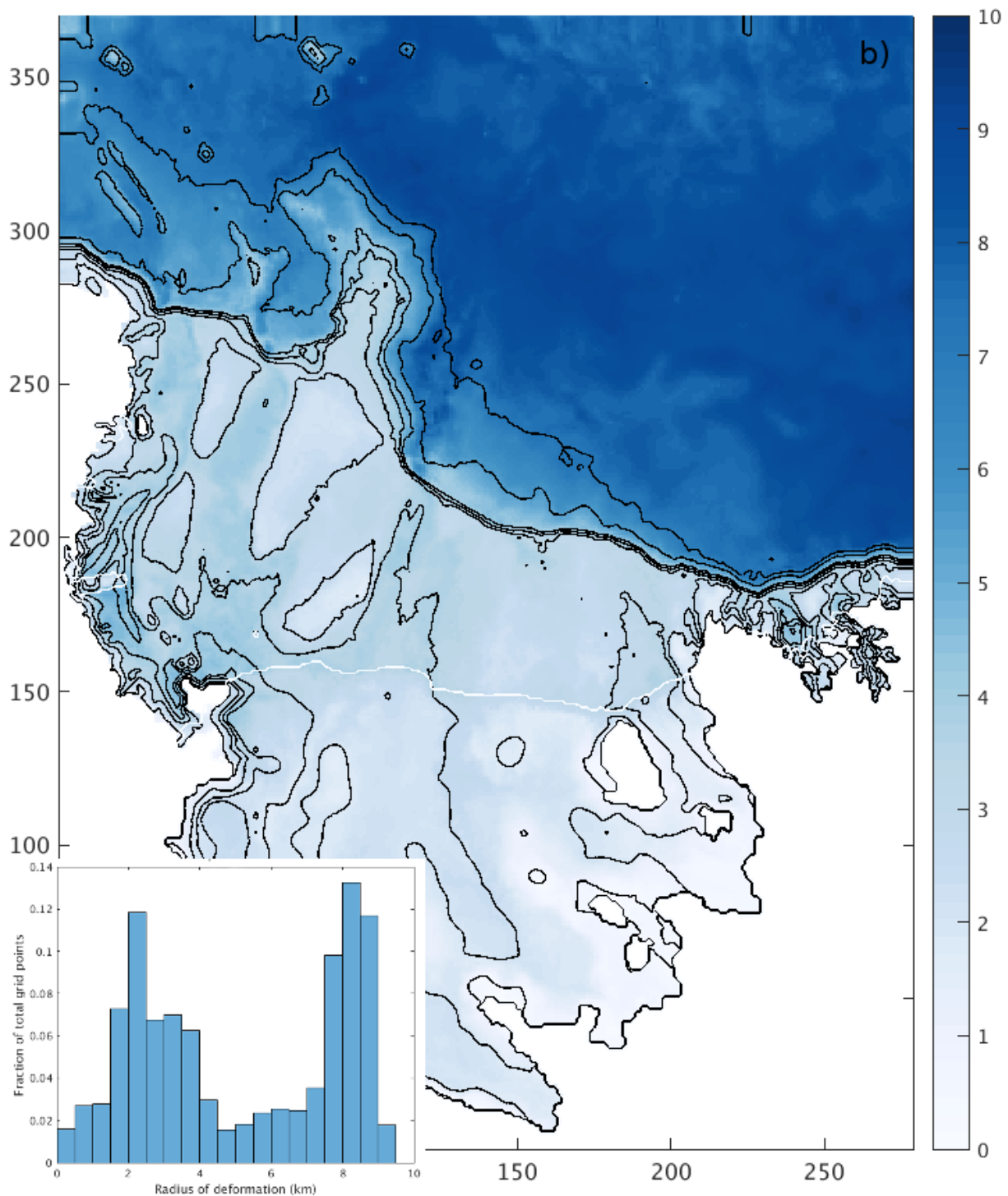


Figure 14. Radius of deformation (km) calculated from simulation 5. Inset shows histogram of values over model domain. a) August 15, 2011. b) February 15, 2012.

and vertical motion plays a significant role.

After formation, eddies in the Ross Sea can change size based on the direction of the energy cascade. Eddies that move away from their formation region to areas without energy sources will lose energy to friction and dissipation and break apart. Eddies that have access to an energy source, such as horizontal density gradients, mean flow kinetic energy, or energy from other eddies can experience the inverse energy cascade and grow, potentially transitioning from mode one baroclinic to barotropic.

Interactions with topography also can have a substantial impact on individual eddies. *Gille et al. [2000]* found that in the ACC, eddy kinetic energy was correlated with seafloor roughness at depths less than 3000 m, but anti-correlated at depths greater than 4800 m. Rough topography can produce variability in flow, creating instabilities or density gradients that fuel eddies, and it can also be a mechanism by which energy is dissipated. In the Ross Sea, notable topographic features include the shelf break, several large banks on the continental shelf, and the ice shelf front. The banks and the shelf break act to guide currents and eddies, while the sharp vorticity gradient at the ice shelf front is a barrier to eddies moving southwards.

Based on geostrophic turbulence theory and the physical geometry of the Ross Sea, we can estimate expected eddy behavior: Mesoscale eddies would form in the Ross Sea as first baroclinic mode eddies. Barotropic eddies have scales too large to fit on the continental shelf, and higher mode baroclinic would be sufficiently small and classified as submesoscale.

The weak stratification (low radius of deformation) over much of the Ross Sea indicates there is not much potential energy available to sustain or grow eddies, particularly if they leave their area of formation. If the first mode baroclinic eddies experience an inverse energy cascade and transition to barotropic, they may last longer, as there are strong currents around topographic features to provide mean flow kinetic energy.

The shelf break and ice shelf front act as potential vorticity barriers to eddies traveling southwards, although eddies can be generated along the barrier and break away to the south, or can move northward across the barrier. The abruptness of the ice shelf front makes it a more significant barrier than the shelf break. As stronger currents indicate higher kinetic energy and potentially fronts with horizontal density gradients (i.e., available potential energy), eddies will most likely appear and be sustained in regions with faster flow. This includes along the shelf break, along the ice shelf front and western coast, and along the north-south pathways on the sides of the banks.

4.2.4 MODELING CONSIDERATIONS

There are two main ways that ocean models include eddies: fully resolving them, or parameterizing their effects. To fully resolve an eddy of a given size, at least two grid points per radius of deformation are needed [Hallberg, 2013]. For any horizontal model grid, there will exist eddies and instabilities at smaller scales than the grid can resolve. Eddy parameterizations are used to approximate the effects of eddies that are not resolved. Perhaps the most famous example is the parameterization from *Gent and McWilliams* [1990] that introduces eddy advection effects in coarse resolution models [*Gent et al.*, 1995].

Considering the Ross Sea model and the appropriate definition of mesoscale for this specific application (5 to 100 km), at least two grid points per 5 km are needed to resolve mesoscale eddies. A horizontal grid spacing of 1.5 km is sufficient to resolve the smallest scale mesoscale eddy. Note that a substantial portion of the model domain (mostly on-shelf and under the ice shelf) is still not eddy-resolving (48% in August, 33% in February, based on the first baroclinic mode radius of deformation). Eddy formation in these regions is expected to be submesoscale in character, and as the ROMS framework is not non-hydrostatic, the dynamics may not be accurately represented even if the resolution were high enough to resolve eddies in these locations. A grid spacing of 5 km is used as a point of comparison, as it still resolves a large portion of the mesoscale size range, but does not resolve eddies around the first baroclinic radius of deformation (100% non-resolving in both August and February).

Another concern in modeling oceanic eddies is handling excess energy at scales equal to or slightly greater than the horizontal resolution. At these scales, energy sources include computational round-off errors, and unresolved eddies. Eddies that are not resolved will still try to form in the model, but the signal will be aliased to the nearest grid points, creating perturbations in flow rather than coherent vortices. Without a resolved pathway for an inverse energy cascade, these perturbations can grow in an un-physical manner. This necessitates an energy removal mechanism to account for both the unresolved eddies and the computational round-off.

In the ROMS model framework, this is accomplished by setting a dissipation parameter that is a function of grid spacing. There is also dissipation inherent in the 3rd order upwind scheme. The goal in setting this dissipation rate is to have it high enough to remove excess energy and keep the model stable, but also have it as low as possible to avoid excess dissipation at larger scales. In this specific application of ROMS, I use a Laplacian horizontal diffusion with $\nu = 5.0 \text{ m}^2 \text{ s}^{-1}$. From this, we can estimate a spin down time τ as a function

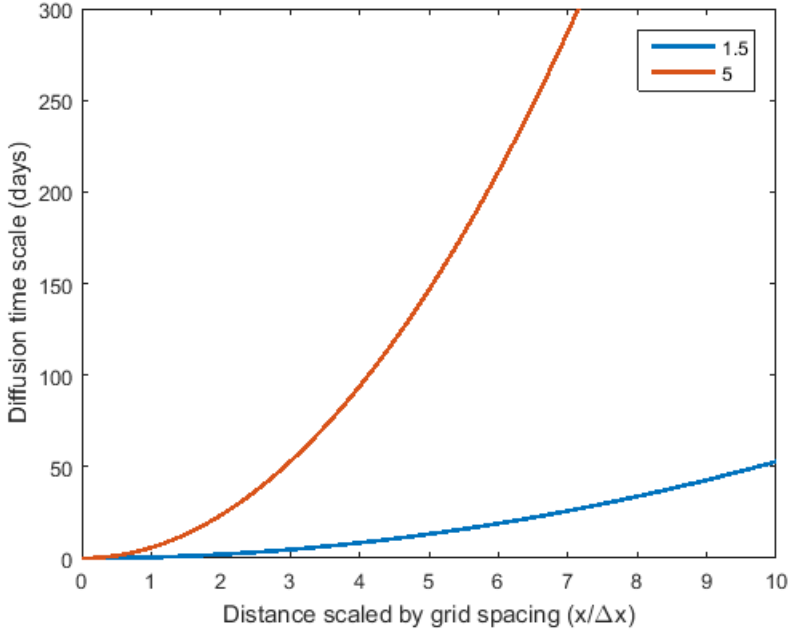


Figure 15. Diffusion time scales: Equation 5 plotted as a function of horizontal distance scaled by grid spacing ($x/\Delta x$) for 1.5 and 5 km grids.

of horizontal grid spacing, Δx :

$$\tau = \frac{\Delta x^2}{\pi^2 \nu}. \quad (5)$$

By using the same value of ν for the 1.5 and 5 km grids, the diffusion between grids is the same for a given size wave, i.e., an energy perturbation with a wavelength of 15 km will have the same diffusion time and rate. However, as a function of number of grid points, the 1.5 km grid has more diffusion: e.g., the $4\Delta x$ wave diffuses over time scales of around 8 days at 1.5 km grid spacing, but closer to 90 days at 5 km grid spacing (Figure 15).

The dissipation inherent in the 3rd order upwind scheme is somewhat more difficult to quantify. The scheme used in ROMS is based on UTOPIA [Rasch, 1994], with modifications as described in *Shchepetkin and McWilliams* [2005]. *Shchepetkin and McWilliams* [1998] analyze the dissipative nature of a number of schemes, including UTOPIA, in a two-dimensional turbulent flow. UTOPIA's dissipation scheme, which is scale-selective and depends on local velocity, is similar to hyperdiffusion and is dependent on the fourth derivative of the advected field. *Shchepetkin and McWilliams* [1998] show that UTOPIA performed well in tests, producing a smooth, physically meaningful solution and appropriately dissipating excess turbulence. However, they note that while dissipation in UTOPIA follows the general

principles of inverse energy cascades as found in two-dimensional turbulence, the general principles apply on average over an entire domain, while a scheme like UTOPIA applies at individual grid points.

In general, the third order upwind scheme used in ROMS is appropriate for this application, having been shown to work well in modeling two dimensional turbulent flows [*Shchepetkin and McWilliams, 1998*]. The scale-selective property of the scheme indicates that it follows the same general pattern as the explicitly set values of dissipation in ROMS: energy at smaller scales is dissipated more quickly than energy at larger scales. There is a possibility that the combined dissipation of the explicit parameter dissipation (although low) and the third order upwind scheme is enough to dissipate mesoscale eddy energy at small scales without allowing the eddy to form; i.e., the number of eddies represented by the model may be an underestimate and may be biased towards larger eddies. In future, tests could be done to determine the extent of the effect of the third order upwind scheme dissipation on eddy formation rates by using simulations with different schemes; although the change in order also changes the scheme-associated truncation error and may cause other complications.

4.3 METHODS

Theoretical predictions for eddies that form and propagate in the Ross Sea indicate that at many regions in the Ross Sea and depending on the time of year, mesoscale eddy formation rates are expected to be low. This, coupled with the dissipation scheme in ROMS, raises an important issue: do more eddies form in simulations of the Ross Sea at higher resolution? The amount of eddy activity in the Ross Sea in simulations **5** and **1** can be estimated by calculating the energy budget, and by explicitly tracking eddies using sea surface height and considering relative vorticity.

4.3.1 KINETIC ENERGY

The total mechanical energy in a given ocean volume can be considered to be the sum of kinetic (KE) and potential energy. Changes to the total energy over time are caused by energy flux through the boundaries of the volume or by internal energy dissipation. Calculating a total energy budget using simulation output is a non-trivial task [*MacCready and Giddings, 2016*], as energy and volume are not necessarily conserved in the discretized governing equations, and are subject to machine precision and round-off. For the purposes of this study, I focus on the distribution of KE in both baroclinic and barotropic states, and

in the time-mean and eddying component.

The standard formulation of KE at any grid cell in a four dimensional model is written as

$$KE(x, y, z, t) = \frac{1}{2} \mathbf{u}(x, y, z, t) \cdot \mathbf{u}(x, y, z, t), \quad (6)$$

where $\mathbf{u}(x, y, z, t)$ is the standard three dimensional velocity vector. We can decompose \mathbf{u} into a depth-mean and a residual, i.e., a barotropic and baroclinic velocity:

$$\mathbf{u}(x, y, z, t) = \langle \mathbf{u} \rangle_z(x, y, t) + \mathbf{u}_z(x, y, z, t). \quad (7)$$

(Note that $\langle \rangle_z$ indicates a mean in the z direction while $_z$ indicates residuals from the mean in the z direction.) Decomposing velocity in this fashion allows the separation of baroclinic and barotropic kinetic energy. We can further decompose the velocity into time-mean and time-average components, to separate eddying flows from the mean flow, i.e.,

$$\langle \mathbf{u} \rangle_z(x, y, t) = \overline{\langle \mathbf{u} \rangle_z}(x, y) + \langle \mathbf{u} \rangle'_z(x, y, t), \quad (8)$$

where the overbar represents a temporal mean and $'$ represents residuals.

Then, KE can be re-written as $KE = KE_{BT} + KE_{BC} + KE_I$, with the barotropic kinetic energy KE_{BT} given as the sum of mean ($\overline{KE_{BT}}$) and eddy (EKE_{BT}) barotropic kinetic energy:

$$KE_{BT}(x, y, t) = \overline{KE_{BT}}(x, y) + EKE_{BT}(x, y, t) \quad (9)$$

$$= \frac{1}{2} \overline{\langle \mathbf{u} \rangle_z}(x, y) \cdot \overline{\langle \mathbf{u} \rangle_z}(x, y) + \frac{1}{2} \langle \mathbf{u} \rangle'_z(x, y, t) \cdot \langle \mathbf{u} \rangle'_z(x, y, t); \quad (10)$$

likewise the baroclinic KE_{BC} as

$$KE_{BC}(x, y, z, t) = \overline{KE_{BC}}(x, y, z) + EKE_{BC}(x, y, z, t) \quad (11)$$

$$= \frac{1}{2} \overline{\mathbf{u}_z}(x, y, z) \cdot \overline{\mathbf{u}_z}(x, y, z) + \frac{1}{2} \mathbf{u}'_z(x, y, z, t) \cdot \mathbf{u}'_z(x, y, z, t). \quad (12)$$

The last term is the kinetic energy interaction term, KE_I , and includes interactions between barotropic and baroclinic flow, as well as between the time-varying and time-mean flow. As these interactions are not of interest in this study, they are all lumped into one term. A similar decomposition of KE into specific parts is done in *Chen et al. [2016]*, but focused solely on the time mean and residuals.

When comparing simulations at different horizontal resolutions, the total volume of water considered is not necessarily the same. Thus, all the KE terms are calculated for each individual grid box, and then averaged per unit volume:

$$\frac{1}{V} \sum KE\Delta V, \quad (13)$$

where $\Delta V = \Delta x \Delta y \Delta z$ is the volume of each grid box, and V is the total volume.

4.3.2 EDDY TRACKING

Another way to estimate eddy activity is to directly count individual eddies in a simulation. There is no universal standard used to define what constitutes an eddy, although there are several often-used methods based on SSH, vorticity, or a combination of both (i.e., the Okubo-Weiss parameter [*Chelton et al.*, 2007; *Isern-Fontanet et al.*, 2003]). For this study I use a Matlab function designed to track eddies by SSH [*Gaube and McGillicuddy Jr.*, 2017], which was modified to work with simulation output in x/y coordinates instead of lat/lon. To define an eddy, a series of criteria must be met:

1. The eddy must persist for at least four consecutive days.
2. SSH of the eddy must be at least 1 cm different from the background.
3. There must be at least 21 grid points contained within an eddy. This corresponds to five points across the diameter of the eddy.
4. The maximum diameter of the eddy is 70 km. This includes all mesoscale eddies, but filters out larger eddies, or variations based on topography.
5. The maximum distance the eddy can travel in one day is 100 km. This corresponds to velocities slightly over 1 m s^{-1} , a reasonable estimate for the maximum velocity seen in the Ross Sea.

These criteria help ensure that the features identified by the eddy-tracking software actually are eddies, and that each eddy track corresponds to only one eddy.

Once an eddy is identified, it is tracked through the simulation, and statistics for individual eddies are recorded, including age, radius, amplitude of SSH, and start day. Eddies are also classified as cyclones (negative SSH; clockwise in the Southern Hemisphere), or anti-cyclones (positive SSH; counterclockwise in the Southern Hemisphere).

Relative vorticity at the surface is calculated to confirm that the eddy tracking software using SSH is identifying eddy-like features. This calculation follows that done by the ROMS software, assuming an adiabatic Boussinesq fluid where potential density is conserved. Relative vorticity (ζ) is given as

$$\zeta = \frac{dv}{dx} - \frac{du}{dy}, \quad (14)$$

absolute vorticity is $\zeta + f$, and potential vorticity (PV) is

$$PV = \frac{1}{\rho_o} ((\zeta + f) \cdot \nabla \rho), \quad (15)$$

where ρ is the density. Relative vorticity is used in this case, as it focuses solely on vorticity generated by the flow and does not include vorticity associated with location.

A limitation of using SSH criteria as opposed to relative vorticity is that the eddy analysis is restricted to eddies that have some expression at the ocean surface. Deep baroclinic eddies would not be identified or tracked using this method. However, we avoid mis-identifying other vorticity features, such as the large potential vorticity gradient at the ice shelf front, as eddies.

4.4 RESULTS AND DISCUSSION

4.4.1 KINETIC ENERGY

Kinetic energy components, including barotropic, baroclinic, time mean, and EKE, are calculated for simulations **1** and **5** for the months of August (winter) and February (summer). Here the analysis is restricted to on-shelf locations, not including under the ice shelf. Including off-shelf waters leads to similar results and conclusions. Variations of these components over each month (Figure 16) appear to be driven by simulation forcing and do not vary when the horizontal resolution is changed. Each simulation in both August and February follows the same general trend: most of the KE is barotropic, not baroclinic, and of each of these, the time mean and EKE components are of similar magnitude (Figure 17). The interaction KE term is non-zero throughout each month, but the monthly average is less than 0.02%.

The KE differences between simulations generally follow the expectations: increasing horizontal resolution increases the total amount of KE, in both August and February. This average increase is more pronounced in August (20%) than in February (5%), although the total KE is larger in February than in August for both simulations. Breaking the increase

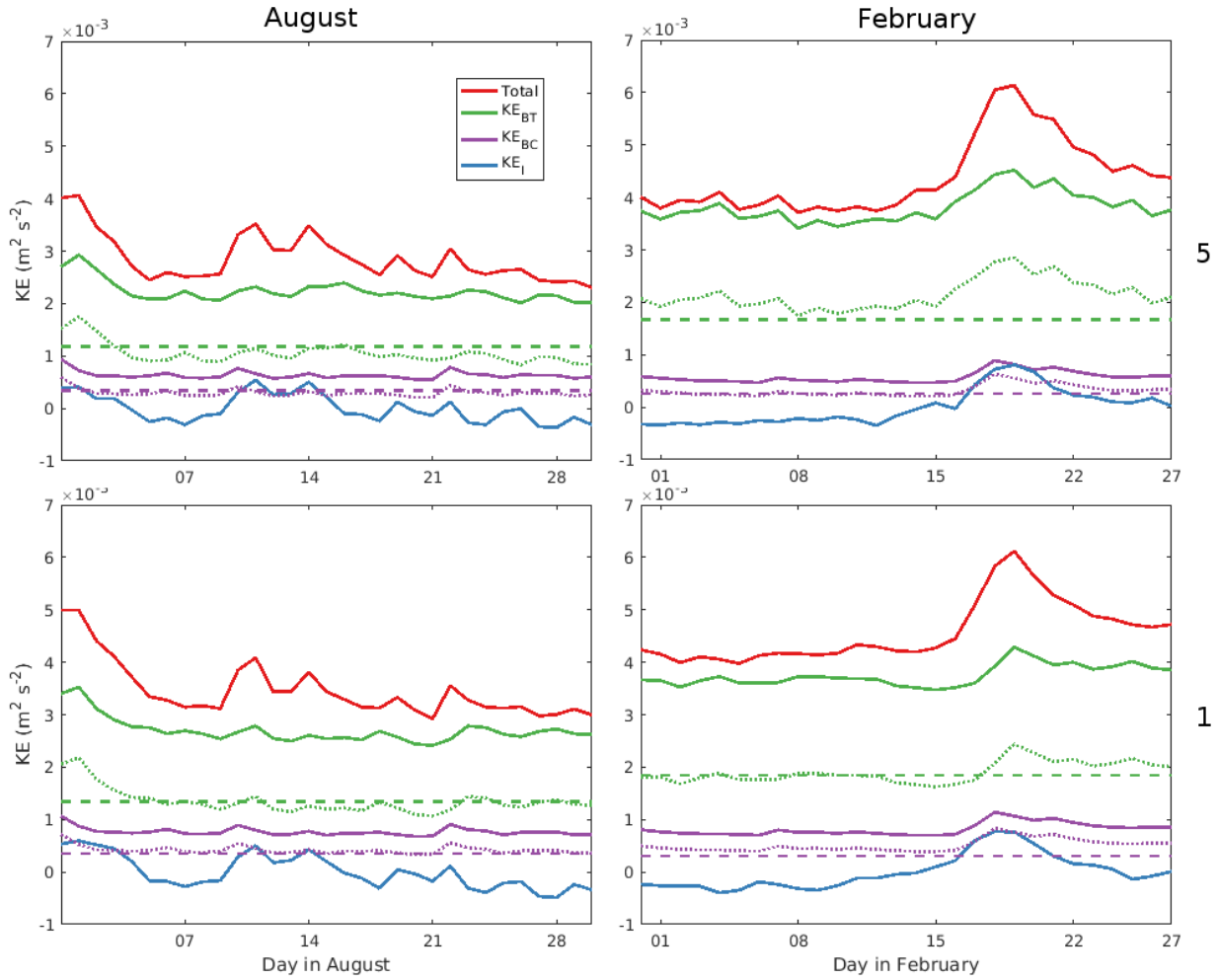


Figure 16. Kinetic Energy (normalized by volume) for simulations 5 and 1 in February and August on the continental shelf. Solid lines are the KE from each component: overall total, barotropic, baroclinic, and the interaction term. Barotropic and baroclinic KE are further split into time mean (dashed) and time varying (dotted) portions.

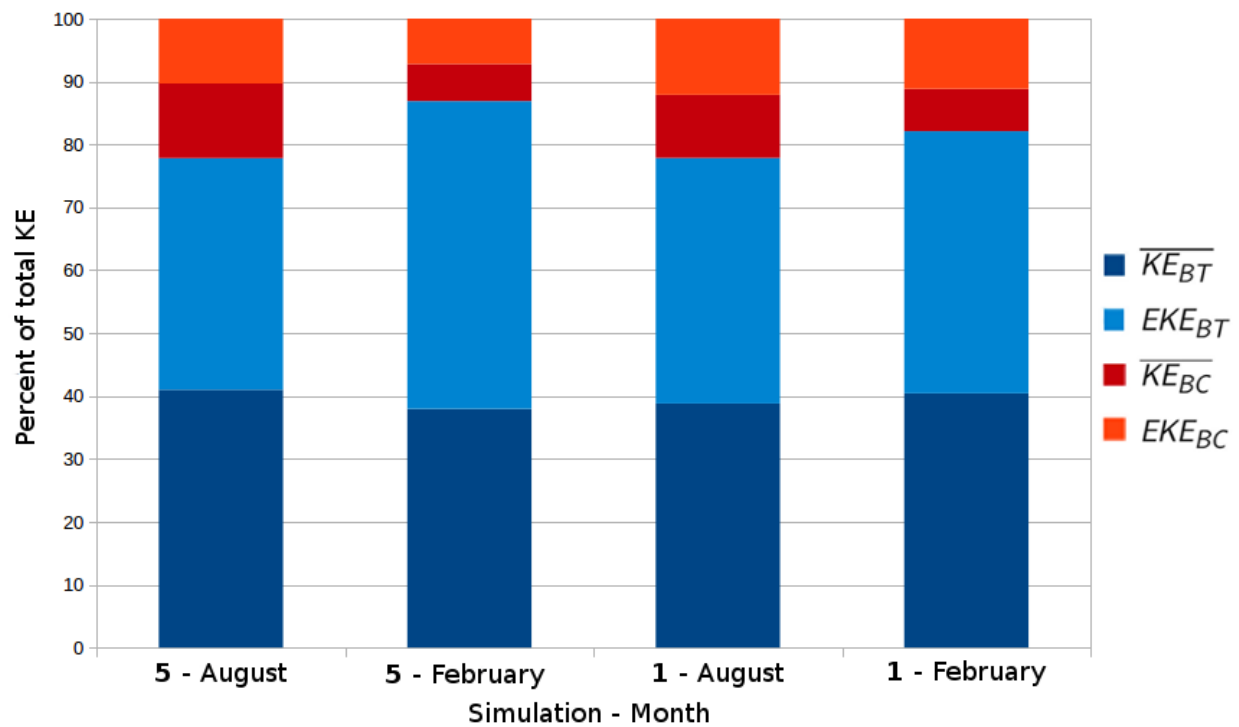


Figure 17. The percent of total KE contained in each component (barotropic time mean KE; barotropic EKE; baroclinic time mean KE; baroclinic EKE) for simulations 5 and 1 averaged over August and February. Note that the interaction KE term contributes less than 0.02% for each and is not shown.

in KE down by component gives a more nuanced picture. In February, there is no change in barotropic KE between simulations. The average barotropic KE increases slightly, but is offset by a decrease in barotropic EKE. In August, the barotropic KE increases by 23% with increasing resolution, a change which is mostly seen in an increase in barotropic EKE (of about 27%). For baroclinic KE, there is an increase in both August and February (21% and 42%, respectively), which is dominated by the baroclinic EKE component (42% and 61% increase, respectively).

Contrary to expectations, the amount of baroclinic KE, both absolute and relative, is less in February for both simulations than in August (Figures 16 and 17). February is typically a time of increased stratification before deep winter mixing driven by brine rejection from sea ice. It is likely that the increased stratification in February leads to more energy generation, and thus more overall EKE. The inverse energy cascade and the eddy sizes permitted by the model resolution would preferentially select eddies that cascade to barotropic eddies, and dissipate energy from smaller baroclinic eddies. Overall, the distribution of KE between baroclinic and barotropic states matches well with the low stratification in the Ross Sea, with 75% or more of kinetic energy in barotropic form (Figure 17).

4.4.2 EDDY TRACKING

Over the last year of simulation, SSH was used to identify and track eddies, following the criteria listed in Section 4.3.2. Overall, 780 eddies were tracked in simulation **5**: 404 anti-cyclonic eddies and 376 cyclonic, and 1257 eddies were tracked in simulation **1**: 578 anti-cyclonic and 679 cyclonic. While there are more eddies present in simulation **1**, the general regions containing eddy tracks are similar to those in simulation **5** (Figure 18). Eddy tracks follow major topographic features, including the shelf break, the ice shelf front, and bathymetric channels on the shelf. Generally, these topographic features are characterized by higher flow rates, and thus higher energy. There is a significant lack of eddies in the off-shelf region and under most of the ice shelf for both simulations.

The characteristics of the eddies tracked in both simulations are also quite similar (Figure 19). Eddy radii are most frequently between 15 and 20 km in **5**, and between 10 and 15 km in **1**, and are limited by the smallest eddy each simulation can properly resolve. The same holds true for eddy height: there are relatively more smaller eddies (<2 cm) than larger ones in simulation **1**, than in simulation **5**. Both these statistics illustrate that the dynamics of the model try to generate small eddies, but is limited by the horizontal resolution. As the baroclinic radius of deformation is very small on the shelf and not all areas of the model

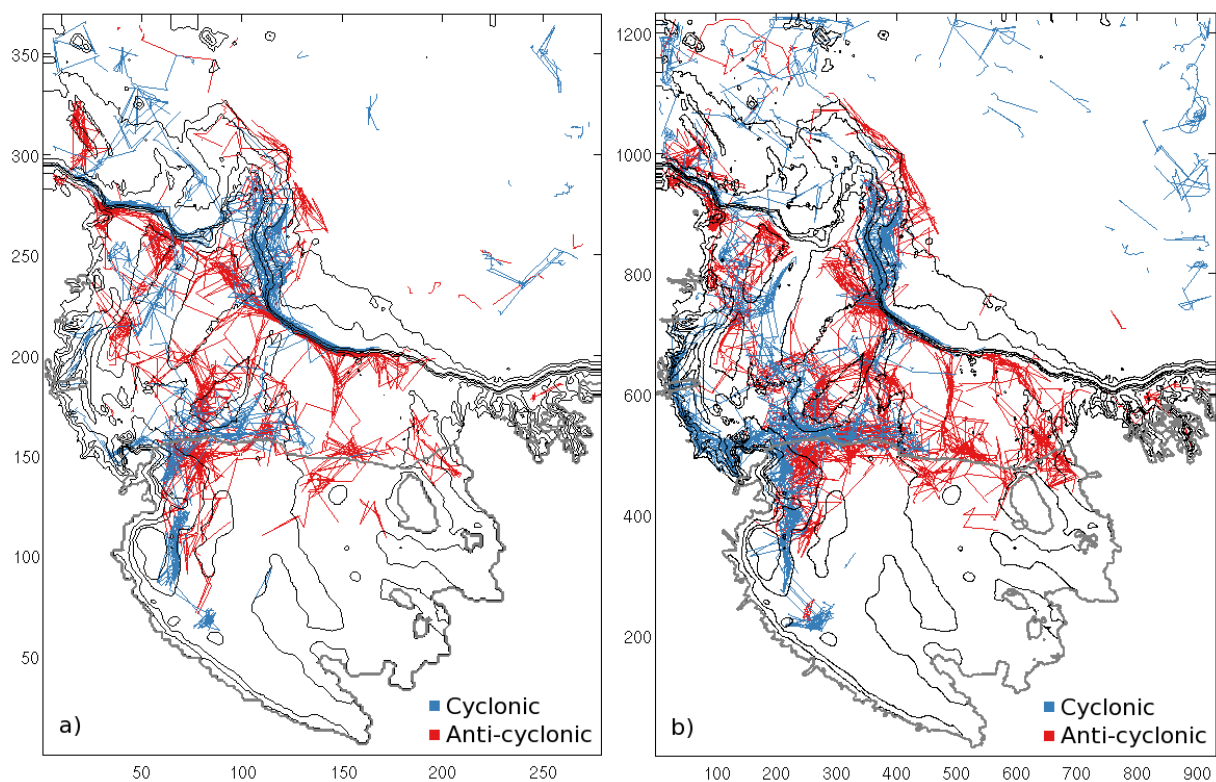


Figure 18. Map of eddy tracks during the last year of simulation for simulation 5 (a), and 1 (b). Black lines are bathymetry, gray line is ice shelf front.

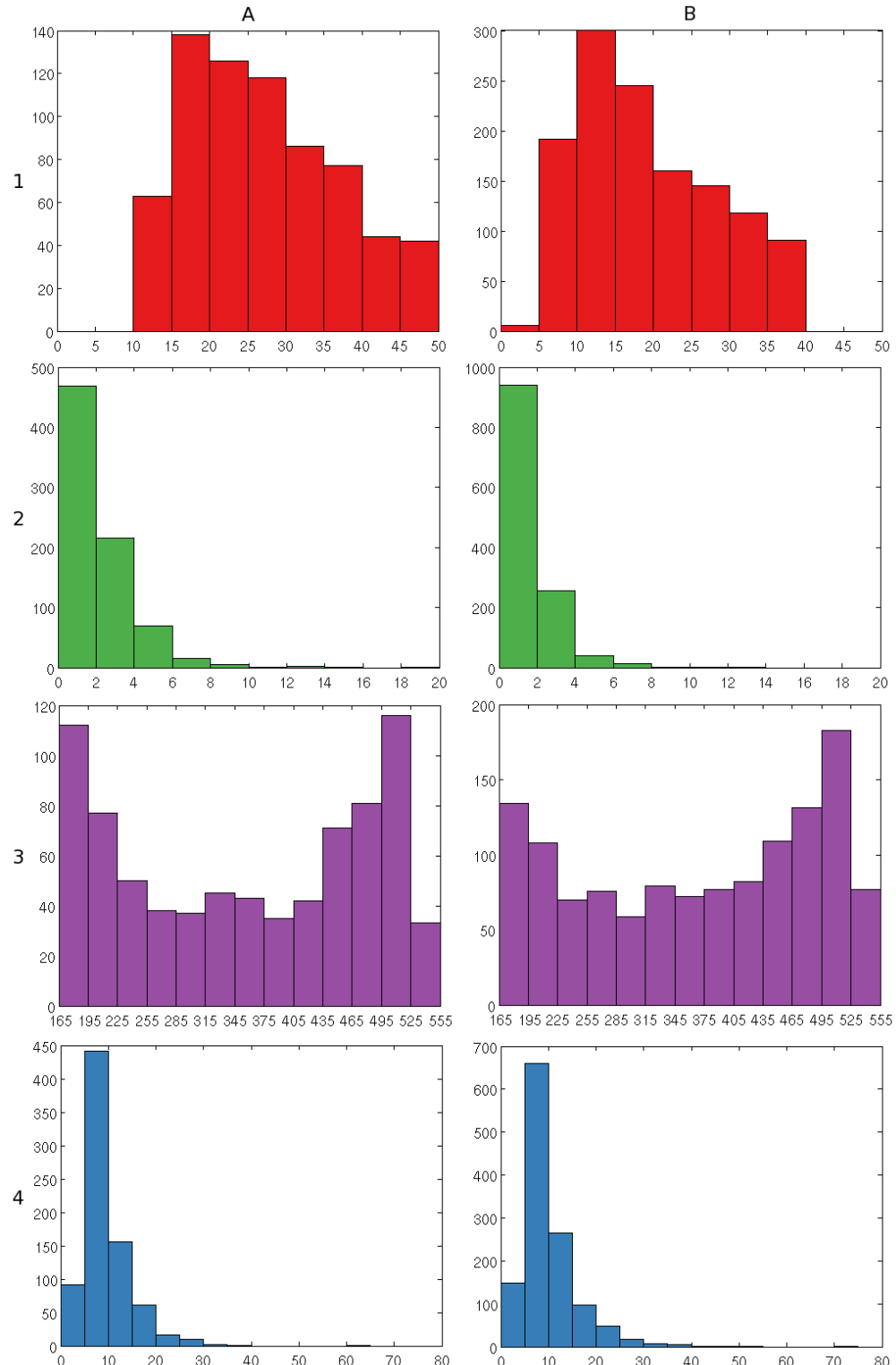


Figure 19. Histograms of eddy characteristics for the last year of simulation for **5** (column A) and **1** (column B). Rows are: 1) Eddy radius (km); 2) Eddy height (cm); 3) Model day eddy first appeared; 4) Number of days the eddy persisted.

domain can be considered eddy-resolving at all times, it is likely that a further increase in horizontal resolution will increase the number of eddies.

Throughout the year, eddies are most frequently generated in the summer time, and less so in the winter, due to the increased stratification and increased radius of deformation during the summer months. The majority of eddies persisted for between 5 and 10 days, although some remained longer, including a few surviving for around two months. This relatively short life of mesoscale eddies in both simulations could be due to a lack of available energy, too much parameterized energy dissipation in the model at small scales, or a combination of both. In general, the statistics of the eddies generated in these simulations matches well with what was expected, given both the physical state of the Ross Sea, and model behavior.

To analyze the appropriateness of defining eddies by SSH, eddies identified on two specific days, August 15, 2011, and February 15, 2012 (representing a winter and a summer day), are compared to simulation SSH, surface in-situ density, and vorticity (Figure 20). The results from August and February are very similar, with the exception that more eddies are identified in February; thus I show and discuss only those results from February.

Eddy contours, as identified by the SSH tracking software, tend to be irregular in both simulation **1** and **5**, and based on the constraints, are typically smaller in simulation **1**. Snapshots of SSH and in-situ density (Figure 20, top and center) are similar on the large scale, showing the same large scale patterns of variation over the same range of values. The smaller variations, driven by eddies and smaller scale instabilities, differ between the two. This is expected, as the higher horizontal resolution allows increased detail at small scales.

In general, eddies defined by the tracking software correspond with visible patterns in the SSH fields (Figure 20, top row). There are a few places where what appears to be an eddy is not identified, as the SSH anomaly for that spot is not above the 1 cm criteria. There are also a few eddies identified that have very small visible SSH signatures, indicating a weak eddy, or perhaps just an anomaly in the ocean surface. The density field associated with these eddies (Figure 20, center row) shows that there is not a strong link between density variations and eddies defined by SSH. Specifically, small patches of higher or lower density water are not defined as eddies, and in several cases, particularly along the shelf break, the eddies span water of varying density, indicating a stirring across density gradients.

Examination of the relative vorticity field (scaled by f , Figure 20, bottom row) shows relatively large values of relative vorticity, up to 50% of the local Coriolis parameter. Some eddies, particularly those along the shelf break, correspond to either a strong positive or negative relative vorticity, while other eddies include both positive and negative vorticity

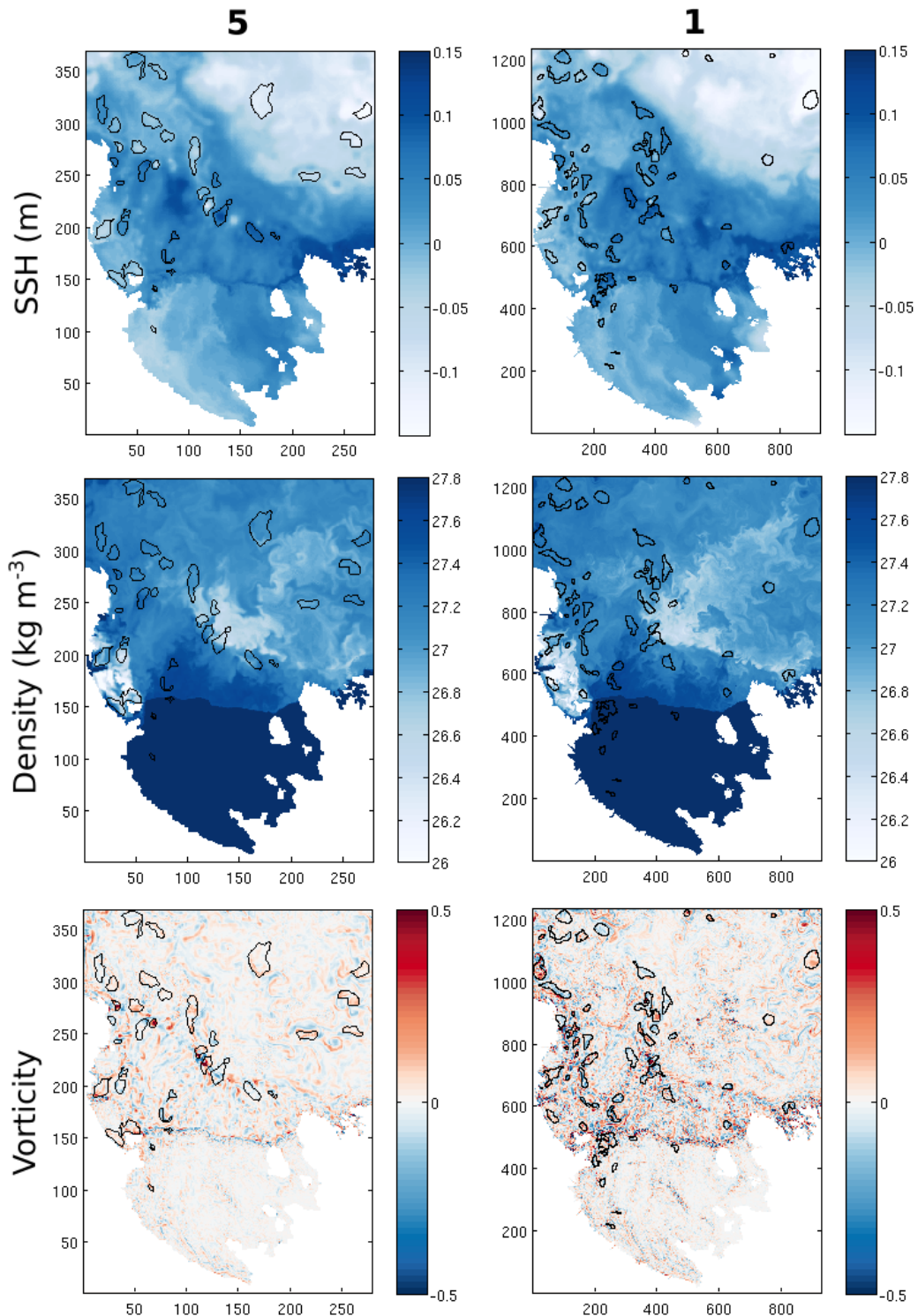


Figure 20. Eddies identified from the eddy tracking software (black contours) plotted over model variables (Sea Surface Height (SSH), in-situ density, and relative vorticity (scaled by coriolis parameter f)) for simulations **5** and **1** on February 15, 2012

values in their cores. The vorticity field indicates that there may be a few more eddies than identified purely by SSH, but there are also regions of strong vorticity patches, such as along the ice shelf front, that do not correspond to eddies. Given the general complexity of the vorticity field, using it to define eddies is not recommended in this application. A combination approach, such as the Okubo-Weiss method (e.g. [Isern-Fontanet *et al.*, 2003; Chelton *et al.*, 2007]), may be appropriate as well, but requires further research.

4.5 CONCLUSION

Two dimensional turbulence theory gives guidelines on the characteristics of mesoscale eddies that are expected to exist in the Ross Sea, as observations are limited, especially during austral winter. Water column stratification is very weak during winter months due to brine rejection from sea ice and strong wind forcing inducing deep mixing. The first mode baroclinic radius of deformation is therefore small, less than 10 km over the entire model domain. Eddies generated with sizes corresponding to the radius of deformation (at, or several times larger than) are not resolved on the continental shelf in simulation **5** and are barely resolved in simulation **1**. The weak stratification also indicates that there is little potential energy available to generate baroclinic eddies, even if resolved in simulations.

In general we find that the results from the simulations match the expected eddy characteristics. Despite the low eddy generation rate and small eddy sizes, there is more kinetic energy and about double the number of eddies in the higher horizontal resolution simulation **1** than in simulation **5**. As the model is designed to dissipate energy at smaller length scales more quickly, the kinetic energy is present in a more barotropic state than baroclinic, indicating that eddies generated around the first baroclinic mode radius of deformation are either dissipated or cascade to the barotropic mode.

The key result from this chapter is that despite the low prevalence of eddies in the Ross Sea and the low baroclinic radius of deformation, there is still a significant difference in the number of eddies generated in simulations at different horizontal resolution. Eddies generated in simulation **1** also tend to be smaller in size. Thus, comparisons between simulations at different resolutions can illustrate the effects of mesoscale eddies, specifically on the supply of dFe in Chapter 6.

It is still an open question if the eddy activity in the Ross Sea simulations compares reasonably well to actual eddy activity. However, there is yet to be developed an observational method that can detect and track eddies under sea ice during the winter months. Further future work for this research includes changing the tracer advection schemes in the model

to get a better idea of the amount of dissipation inherent in the third order upwind scheme. It is also likely that a further increase in horizontal resolution, although perhaps not cost-effective, may increase the number of eddies and the baroclinic kinetic energy by allowing smaller submesoscale eddies to form and cascade to larger, but still baroclinic, eddies.

CHAPTER 5

SEA ICE & TIDES

5.1 INTRODUCTION

Sea ice motion is forced by the atmosphere and the ocean through drag stresses at the upper and lower boundaries, respectively, modified by internal ice stresses and the presence of solid boundaries including coasts and ice-shelf fronts. Velocities of ice-mounted, satellite-tracked drifters show strong tidal signals in some regions (see, e.g. *Heil et al.* [2008]). At sufficiently low ice concentration (C_{ice}), the ice moves in free drift (i.e., internal ice stresses can be ignored), where the ice velocity is very close to the underlying ocean velocity [*Padman and Kottmeier*, 2000]. Therefore, if there is a periodic lateral divergence of surface tidal currents, sea-ice motion will also be periodically divergent. In-situ observations confirm this “ice accordion” behavior of sea ice [*Nansen*, 1898; *Geiger et al.*, 1998; *Eisen and Kottmeier*, 2000; *Heil et al.*, 2008]. The ice accordion can also be seen in RADARSAT wide-swath synthetic aperture radar data at high latitudes [*Kwok et al.*, 2003].

Although the tide-forced ice divergence is essentially periodic, numerical models indicate that this process has a net effect on time-averaged sea ice properties including C_{ice} and ice thickness h_{ice} (see, e.g., *Kowalik and Proshutinsky* [1994]). *Koentopp et al.* [2005] studied the effect on mean sea ice characteristics of adding tides to an atmospherically forced model of the Weddell Sea, where strong tidal motion of sea ice occurs over the continental shelf and upper continental slope [*Geiger et al.*, 1998; *Heil et al.*, 2008]. Oscillatory sea ice divergence (Δu_{ice}) reduced the modeled, time-averaged value of $C_{ice}(x, y)$ in some regions by up to $\sim 20\%$, changed mean ice thickness $h_{ice}(x, y)$ by up to ~ 0.5 m, and led to higher net annual ice growth. Coupling between tidal processes and the mean motion of the sea ice driven by the wind stress and oceanic flow led to modeled tidal effects being distributed well beyond the regions of strong tidal currents.

Given this modeled role of tides on mean sea ice characteristics, we seek an observational method for mapping tide forced sea ice divergence. *Padman and Kottmeier* [2000] proposed that strong tidal divergence in specific regions of the Ross Sea, notably along the continental shelf break, might be visible as locally low values of C_{ice} derived from daily-averaged SSM/I

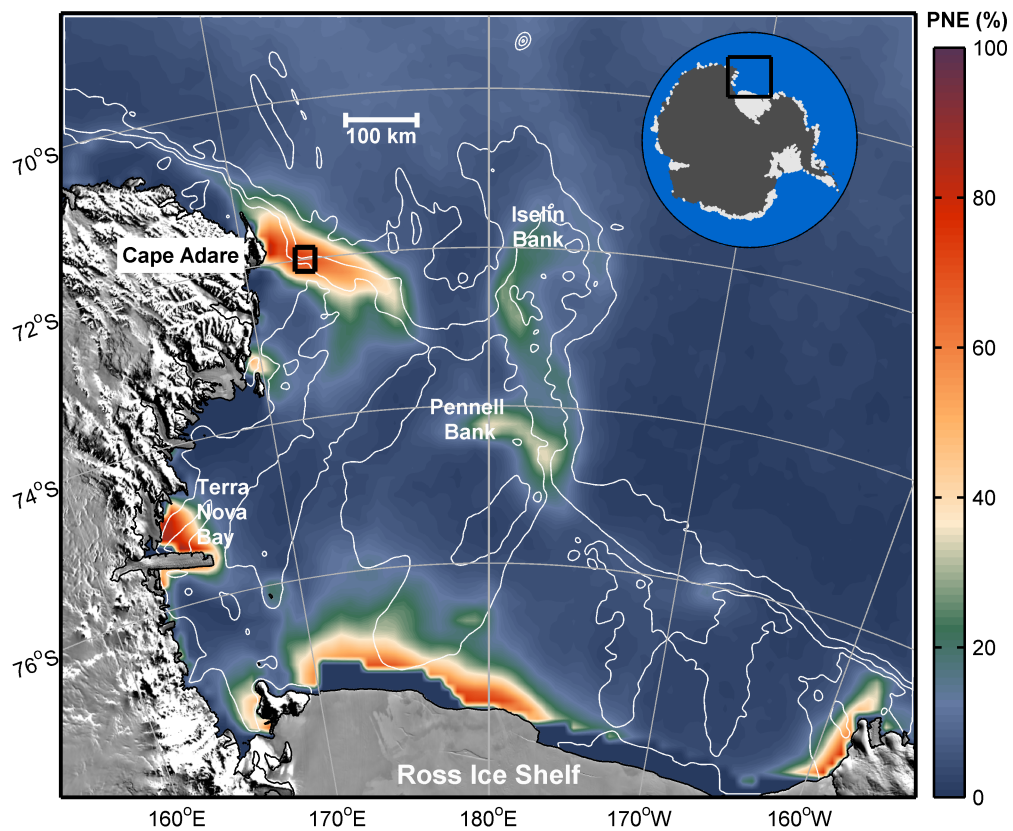


Figure 21. Probability of non-exceedance of sea ice concentration (C_{ice}) in the Ross Sea for a threshold of $C_{ice} = 0.95$ for all AMSR-E daily-averaged data for April–November inclusive, years 2002–2009. Data were processed with the NASA Team 2 algorithm [Markus and Cavalieri, 2009]. High values imply frequent occurrences of partial open water (leads or polynyas). White lines are 500, 1000, and 2000 m isobaths. The test site is indicated as a black box just to the east of Cape Adare, northwest Ross Sea.

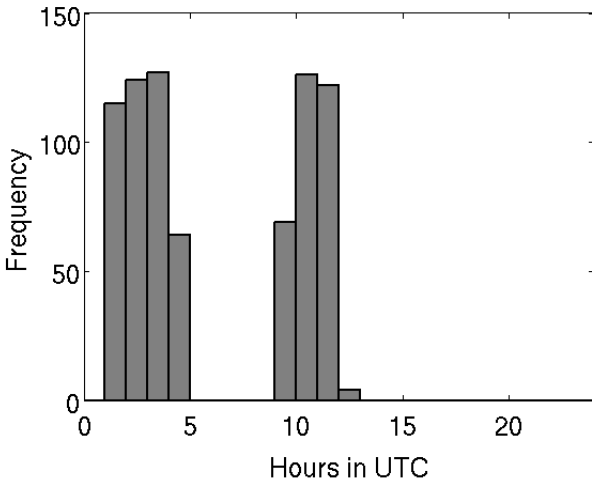


Figure 22. Frequency of swath passes over the study location over the course of 1 year. The irregular satellite sampling leaves 12 consecutive hours unsampled.

passive microwave satellite data. However, the fundamental periodicities of tides ($\sim 1/2$ and ~ 1 day) are not resolved by daily-averaged maps, and other processes may affect time averaged values of C_{ice} along the shelf break. Here, we report a novel method in which individual swaths of Advanced Microwave Scanning Radiometer - EOS (AMSR-E) passive microwave satellite data are used to develop time series of C_{ice} at high temporal resolution (several times per day) to allow detection of tidal variations of C_{ice} . The extensive winter sea ice pack (Figure 21) and large, spatially variable, tidal currents of the Ross Sea [Erofeeva *et al.*, 2005; Padman *et al.*, 2009] make it an appropriate location to test this new method. Output from a regional ocean model of the Ross Sea is validated with the new AMSR-E derived timeseries of C_{ice} and is further analyzed to determine tidally forced changes in surface heat fluxes and sea ice formation rates.

*Note to the reader: A majority of this work is published in Mack *et al.* [2013].*

5.2 DATA AND METHODS

We use Level 2 swath data that were acquired with the AMSR-E passive microwave sensor on the Aqua satellite [Parkinson, 2003]. These data are owned and distributed by the Japanese Aerospace Exploration Agency (JAXA) as part of the Earth Observing System (EOS). Level 2 swath data include values of C_{ice} derived with the modified Bootstrap sea ice concentration algorithm [Comiso, 2009], provided at a spacing of ~ 10 km across swaths that are ~ 1450 km wide [JAXA (Japan Aerospace Exploration Agency), 2006].

Constituent	Period (h)	Elevation (m)	Cross-slope current (m s^{-1})	C_{ice}	C_{ice} Synthetic
Long period					
MF	327.86	0.03	0.02	0.096	0.009
Diurnal					
O1	25.83	0.27	48.7	0.070	0.050
K1	23.96	0.22	30.6	0.046	0.033
P1	24.00	0.09	9.9	0.006	0.007
Semidiurnal					
M2	12.42	0.09	0.7	NS	NS
S2	12.00	0.06	0.9	NS	NS

Table 6. Amplitudes of major tidal harmonics at the test site centered on 72°S, 172.5°E in the northwest Ross Sea (see Figure 21 for location). Column 2 lists component periods in hours. Columns 3 and 4 give amplitudes for sea surface elevation and barotropic cross-slope tidal current, respectively, from the RossTIM barotropic tidal inverse model. Column 5 lists amplitudes of variability in C_{ice} from the present study. Column 6 is the tidal analysis of a synthetic signal created using O1 and K1 signals only, processed, and analyzed as described in Section 5.2. NS, nonsignificant.

Aqua is in sun-synchronous orbit and passes over the equator at ∼13:30 local solar time [JAXA (*Japan Aerospace Exploration Agency*), 2006]. Locations closer to the poles are more frequently sampled by overlapping swaths. At 72° latitude, three to four swaths sample a specific location per day; however, the time separation of consecutive passes is not regular (Figure 22).

To determine whether tidal signals can be extracted from these irregularly sampled data, we first analyzed AMSR-E C_{ice} estimates from individual passes over a test site in the northwest Ross Sea continental slope where we expect the tidal signal in C_{ice} to be large [Erofeeva *et al.*, 2005; Padman *et al.*, 2009]. We extracted C_{ice} values from each satellite swath sampling a box of size 25 × 25 km centered at 72°S, 172.5°E (see Figure 21 for location). The box size is a compromise between the potentially small scales of variability of tidal divergence (set mostly by topography; see Padman and Kottmeier [2000]) and the need for sufficient spatial averaging of individual C_{ice} estimates from the swath data. The median number of C_{ice} estimates per box average for each swath is 6 to 8. The time difference of several seconds for individual swath data points over this small area was ignored in assigning a time t to each swath estimate of $C_{ice}(t)$.

We limited further analysis to the winter period April - November inclusive, when C_{ice} generally stayed between 0.5 and 1.0 (Figure 23a). The time series of spatially averaged

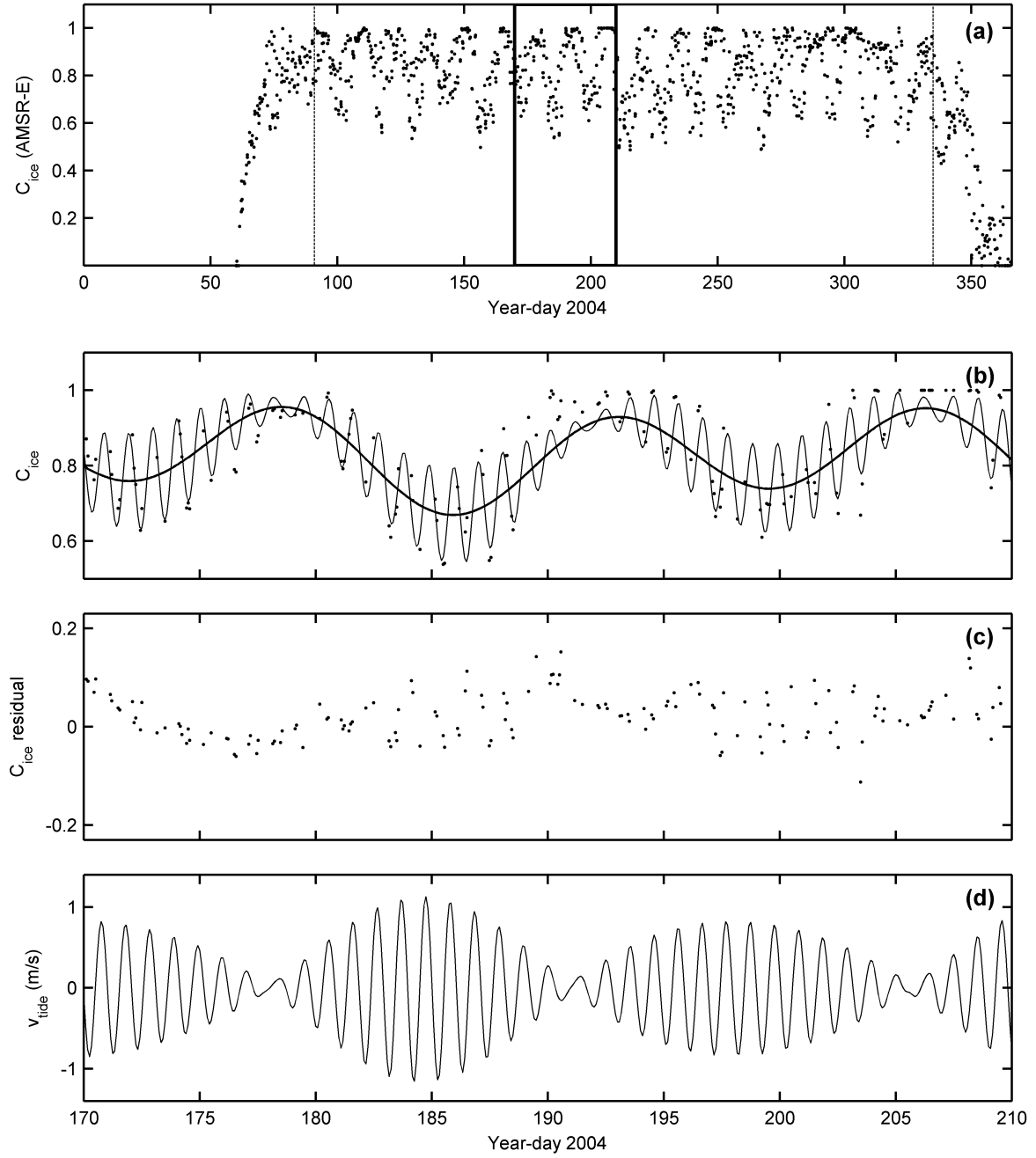


Figure 23. Sea ice concentration (C_{ice}) and tidal properties for year 2004 for a site in the northwest Ross Sea east of Cape Adare; see Figure 21 for location. (a) Measured values of $C_{ice}(t)$ for each swath, spatially averaged in a 25 x 25 km box. Vertical thin lines show period for which tidal analysis was performed with T_Tide (see Table 6). Vertical thick lines demark time interval shown in (b)-(d). (b) Values of C_{ice} for each swath (dots), tidal contribution based on T_Tide fit (continuous light line), and tidal contribution associated with long-period tides (continuous heavy line). (c) Residual C_{ice} anomaly after removal of tidal fit. (d) Cross-slope velocity v (m s⁻¹) evaluated with the RossTIM barotropic tidal inverse model [Erofeeva *et al.*, 2005].

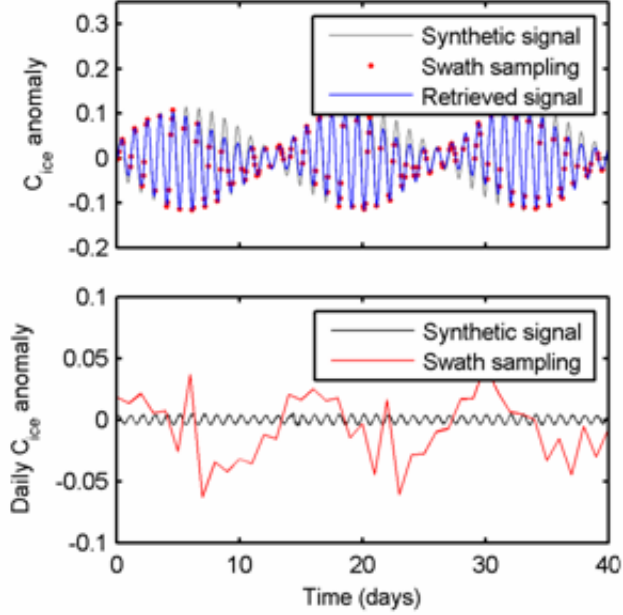


Figure 24. (top) Comparison of synthesized signal (O1+K1) with signal retrieved by our analysis procedure assuming data available at the actual times of C_{ice} acquisition (red dots) from the AMSR-E swath data set. (bottom) Comparison of daily averaged C_{ice} values for the same time series, computed as the 24-h running mean of the synthesized time series (black) and the daily average at the times of AMSR-E swath sampling (red).

$C_{ice}(t)$ values from each swath was interpolated to a regular two hour time interval using cubic splines. The resulting time series, denoted $C_{ice}^0(t)$, was analyzed with the Matlab toolbox, T_Tide [Pawlowicz *et al.*, 2002], to determine amplitude and phase coefficients for major tidal constituents. This package is based on the Foreman [1977] analysis code that extracts a best tidal fit using all tidal constituents that can be formally resolved with a given record length. Tide heights and currents in the northwest Ross Sea are dominated by diurnal tidal constituents O1 (period ~ 25.82 h) and K1 (~ 23.96 h), whereas semi-diurnal constituents are negligible [Erofeeva *et al.*, 2005; Whitworth and Orsi, 2006]. The tidal amplitude coefficients for C_{ice} (Table 6) generally show a similar pattern. However, the largest-amplitude tidal signal in C_{ice} is the long-period tide MF with period ~ 328 h (~ 13.66 days); this periodicity is the modulation period (spring/neap cycle) of the O1 and K1 fundamental tidal constituents.

5.2.1 ALIASING AND SAMPLING ISSUES

We tested our analysis procedure by generating a synthetic tidal signal as the sum of

two sine waves representing O1 and K1 with the same amplitudes given in column 5 of Table 6 and random phases. We then sampled this signal (see Figure 24) at the actual times of swath measurements of C_{ice} , interpolated the signal to a regular 2-h time base, and analyzed the signal with T-Tide, following the new analysis method described above. The analysis method returned the correct primary frequencies and no significant spurious signals, however, amplitudes for O1 and K1 were each reduced by $\sim 30\%$; compare columns 5 and 6 of Table 6. We attribute this reduction to cubic spline interpolation across the large daily gaps in the swath time series of C_{ice} . Despite the loss in signal amplitude, cubic spline interpolation provides the best quality retrieval of synthetic signals sampled at satellite pass times. Specifically, compared to other interpolation methods, cubic splines preserve the signal frequency over large data gaps without over-estimating the amplitude.

Note that the amplitude of the long-period MF constituent from the tidal analysis of the synthetic time series (~ 0.009) is small compared with the value of ~ 0.096 from our analysis of AMSR-E swath data. This observation indicates that the large MF signal in measured C_{ice} is not an artifact of the analysis procedure but represents some true geophysical variability over spring/neap cycles.

Sea-ice concentration products are routinely distributed as daily values that are derived as simple arithmetic means of all instantaneous C_{ice} measurements in a specific grid cell during 1 day. (For AMSR-E, a 12.5 x 12.5 km polar stereographic grid is used.) The irregular time sampling by swaths (Figure 22) suggests that this approach to constructing daily averages may alias diurnal tidal constituents, whose periods differ slightly from 1.0 solar day, to longer periods. To test whether this aliasing occurs in practice, we calculated daily arithmetic mean values of the synthetic O1 and K1 combined signal sampled at the satellite pass times. The irregular sampling for a specific location leads to a low frequency (14 day period) cycle in the daily mean values (Figure 24). The amplitude for this signal is much larger than the 24 hour running mean based on the synthesized tidal fit. Simple daily averaging of the irregularly sampled C_{ice} values from AMSR-E swaths can create a false fortnightly signal in places where the fundamental daily tides dominate. Here, this false signal is smaller than the real fortnightly signal in C_{ice} that we ascribe to nonlinear interactions between mean flow and tides.

We also applied the new analysis method to a simpler synthetic signal composed of a single sine wave with period 24.89 hours equal to the average of O1 and K1 periods. In this case, the daily averages show a period of 27.4 days with an amplitude about 60% of the original sine wave, which is entirely a product of the irregular sampling scheme. The ~ 14 and ~ 27

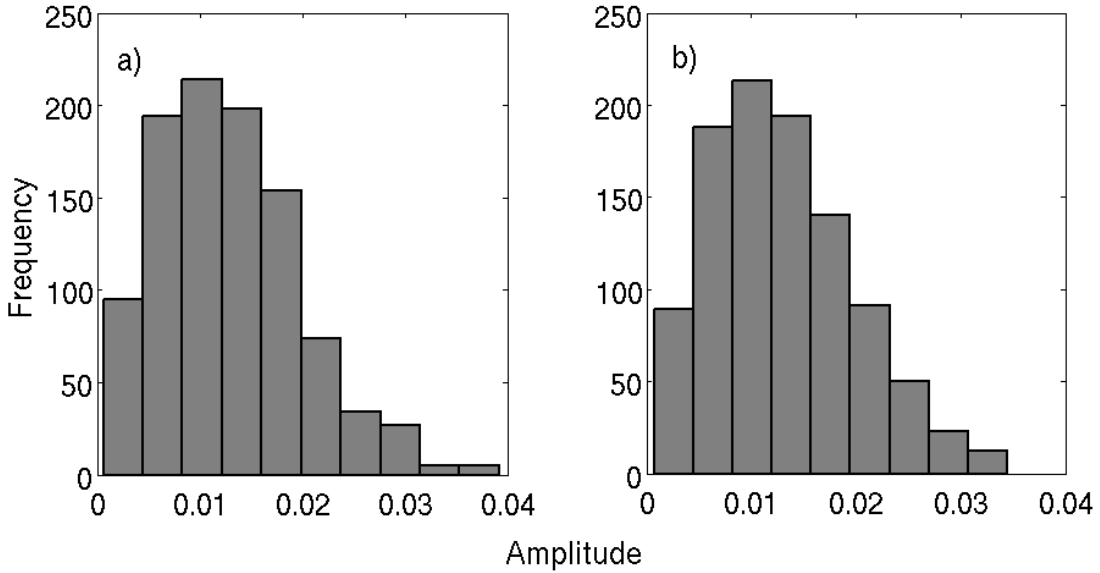


Figure 25. Frequency distribution of amplitudes of (a) O1 and (b) K1 from 1000 Monte Carlo type simulations of noise-only time series that were randomly sampled from a normal distribution with a standard deviation of 0.1.

day periods from aliased fundamental tides may be misinterpreted as monthly variability in C_{ice} . These results can be generalized to any sun-synchronous satellite observing phenomena with near-daily periodicity at high latitudes.

5.2.2 ERROR ANALYSIS

To assess the size of the error in the amplitudes of O1 and K1 in C_{ice} , we used a Monte Carlo type approach. Comiso [2009] estimates the error in AMSR-E data to be 4-10% in dry winter conditions. We generated a normal distribution with a standard deviation of 0.1 and mean of 0, and randomly sampled it at satellite pass times to create a signal of pure noise. We interpolated this signal to a regular two hour time base and analyzed the signal with T_Tide, following the new analysis method. O1 and K1 amplitudes were recorded for one thousand different sets of random noise and the resulting distributions are displayed in Figure 25. The standard deviation, and thus the error estimate, for both is 0.007.

5.2.3 REGIONAL OCEAN MODEL

The Ross Sea model used in this study is built using ROMS, with a set-up similar to that described in Section 2.3. The major difference is that simulations are run from September

15, 2003 through September 15, 2005, with forcing adjusted to match the time period. High frequency output is recorded at four hour intervals over the second winter, from April 2005 until September 2005 in order to resolve tidal signals. Following the convention established in Chapter 2, the simulation at 5 km resolution without tidal forcing is referred to as simulation **5**; with tidal forcing it is **5T**.

We use T-Tide directly to analyze model output, as the data is already evenly distributed in time and space. To compare with AMSR-E results, simulation variables are averaged within the box along the northwest shelf break, as shown in Figure 21.

5.3 RESULTS AND DISCUSSION

5.3.1 AMSR-E OBSERVATIONS

The time series of area-averaged, single-swath values of $C_{ice}(t)$ for the 25 x 25 km box centered on 72°S, 172.5°E shows values ranging from ~0.5 to 1.0 with a mean of 0.84 for April November inclusive, 2004 (Figure 23a). The T-Tide analysis applied to the interpolated time series $C_{ice}^0(t)$ (Table 6) shows significant O1 and K1 signals with C_{ice} amplitude coefficients of 0.070 ± 0.007 and 0.046 ± 0.007 , respectively, and a large MF (period ~13.7 days) tide with amplitude ~0.096.

The MF signal represents the observed reduction from high daily-averaged ice cover ($C_{ice} > 0.9$) at neap tides to typical values of ~0.7 at spring tides (Figure 23b). The large MF signal is not the result of aliasing of the O1 + K1 signal by irregular temporal sampling; compare columns 5 and 6 of Table 6.

The amplitude of the residual signal in C_{ice} , after removing the fitted tidal variability including long-period tides, is smaller than the tidal component (compare Figure 23 c and b). That is, tides explain most variability of C_{ice} at this location during winter.

To place the tidal signals in C_{ice} in the context of ocean tidal state, we use the Ross Sea Tidal Inverse Model (RossTIM) [Erofeeva *et al.*, 2005] to estimate the depth averaged cross-slope tidal velocity (Figure 23d). The RossTIM model assimilates velocities from moorings and ship-based acoustic Doppler current profiles from cruises near the northwest Ross Sea shelf break and so is the best available model for predictions of barotropic tidal currents in this region. The spring/neap cycle of $C_{ice}^0(t)$ (Figure 23b) is approximately out of phase with the spring/neap cycle in modeled cross-slope ocean tidal velocity; the lowest daily-averaged values of C_{ice} occur about 1 day after maximum spring tidal currents.

We expect that the major effect of ocean tides on C_{ice} at the fundamental diurnal tidal

periods is caused by tidal divergence [Padman and Kottmeier, 2000]. Tides in the northwest Ross Sea also cause warmer offshore water to flood onto the outer continental shelf [Padman *et al.*, 2009]; however, we do not expect these warmer waters to significantly change ice concentration by melting because individual ice floes are advected quite rapidly through the region where tidal advective effects are significant (see Comiso *et al.* [2011], for maps of measured ice velocity). Thus, for the remainder of this article, we focus on changes in C_{ice} associated with predicted periodically divergent tidal stresses.

By applying the above analysis of AMSR-E swath C_{ice} data to 25 x 25 km boxes covering the entire Ross Sea, we have developed maps of amplitude and phase coefficients for O1 and K1 constituents (Figure 26). Boxes with a signal-to-noise ratio (SNR) < 3, based on T-Tide output, have been hidden. Amplitudes for both O1 and K1 sometimes exceed 0.05 over the continental slope in the northwest Ross Sea, and significant values (SNR > 3) are found along much of the continental slope and over Iselin Bank (see Figure 21 for location). Phase maps (Figure 26, top) show westward propagation of C_{ice} anomalies along the continental slope, consistent with diurnal tidal currents being primarily associated with small-scale topographic vorticity waves trapped to the slope [Padman and Kottmeier, 2000; Erofeeva *et al.*, 2005].

We used the RossTIM model and the same averaging scale (25 x 25 km) applied to swath estimates of C_{ice} to estimate the horizontal divergence of ocean tidal currents ($\nabla_h \cdot \mathbf{u}_{ocean}$) for each of O1 and K1. The standard deviation of lateral divergence, $\sigma(\nabla_h \cdot \mathbf{u}_{ocean})$, can then be converted to the amplitude coefficient (A) of the open-water fraction for a specific tidal constituent, assuming free drift of sea ice, by

$$A = \frac{\sigma(\nabla_h \cdot \mathbf{u}_{ocean} T_{tide})}{\sqrt{2}\pi} \quad (16)$$

where T_{tide} is the period of the constituent. Peak values of $\sigma(\nabla_h \cdot \mathbf{u}_{ocean})$ are $\sim 10^{-5} \text{ s}^{-1}$, implying $A = 0.2$ for a single constituent of the diurnal tide. However, the values of A based on RossTIM are typically about twice as large as the values derived from our analyses of AMSR-E swath data (compare Figure 26, middle and bottom). The RossTIM model does not include the long-period MF tidal constituent; however, analyses of predicted values of $\sigma(\nabla_h \cdot \mathbf{u}_{ocean})$ for MF in other tide models suggest that the divergence for this constituent is much too small to explain the observed MF signal in $C_{ice}(t)$, although T_{tide} is large (~ 14 days).

Because RossTIM is based on assimilation of tidal current data [Erofeeva *et al.*, 2005], we expect that it is a reasonable representation of lateral divergence of barotropic tidal

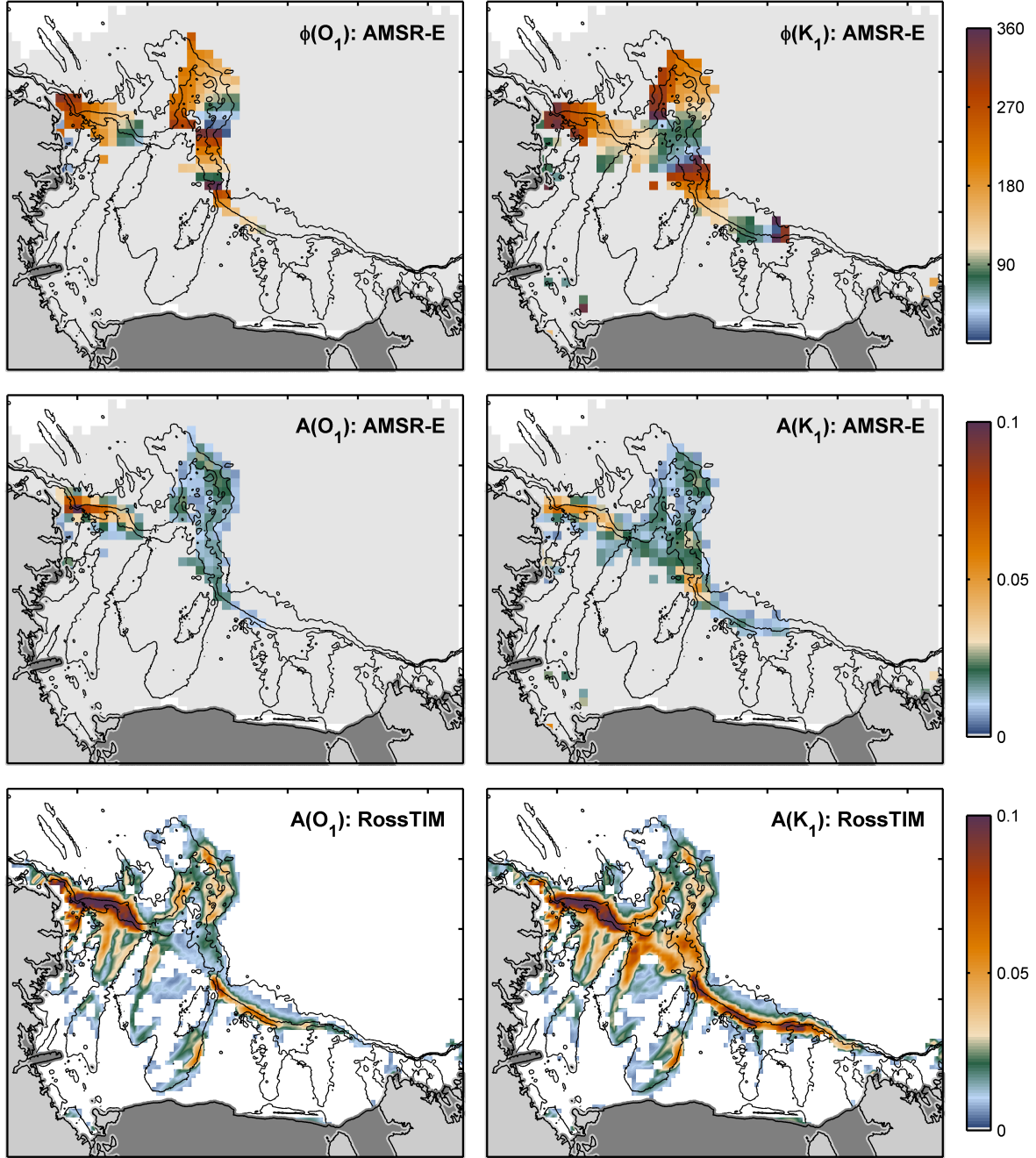


Figure 26. (left, top and middle) Phase and amplitude of C_{ice} variability for the O1 tidal constituent from T_Tide analysis of AMSR-E swath data in 25×25 km boxes. Boxes with a SNR<3 (determined by T_Tide) are not plotted. Amplitude has been scaled by 1.2 to account for signal reduction associated with interpolation of the irregular time series of swath data (see Table 6). (left, bottom) Amplitude of C_{ice} variability based on the barotropic inverse tide model RossTIM, using 25×25 km boxes to calculate horizontal divergence of O1 tidal currents ($\Delta_h \dot{u}_{ocean}$), and assuming free drift of sea-ice. Values < 0.005 are not plotted. (right) Same as left, but for K1 tidal constituent. In all panels, black contours are 500, 1000, and 2000 m isobaths.

Constituent	Period (h)	C_{ice}	Ice-ocean mass flux (cm day $^{-1}$)	Surface heat flux (Watts m $^{-2}$)
Simulation 5T				
O1	25.83	0.112	0.517	62.16
K1	23.96	0.060	0.255	33.15
Simulation 5				
O1	25.83	NS	NS	NS
K1	23.96	NS	NS	1.309

Table 7. Simulation-derived amplitudes of tidal harmonics O1 and K1 at the test site centered on 72°S, 172.5°E in the northwest Ross Sea (see Figure 21 for location). Column 2 lists component periods in hours. Columns 3-5 list amplitudes of variability in sea ice concentration, ice-ocean mass flux, and surface heat flux from T-Tide analysis. NS is not significant.

ocean currents at the fundamental tidal periods of ~ 1 and ~ 0.5 day. Thus, we interpret the discrepancies between measured and modeled values of A for O1, K1, and MF as indicating weaknesses in the free-drift assumption used to equate $\nabla \cdot \mathbf{u}_{ice}$ to $\nabla_h \cdot \mathbf{u}_{ocean}$ and/or the presence of baroclinic tidal signals that reduce the near-surface tidal divergence relative to the barotropic (depth-averaged) value. Identifying these processes is beyond the scope of the present study; however, the existence of these discrepancies suggests that tidal analyses of C_{ice} measurements from AMSR-E swath data may be used to diagnose sea ice mechanical properties and ice/ocean coupling.

5.3.2 ROSS SEA MODEL

The timeseries of C_{ice} from simulation **5T** (Figure 27a) resembles that derived from AMSR-E observations (Figure 23a), with variations in C_{ice} over the winter months between 0.5 and 1.0, although there appears to be more high frequency variability at the diurnal scale. The amplitude of O1 and K1 in C_{ice} is higher than that derived from AMSR-E data by 30 to 60% (compare Tables 6 and 7), although this is expected as the cubic spline interpolation of satellite data diminishes the total amplitude of the signal. C_{ice} taken from simulation **5** shows, as expected, no significant variability at tidal frequencies.

Using simulation results, we can further investigate the potential effects of tidal variability on variables related to C_{ice} . As tidal divergence causes the sea ice to open, the heat flux from the ocean to the atmosphere increases. Comparing simulations **5** and **5T**, we see a large increase in surface heat flux to the atmosphere in **5T** at timescales consistent with

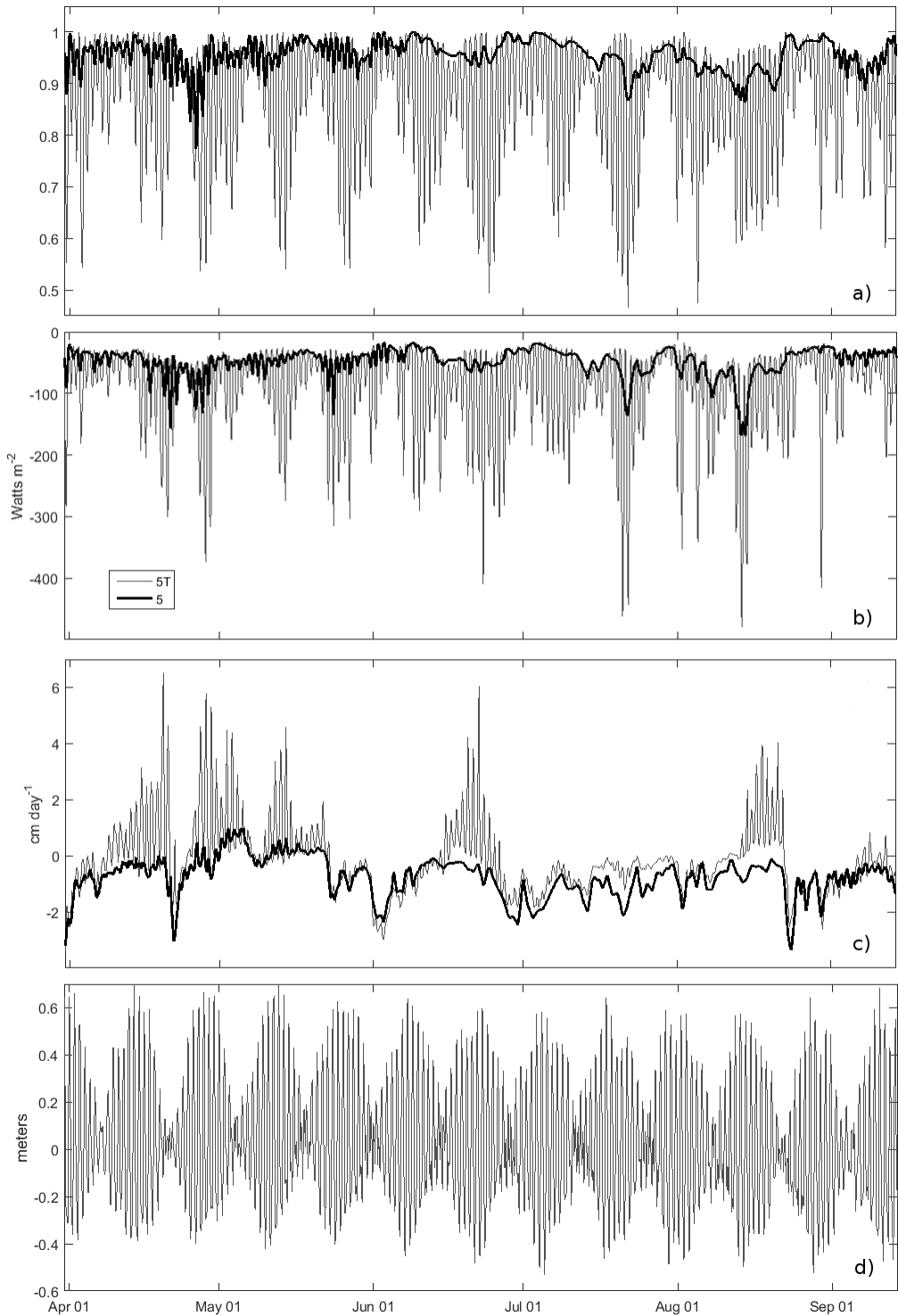


Figure 27. Time series from simulations, averaged over the box shown in Figure 21. a) C_{ice} ; b) Surface heat flux (W m^{-2}), negative is out of the ocean; c) Ice-ocean mass flux (cm day^{-1}), positive values indicate sea ice formation; d) Sea surface height (meters) from **5T**. For a,b,c) bold line is from simulation **5**, light line is simulation **5T**.

tidal variability (Figure 27b; Table 7). Maximum heat fluxes at spring tide can reach 300 W m^{-2} , potentially affecting local weather. During several spring tides, this loss of oceanic heat triggers sea ice formation (Figure 27c). This implies that, in this section of the Ross Sea, tidal divergence is a mechanism that forms temporary polynyas which have the capability to produce sea ice. These tidal polynyas open up what would otherwise be a sea ice covered area and allow exchange between the ocean and the atmosphere during austral winter.

5.4 CONCLUSION

At sufficiently high latitudes, the tidal contribution to sea-ice concentration variability can be evaluated from analyses of individual swaths of AMSR-E satellite passive microwave data. For a typical latitude of ice-covered polar seas, $\sim 72^\circ$, we obtain approximately three to four passes per day, which is sufficient to quantify diurnal tidal variability. For higher-latitude locations such as the southern Ross and Weddell seas, and the Arctic Ocean, swath data are acquired more frequently. However, many of these locations are dominated by semidiurnal (period $\sim 1/2$ day) rather than diurnal tides, thus requiring more frequent passes to adequately sample the fundamental tides.

For our study region in the northwest Ross Sea, sea ice response to ocean tidal currents causes C_{ice} to vary in winter (April to November inclusive) by up to 0.2 around a mean value of ~ 0.8 . Variability of this magnitude could have a significant impact on the average heat exchange between the atmosphere and ocean and net sea ice production, much like a small polynya. Results from a regional ocean model support this hypothesis, showing both significant heat fluxes from the ocean to the atmosphere that trigger several sea ice formation events during the austral winter.

We hypothesize that the time-averaged value of C_{ice} over the northwest Ross Sea continental slope is itself lower than it would be in the absence of tides. Our conceptual model is that, in winter, sea ice is advected from the south at $\sim 0.1 \text{ m s}^{-1}$ [Comiso *et al.*, 2011] as almost solid ice pack (Figure 21). As the pack ice transits the shelf break and continental slope, it is relatively unaffected if it crosses during neap tides but is periodically forced open by tidal divergence during spring tides (Figure 23). This intermittent creation of open water (i.e., leads) in an ice pack that would otherwise have $C_{ice} = 1$ implies dynamic thickening of ice floes by rafting and by ridge building at floe margins as new ice formed in the transient leads is compressed in each subsequent convergent phase.

Ice resistance to deformation explains the reduction of O1 and K1 tidal components of

$C_{ice}(t)$ relative to the values estimated from a barotropic inverse tidal model and the free-drift approximation. The strong spring/neap cycle of C_{ice} (Figure 23b) is consistent with coupling between mean advection and the spatially limited region of strong tidal currents. It is also possible that baroclinicity of the tidal currents leads to a reduction in surface values of $\nabla \cdot \mathbf{u}_{ocean}$ relative to the modeled barotropic (depth-averaged) values, but we have seen no evidence for significant baroclinic tides in the weakly stratified Ross Sea.

We have also demonstrated that, because of the irregular time sampling by satellite swaths, simple daily averages of C_{ice} (as typically provided to users) can alias diurnal tides to lower frequencies (~ 1 and ~ 2 cycles per month), where the signal may be confused with wind-forced and other low frequency variability in C_{ice} . An improved approach to daily averaging is to fit tidal harmonics to estimates of C_{ice} at times of individual swaths and then calculate the average of the fitted time series.

The AMSR-E single-swath data set and the methodology described above are best suited to high-latitude regions where ocean tidal divergence is strong and other causes of C_{ice} variability at high frequencies are relatively weak. Such regions include the ice-shelf fronts and shelf breaks of the Ross and Weddell seas in Antarctica and the eastern Arctic Ocean. Further analyses of the AMSR-E ice concentration record may provide valuable information not only on the sea ice cover but also on the state of the underlying ocean and our ability to model it.

CHAPTER 6

IRON TRANSPORT PATHWAYS

6.1 INTRODUCTION

Primary production in the Ross Sea is limited for most of the year by light availability. The high latitude location means that there is very little solar radiation in winter, and even when the amount of light increases, it is obstructed by a thick cover of sea ice on the ocean surface. Only in a few months in spring and summer, when the solar radiation is high and the sea ice melts, do the phytoplankton bloom. However, the bloom quickly becomes nutrient limited and cannot be sustained through the entire summer. Specifically, it is the micronutrient, dissolved iron (dFe), that limits phytoplankton growth. DFe is necessary only in very small quantities, but when there is sufficient supply of major nutrients such as nitrogen and phosphorus, as well as ample solar radiation, dFe acts as the limiter to primary production.

The dependence of entire ecosystems, such as the one in the Ross Sea, on a metal found only in trace amounts throughout the ocean is a relatively recent discovery. Special oceanographic equipment and procedures that are “trace metal clean” are needed to be able to measure the amount of dFe in seawater without contamination. One of the main objectives of the PRISM-RS project (Section 2.2.1) was to measure the amount of dFe in seawater throughout the Ross Sea to obtain information on how it varies spatially and with depth. Variations with depth are of particular interest, as the sediments are a potential source of dFe and concentrations of dFe deep in the water column provide an estimate of how much is mixed upwards to the surface during times of deep winter mixing.

In Chapter 3, the PRISM-RS data was used as a validation tool for the model. Here, dFe measurements from PRISM-RS observations and other sources are used to estimate the amount of dFe from each potential source. Then, the simulations track the dispersion of dFe throughout the model domain, providing information on what is potentially happening at unobserved locations and times. Specifically, the focus is on tides and mesoscale eddies, and the contribution from each of these processes to the distribution of dFe in the surface ocean during spring and summer. This illustrates not only the potential transport pathways of dFe

from source locations to the surface ocean, but also the variability of supply when tides and eddies are considered.

For the purposes of simulation, the potential sources of dFe in the Ross Sea can be grouped into four main categories, each one corresponding with a passive tracer dye in the model. Surface input of dFe over the main part of the Ross Sea comes from sea ice melt and iron deposited from atmospheric dust, which lands on the sea ice most of the year. Glacial melt sources of dFe have several components, including the main Ross Ice Shelf, various smaller ice shelves and glaciers, and subglacial streams. The various ice shelves and glaciers contain similar amounts of iron, but the subglacial streams running under the ice sheet and connecting to the ocean at the grounding line are thought to have much higher concentrations of dFe. However, as these streams are essentially point sources far away from the open continental shelf, with little known about their total input, quantity, and locations, it is not feasible to model them separately. Circumpolar Deep Water (CDW) is a third source: off-shelf CDW is relatively high in dFe compared to the depleted on-shelf waters in the Ross Sea, and intrusions of this water mass increases the amount of dFe on-shelf. The final source is from deep on-shelf waters and includes dFe directly effluxed from the sediments as well as dFe that is remineralized at depth, i.e., as organic matter decomposes, the dFe it took in while alive is released as it sinks. By estimating the amount of dFe available immediately above the seafloor, these two processes can be grouped into one source without specifying the relative contribution from each.

This chapter is the culmination of the rest of the research presented in this thesis. The central question - what are the transport pathways for dFe in the Ross Sea and how are they affected by tides and mesoscale eddies - is addressed using the model developed in Chapter 2 and validated in Chapter 3, with an understanding of how mesoscale eddies are represented at different horizontal resolutions (Chapter 4). The passive tracer dyes are translated from arbitrary dye units to dFe concentrations, and changes in dFe supply to the surface mixed layer (SML), both temporally and spatially, are compared between simulations.

6.2 METHODS

Estimates of the supply of dFe to the surface ocean are dependent on a series of calculations using observations and simulations; both are described in Chapter 2. First, observations are used to determine the concentration of dFe in each of the four sources represented by a tracer dye. Then, the ocean surface is defined by calculating the mixed layer depth (MLD) and specifying the surface as the SML above that. Model values of MLD are compared with

climatological values and estimates from the PRISM-RS observations. Then, using tracer dye concentrations within the SML, the amount of dFe supplied from each source is calculated and compared between simulations using the Simulation Significance Criterion (SSC) introduced in Section 2.5.2.

6.2.1 PASSIVE TRACER DYES

Each of the four sources of dFe in the model is tracked using a passive tracer dye, which are detailed in Section 2.5.1, and used in Chapter 3. Three of these dyes, representing CDW (dye_{CDW}), sea ice melt (dye_{SIM}), and glacial melt (dye_{GM}), have also been used in previous studies [Dinniman *et al.*, 2011; McGillicuddy *et al.*, 2015]. In brief, dye_{CDW} is initialized in off-shelf waters that meet the criterion for CDW (temperature greater than 0 °C), and is diffused and mixed onto the continental shelf by physical processes. Dye_{SIM} is input into the surface layer of the model as a function of positive sea ice melt (ice formation does not remove dye). Similarly, dye_{GM} is injected into the surface layer under the ice shelves as a function of positive glacial melt. Calculations of dye end-member concentrations of dissolved iron and associated errors from observations are given in detail in *McGillicuddy et al.* [2015].

These three dyes are initialized at the beginning of the simulations and allowed to disperse throughout the model domain for the full year and a half. This allows dye_{CDW} and dye_{GM} to travel from their source locations off-shelf and under the ice shelf to the continental shelf before being mixed upwards over the course of the last simulation year. The concentrations of dye_{CDW} and dye_{GM} in the surface mixed layer at the end of the first six months are less than 1%, and have no impact on the final values. Dye_{SIM} does have a significant concentration at the end of the first six months, but disperses to extremely low concentrations over the course of the winter, and is likewise negligible.

The fourth dye (dye_{bdFe}) was added as a proxy for benthic iron sources, including sediment efflux and benthic remineralization. Observations from the PRISM-RS cruise (Section 2.2.1) of the distribution of dissolved iron near the sea floor were used to set the parameters for dye_{bdFe} . These observations indicate that only locations with bottom depths below 400 meters have enhanced dFe concentrations near the bottom, most likely due to the presence of a benthic nepheloid layer not observed in shallower regions [Marsay *et al.*, 2014]. Following Marsay *et al.* [2014], all measurements of dFe concentration below 200 meters depth, where the bottom depth was at least 400 meters deep, were fit as a function of height

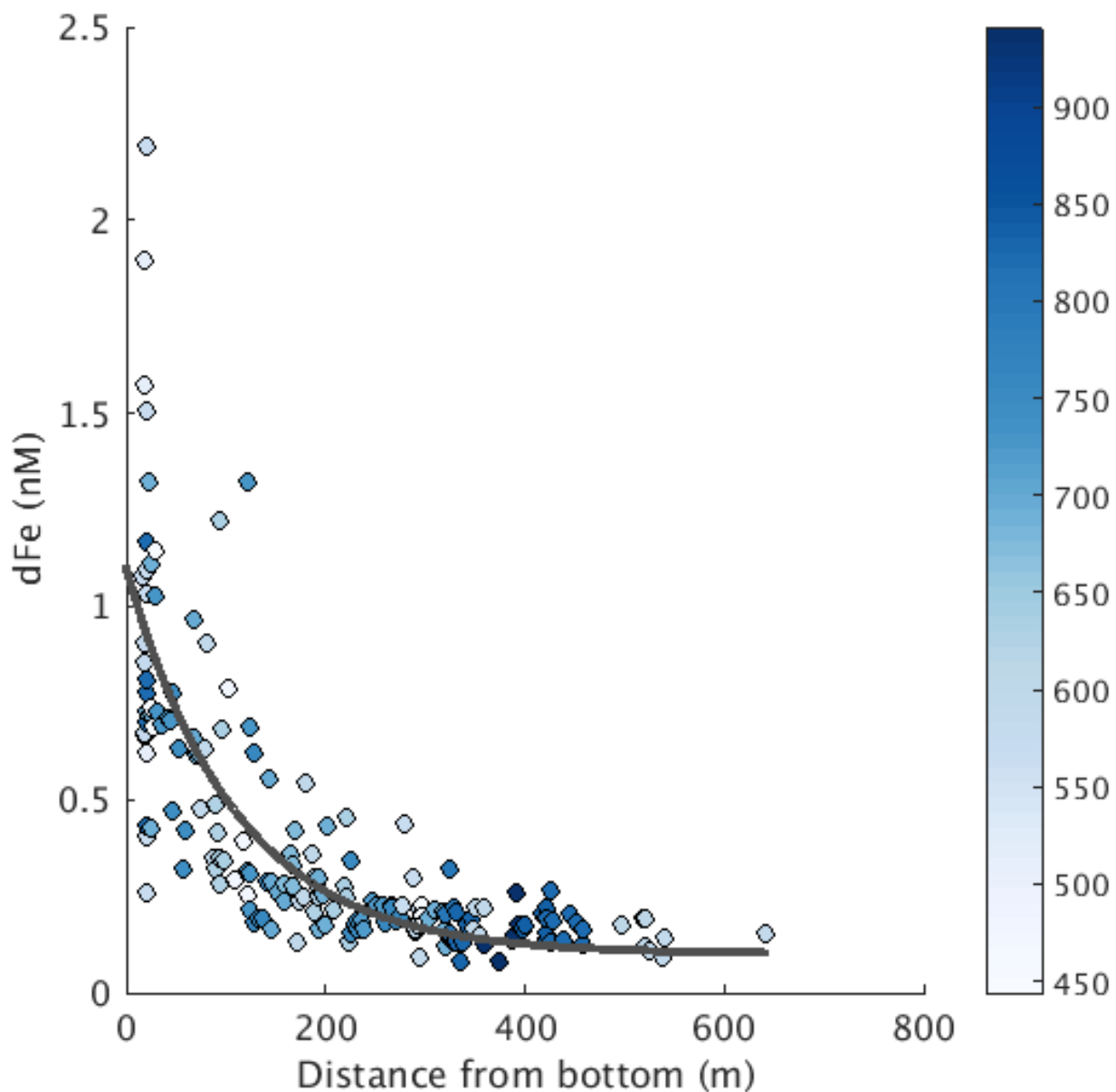


Figure 28. DFe measurements below 200 m from casts where bottom depth was greater than 400 m, given as a function of distance from the seafloor. Color bar is total water column depth in meters. Black line is exponential fit from Equation 17. Adapted from Marsay *et al.* [2014].

Dye	dFe End Member (nM)	Source
dye_{CDW}	0.27 ± 0.05	<i>Sedwick et al. [2011]; McGillicuddy et al. [2015]</i>
dye_{SIM}	10.0 ± 5.0	<i>McGillicuddy et al. [2015]; Lannuzel et al. [2010]</i>
dye_{GM}	29.0 ± 21.0	<i>McGillicuddy et al. [2015]</i>
dye_{bdFe}	1.04 ± 0.22	<i>Marsay et al. [2014]</i>

Table 8. End member concentrations for model passive tracer dyes.

above bottom, z , with the suggested exponential:

$$dFe = 0.1 \text{ nM} + Ae^{Bz} \quad (17)$$

Applying the fit to all dFe data (Figure 28), yields fit parameters $A = 0.9973$ and $B = -0.00908$, with 95% confidence levels of [0.8837, 1.111] and [-0.01083, -0.007334], respectively. This fit is used to calculate the estimated concentration of dFe in the bottom model layer at all on-shelf grid points inshore of the 700 m isobath and deeper than 400 m. The average height above bottom of this layer is 6.57 m with a range of 4.79 m to 14.68 m, and the expected dFe concentration at 6.57 m above the seafloor is $1.04 \text{ nM} \pm 0.22 \text{ nM}$, which sets the end member for dye_{bdFe} .

In the model, dye_{bdFe} is initialized at all grid points inshore of the 700 m isobath, at depths greater than 400 m. Locations under the ice shelf are excluded, as there is no data to properly represent benthic sources there. The dye is held at a constant value in the bottom layer, allowing transport to be determined by advection, mixing, and turbulent diffusion. It is essentially an infinite source that operates under the assumption that flux into the benthic layer from sediments or remineralization is in steady state with flux out of the benthic layer. As the model represents only physical processes, and not any biological uptake parameters, dye_{bdFe} is not initialized until the end of the first simulation summer (i.e., March 1, 2011). The dye that reaches the surface by the end of the simulation represents the input over the course of one year, and thus represents a reasonable estimate of what is available for biological uptake during the growing season.

6.2.2 SIMULATION SIGNIFICANCE CRITERION

When comparing simulations, the SSC defined in Section 2.5.2 (Equation 2) is used as a threshold for statistical significance. However, the passive tracer dyes accumulate during a simulation from continual supply with export through the open boundaries as the only sink.

This accumulation lessens the physical meaning of the dyes over multiple years of simulation, but it does not affect the relative magnitude of the sub-annual variability for each, a key part of calculating the SSC.

For example, dye_{GM} in the surface mixed layer accumulates throughout simulation **S5**, as the water fills up with dye over the first four years and then stabilizes with a seasonal cycle (Figure 29). Despite the dye accumulation, the relative magnitude of the sub-annual variability stays consistent over time. This holds true for all four dyes, as well as their sum.

6.2.3 MIXED LAYER DEPTH CALCULATIONS

The literature lists many ways to calculate MLD, from exceeding a threshold or gradient condition to more involved methods [Holte and Talley, 2009]. Here MLD is calculated following *de Boyer Montégut et al.* [2004], by applying a threshold method using temperature and density, which has been demonstrated to work well in the Southern Ocean [Dong et al., 2008]. For data from the PRISM-RS cruise, the reference depth is set to 10 m, to avoid ephemeral surface effects. For simulation output, the reference level is set to the top model layer (thickness of 1 m in shallow areas, and up to 15 m over abyssal depths). Using the second model layer instead has little to no effect on the end result.

The MLD is then defined as the shallowest depth below the reference depth that meets the criterion $|\Delta T| \geq 0.2^\circ\text{C}$ or $\Delta\rho \geq 0.03\text{ kgm}^{-3}$, where T is potential temperature, and ρ is potential density. For the most part, MLD in the Ross Sea is controlled by salinity gradients, although some locations near the ice shelf front have a shallower MLD based on the temperature criteria. There are also instances where deep winter mixing reaches the seafloor, and MLD is limited by that depth.

6.3 RESULTS

6.3.1 BENTHIC DYE PATHWAYS

Simulation **5** is used as the base case, and analyzed to determine the pathways of dye_{bdFe} . Starting in March 2011 in the bottom model layer, dye_{bdFe} is initialized to 100 dye units inshore of the 700 m isobath only where the water column depth is greater than 400 m (locations with 100 in the first panel of Fig. 30). Dye_{bdFe} is zero elsewhere and at all locations under the ice shelf. The dye flows off the western side of the continental shelf break, approximating the flow of dense High Salinity Shelf Water (HSSW) that sinks and

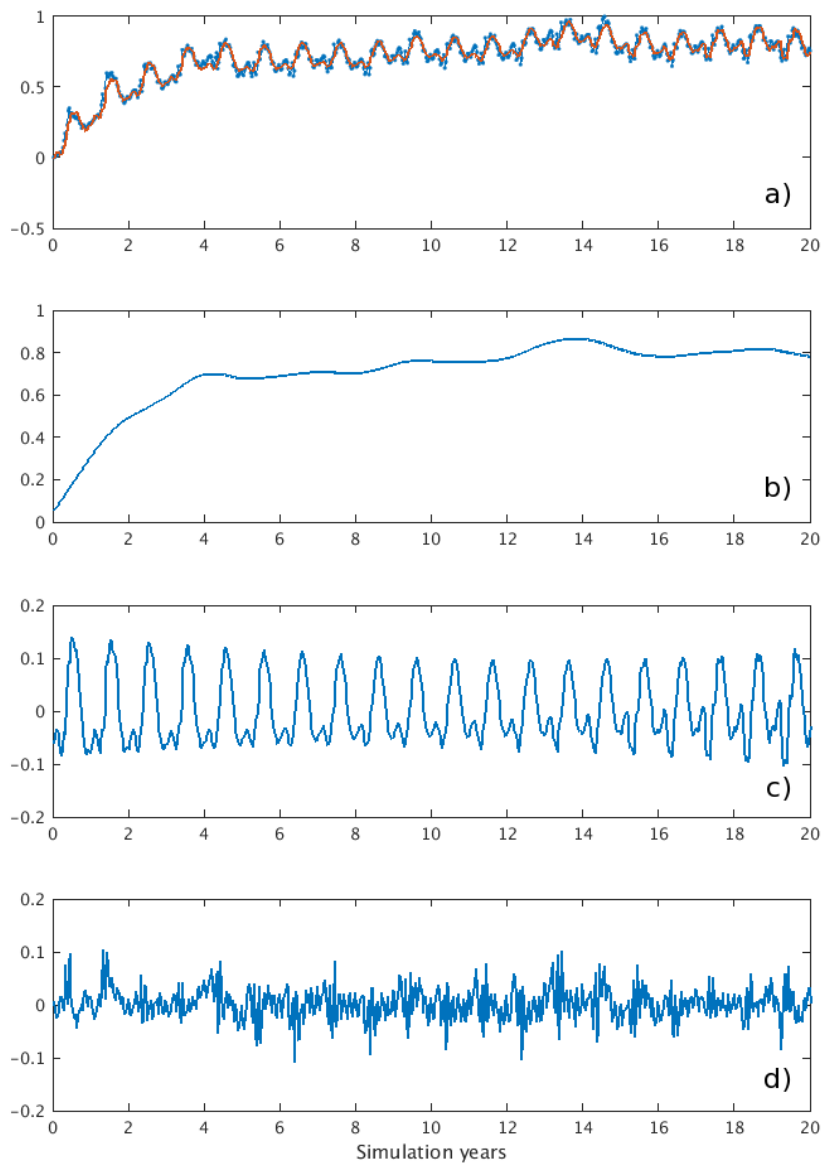


Figure 29. STL (Seasonal Trend using Loess) [Cleveland *et al.*, 1990] decomposition of dye_{GM} from simulation **S5** with annually repeating forcing. a) Dots are original timeseries normalized by the maximum value, solid line is the fit (trend plus seasonal cycle). b) Non-linear trend. c) Seasonal cycle. d) Sub-annual variability.

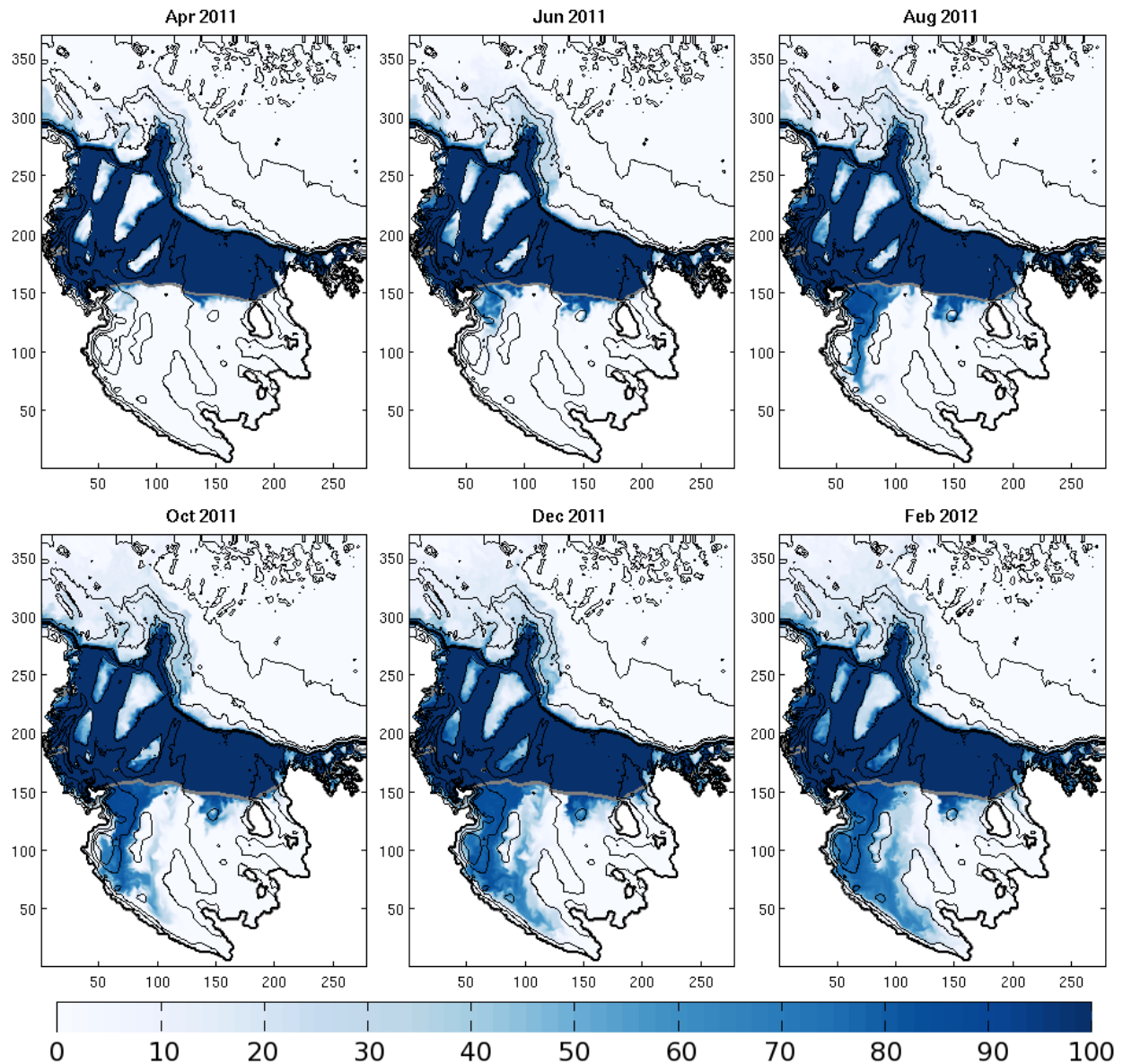


Figure 30. Monthly snapshots of dye_{bdFe} in the bottom model layer for the last year of simulation 5. Color bar is in dye units, where the dye was initialized at 100. Black lines are bathymetry contours, gray line is the ice shelf front. X/Y axes indicate simulation grid points.

entrains ambient water to form Antarctic Bottom Water (AABW). Dye concentrations off-shelf here range from 20-30, indicating that the bottom water from the continental shelf forms 20-30% of what becomes AABW derived from the Ross Sea. This matches estimates of the benthic layer containing 25% HSSW off Cape Adare [Gordon *et al.*, 2009], or 30% at 1500 m depth on the western continental slope.

The dye intrudes on the western side of the Ross Ice Shelf and continues towards the grounding line, illuminating the pathway of HSSW into the ice shelf cavity which impacts basal melting (Figure 30). There is a small intrusion on the east side that develops quickly, but does not advance very far under the ice shelf, resulting in constant dye values after mid-winter.

In the center of the continental shelf, benthic waters from deeper locations are mixed over the banks during the course of the year. In particular, more than 50% of the bottom water on Mawson and Ross banks is from deeper areas of the continental shelf, while Pennell Bank has significantly less. The depths of these banks are similar, but Pennell is the widest and flattest of the three.

The concentration of dye during the austral summer months for all simulations is captured by calculating a December-January-February (DJF) average (Figure 31). Increased horizontal resolution in simulations **1** and **1T** shows less dye over Crary Bank (south of Mawson), indicating steeper bathymetry at higher resolution redirects benthic flows around the bank, rather than over it. There is also less dye on the far eastern side of the continental shelf, and under the middle of the ice shelf. However, the amount of dye that leaves the continental shelf in AABW increases.

When tidal forcing is added in simulations **5T** and **1T**, the amount of dye over Mawson and Pennell banks increases. A probable mechanism for this increase in dye_{bdFe} is the increase of onshore velocities with tides along the western side of the banks near the shelf break at depth. Increased energy and mixing sloshes dye from depth up onto the banks from the western side. The same effect is not seen at Ross and Crary banks, as they are too far removed from the shelf break, where tides are weaker. Under the ice shelf, the western side has more dye, indicating an increased flushing of the ice shelf cavity with tides, and the eastern side of the ice shelf front also shows more dye intruding.

Surface (i.e., top model layer - several hundred meters below sea level under the ice shelf) dye_{bdFe} indicates where upwelling and significant vertical mixing occurs (Figure 32). Two months after the dye_{bdFe} is initialized, it begins to reach the surface along the front of the Ross Ice Shelf, and near Terra Nova Bay, both persistent polynya locations with strong

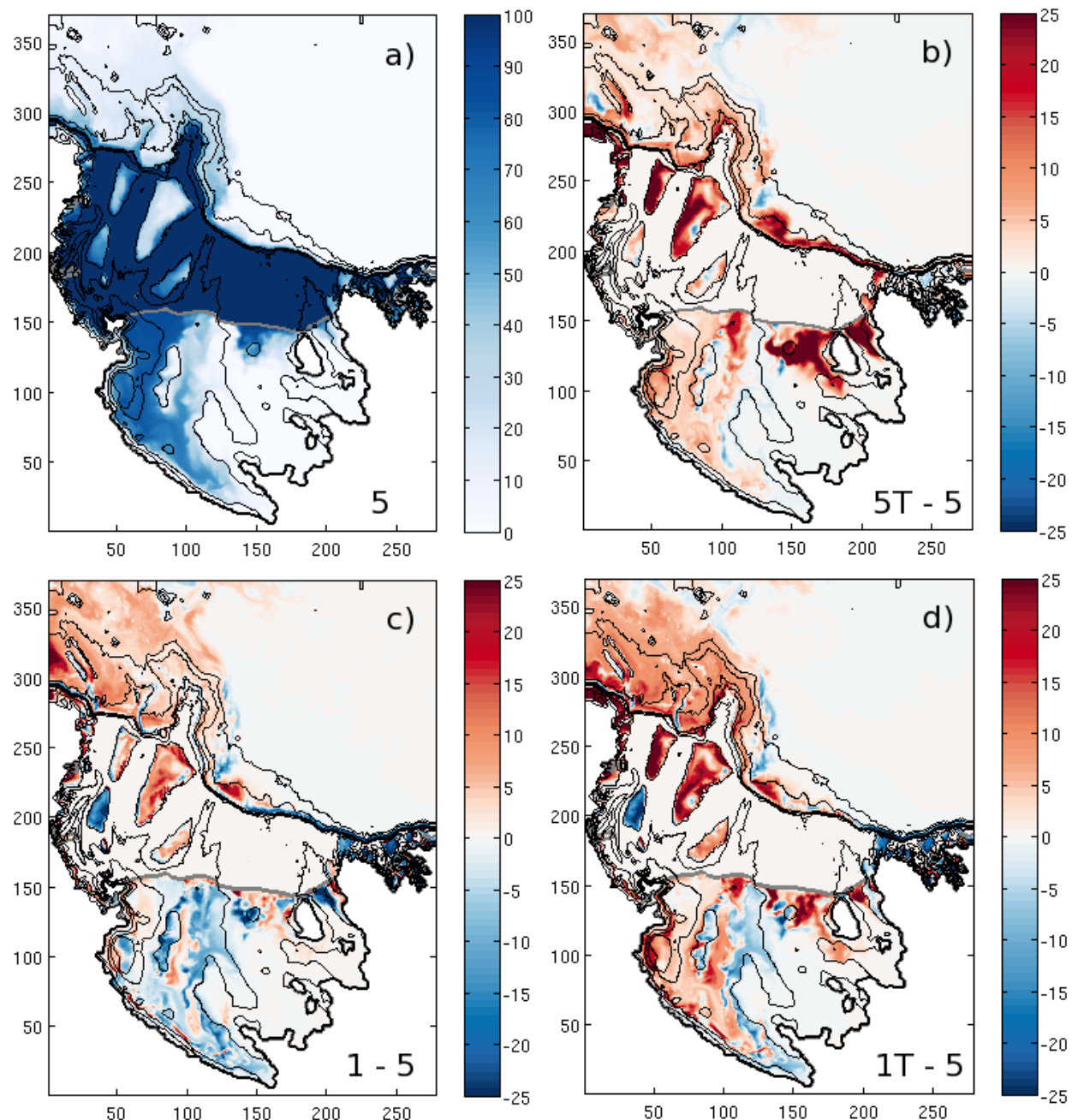


Figure 31. Average amount (DJF) of benthic dye in bottom model layer. a) Results from simulation 5; b,c,d) Difference between simulation 5 and 5T, 1, 1T, respectively. Positive values indicate more dye in that simulation, negative values indicate less. Colorbar is in dye units; black lines are bathymetry; gray line is the ice shelf front. X/Y axes indicate simulation grid points from 5 km grid.

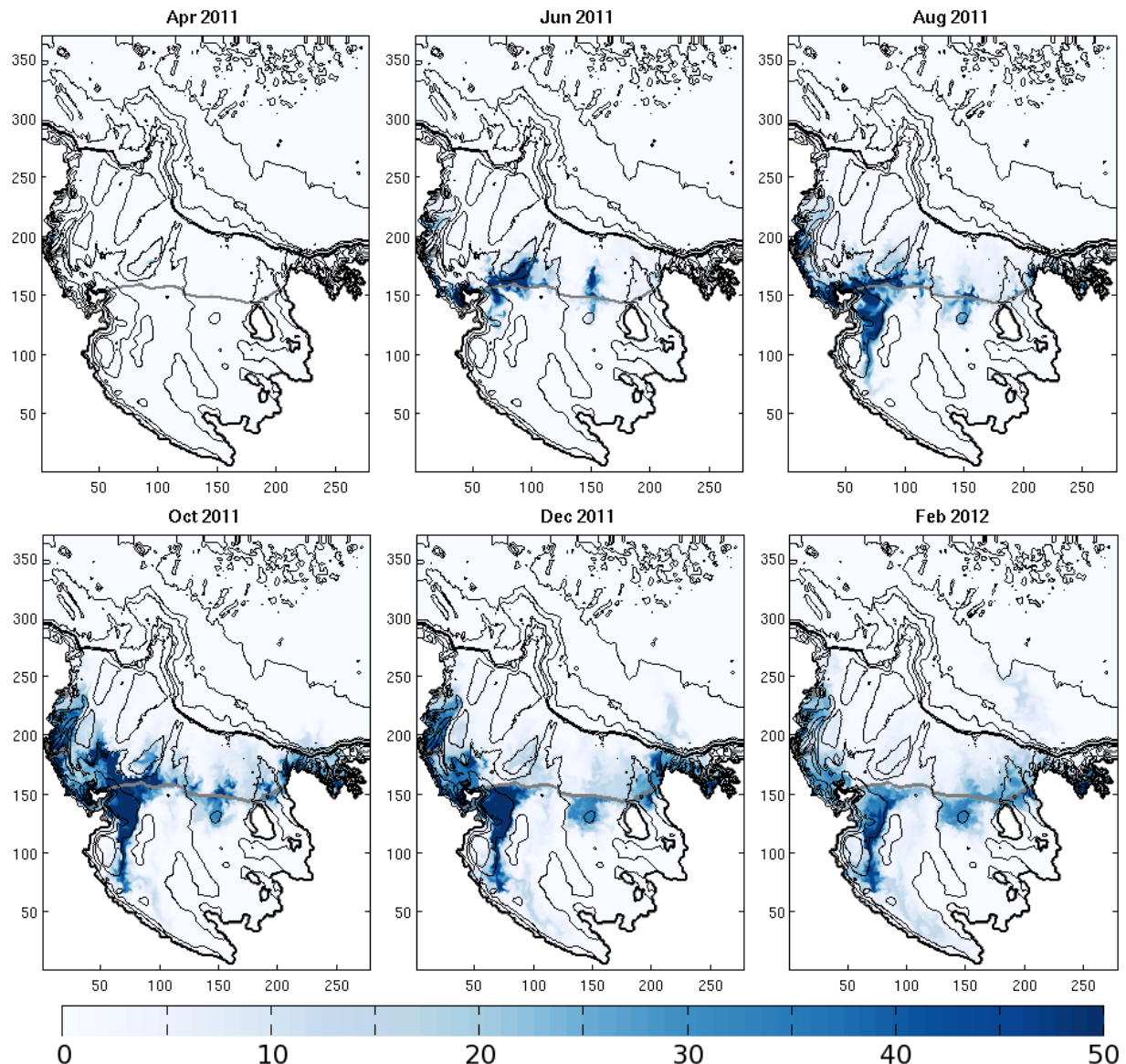


Figure 32. Monthly snapshots of dye_{bdFe} in the top model layer for the last year of simulation 5. Colorbar is in dye units, where the dye is initialized at 100. Black lines are bathymetry contours, gray line is the ice shelf front. X/Y axes indicate simulation grid points. Note the color bar scale is different from Figure 30

vertical mixing and sites of HSSW formation. It also quickly moves under the Ross Ice Shelf at the deep intrusion location, indicating that flushing of the ice shelf cavity extends over all depth levels.

Starting in October, some of the dye leaves the continental shelf in a surface plume from the eastern side of the shelf break. By the beginning of austral summer, the amount of benthic dye in the surface layer on the western side of the continental shelf has significantly decreased from earlier in the year, indicating that the surface dye has dispersed, and the supply of dye from below has stopped due to less vertical mixing in summer. A similar reduction in dye intensity under the western side of the ice shelf also occurs, showing the pathway for that surface dye to be advection from surface waters outside the ice shelf, and not vertical mixing of dye already under the ice shelf at depth.

DJF average dye_{bdFe} at the surface (Figure 33) shows that increased resolution in simulations **1** and **1T** lessens the amount of dye under the western side of the ice shelf indicating that eddies are either decreasing advection under the ice shelf front or suppressing vertical mixing on the southwestern continental shelf, or that increased horizontal resolution allows for steeper bathymetric slopes. The amount of dye on the eastern side of the continental shelf also lessens at higher resolution.

When tidal forcing is added in simulations **5T** and **1T**, there is generally more dye over the entire continental shelf, concentrated on the western side, as tides increase vertical mixing. Likewise, the amount of dye just under the ice shelf front also increases. Interestingly, in all simulations except for **5**, the surface off-shelf plume disappears. One possible explanation for this is that the dye is dispersed vertically due to enhanced vertical mixing from tides at the shelf break, or, at higher resolutions, there simply is not enough dye on the eastern side of the continental shelf to generate the plume.

6.3.2 MIXED LAYER DEPTH

To calculate how much dFe gets to the surface ocean in the simulations, the surface ocean is defined as the SML, or the water above the MLD. Using the method described in section 6.2.3, MLDs are determined for each of the simulations, the PRISM-RS cruise data, and from climatology [Kara *et al.*, 2003] (Table 9). For the simulations and climatology, only MLDs calculated inshore of the simulation defined 700 m isobath are used, while for PRISM-RS cruise data, all MLDs on the continental shelf from CTD and VPR data are used. Based on the SSC for each simulation the average MLD for January–February 2012 does not significantly vary between simulations. Comparison with climatology gives similar MLD

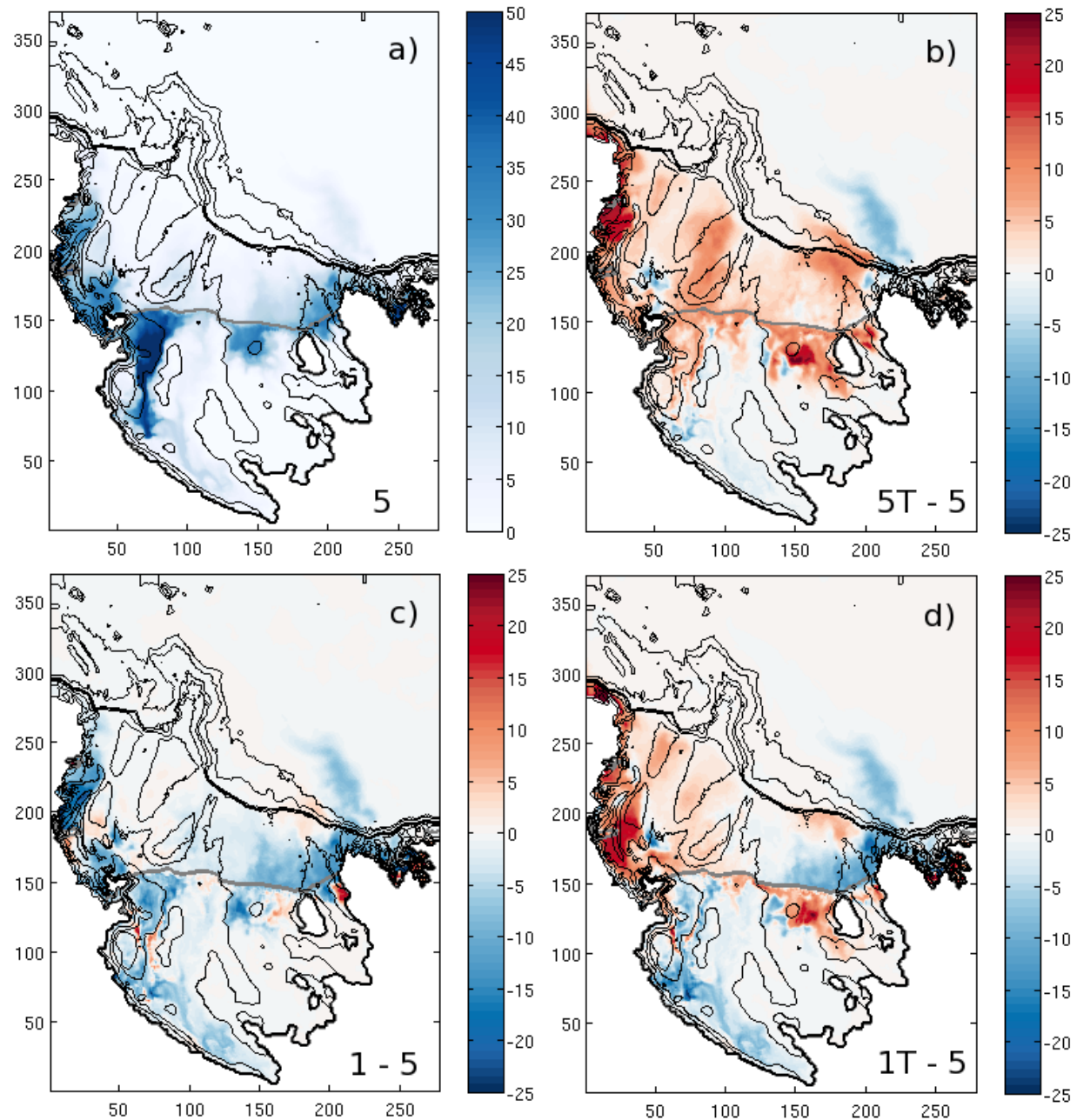


Figure 33. Average amount (DJF) of benthic dye in surface model layer. a) Results from simulation 5; b, c, d) Difference between simulation 5 and 5T, 1, 1T, respectively. Positive values indicate more dye in that simulation, negative values indicate less. Colorbar is in dye units; black lines are bathymetry; gray line is the ice shelf front.

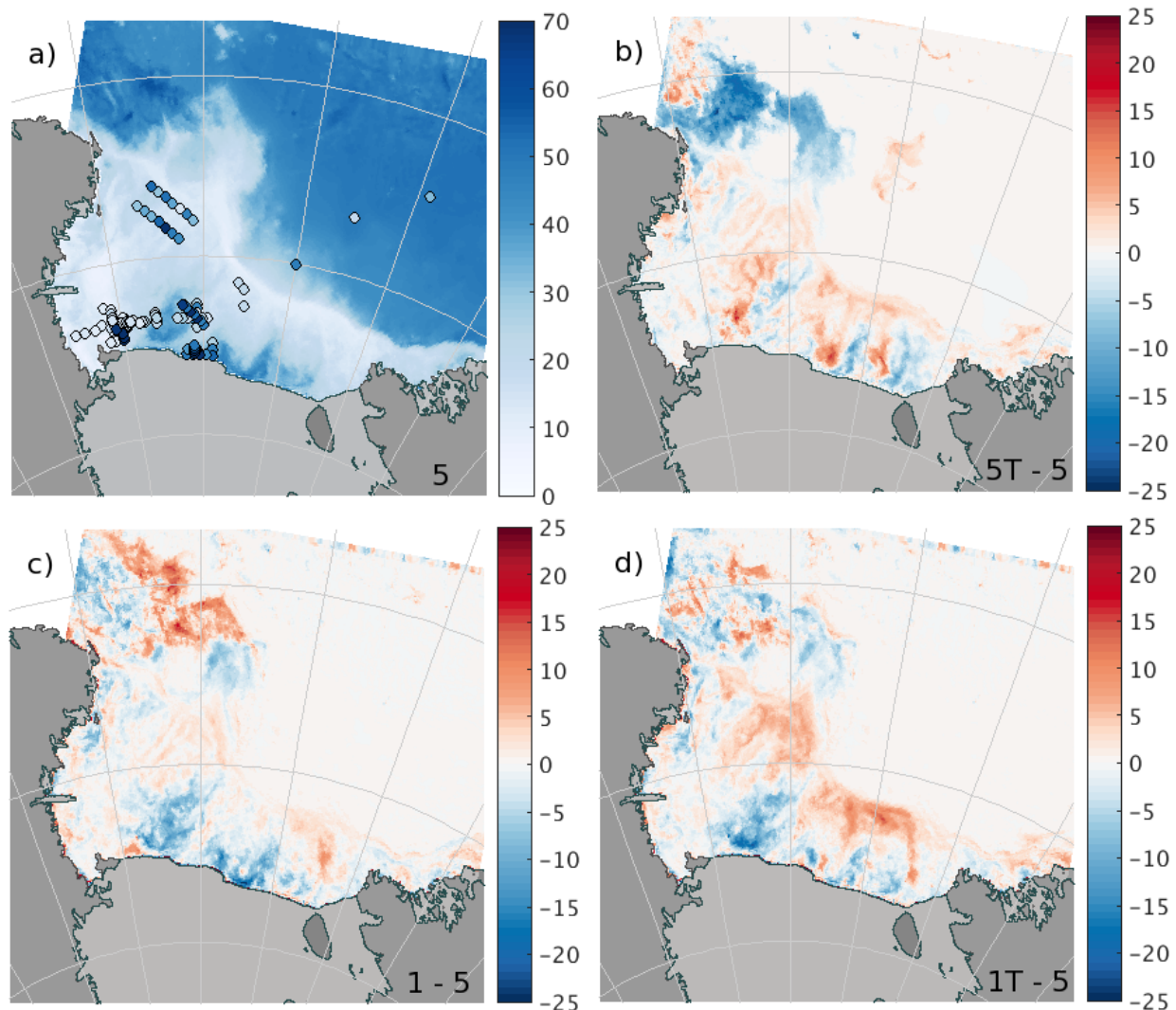


Figure 34. Average mixed layer depth for simulations for January/February. a) Background is simulation 5; dots are MLDs from PRISM-RS CTD stations. b, c, d) Differences between simulation 5 and 5T, 1, 1T, respectively. Positive values indicate increased MLD, negative indicate decreased.

Source	J/F MLD	Stdev	SSC
5	18.32 m	7.63	\pm 1.085 m
5T	18.71 m	7.69	\pm 1.108 m
1	17.63 m	6.31	\pm 1.044 m
1T	18.78 m	6.50	\pm 1.112 m
CTD/VPR	34.36 m	21.31	N/A
Climatology	20.49 m	7.27	N/A

Table 9. Average mixed layer depths (MLDs) on the continental shelf for January through February 2012 from simulations, PRISM-RS cruise data, and global climatologies [Kara *et al.*, 2003], given with standard deviations (Stdev). SSC for simulations is shown as the percentage SSC times the average MLD.

values and similar variability. However, data from the PRISM-RS cruise is quite different, showing a MLD that is significantly deeper, by over 10 m, than climatology or simulation derived values, with much greater variability.

A subset of MLDs from simulations is generated by sub-sampling at CTD stations within 1 hour of the CTD cast. The results are consistent: simulations show an average MLD between 17.17 and 18.20 meters, with standard deviations between 8.07 and 10.31 meters, similar to the January-February averages in Table 9. Areas where simulated MLD differs greatly from observed MLD are along the ice shelf front, and at a few stations over Ross Bank (Figure 34). The discrepancies in MLD at the ice shelf front may be due to biased sampling. Eddies along the ice shelf front were preferentially sampled during the PRISM-RS cruise, and MLDs were much deeper in their cores [Li *et al.*, 2017]. In general the model correctly simulates stations that have relatively shallow MLDs, but has a more difficult time with deeper MLDs, at least during the summer months. There also is no significant improvement in MLD estimation from simulations **5T,1**, or **1T**.

The most likely explanation for this difference in MLDs is the coarseness of resolution of climatological data (1°), and of the atmospheric forcing applied to the model simulations (80 km resolution). A comparison of the PRISM-RS along-track wind speeds with ERA-Interim [Dee *et al.*, 2011] wind speeds used to force the model shows a similar temporal variability, but the maximum observed winds are stronger than those in ERA-Interim (Figure 36). It has previously been shown that increasing the resolution of atmospheric models improves the simulation and strength of coastal winds in the Antarctic [Bromwich *et al.*, 2013; Dinniman *et al.*, 2015] and that this can deepen mixed layers in simulations of the Ross Sea [Mathiot *et al.*, 2012]. Thus the inability of the simulation to accurately represent

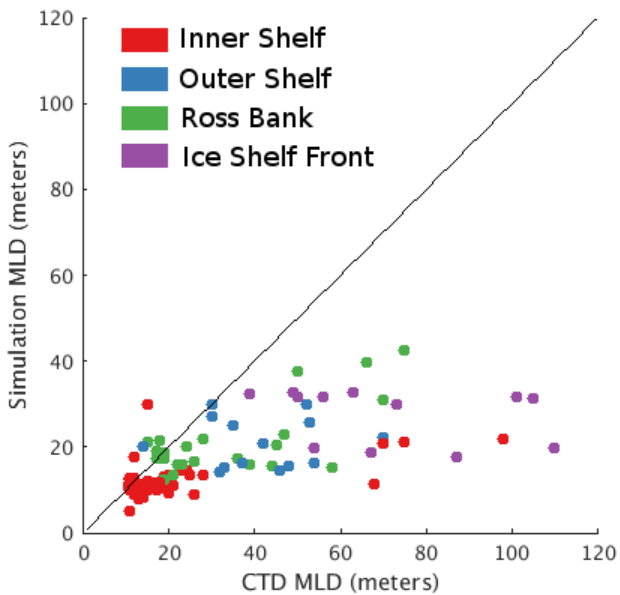


Figure 35. Simulation mixed layer depth (MLD) from simulation 5 at CTD stations and times plotted against CTD observations of MLD. Colors indicate general area of observations.

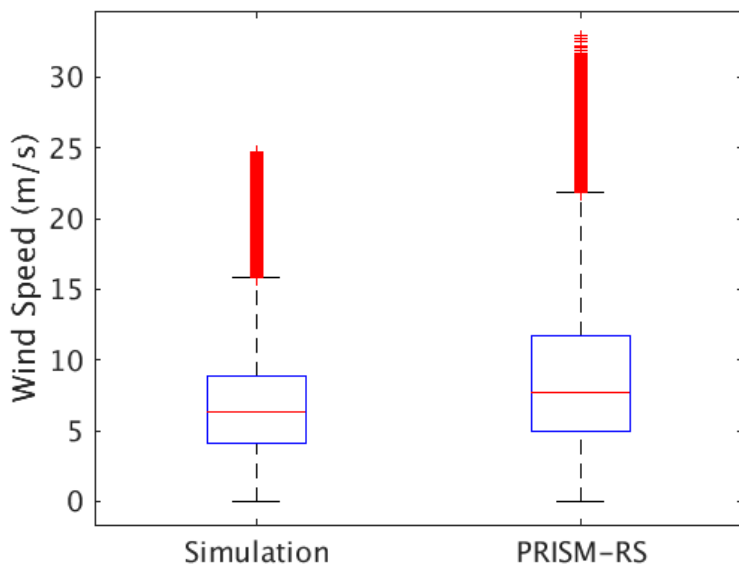


Figure 36. Box plot showing the distributions of wind speeds from PRISM-RS data and from ERA-Interim used to force the model.

MLDs is at least partially the result of the lower resolution of atmospheric data used to force the model.

Comparing the spatial pattern of MLD (Figure 34), the MLDs for the different simulations are by no means the same. When tidal forcing is added to simulation **5**, there is a strong decrease in MLD off-shelf in the northwest region, primarily because tides help break up the retreating sea ice, allowing shallower MLDs to form earlier [Mack *et al.*, 2013]. MLDs on-shelf for simulations **5T** and **1T** show a shift in pattern from their non-tidal counterparts: along the ice shelf front some areas become shallower and some deeper. Adding tides at both resolutions also increases the MLD on the outer portion of the continental shelf, near the shelf break, as tides have the strongest impact there. An increase in horizontal resolution mainly decreases the MLD along the ice shelf front, as eddies that have trapped relatively fresh Ice Shelf Water (ISW) suppress vertical mixing. There are some complex changes to MLD in off-shelf waters in the northwest as this is an area with fairly high eddy activity, modifying MLD at smaller spatial scales.

Overall, while the average MLD does not differ greatly between simulations, the difference in spatial pattern suggests that MLD may play a significant role, alongside actual supply of dFe, in determining how much dFe reaches the SML and is available to support biological production.

6.3.3 DISSOLVED IRON SUPPLY

First, consider the amount of dFe supplied to the SML in each simulation from each source for the final four months of simulation, i.e., the 2011-2012 growing season (Figure 37). These four months cover the time period of the phytoplankton bloom, which can begin as early as mid-November and continues through February [Sedwick *et al.*, 2011]. The large changes in y-axis scale in Figure 37 are mainly due to the shallowing of the SML. All four simulations show the same general characteristics as time progresses. The supply of dFe is dominated by dye_{bdFe} in November and December, and decreases as the mixed layer shallows in summer. As sea ice begins to melt, the contribution from dye_{SIM} increases, roughly matching that of dye_{CDW} in December, and then dominating in January and February. The amount of dye_{bdFe} significantly decreases with increased resolution (**1** and **1T**) in all months due to shallower MLDs near the ice shelf front, and decreased vertical mixing on-shelf. At the same time, dye_{bdFe} increases with tides in all months, rendering the net effect of tides and eddies not significant (5 vs 1T). Dye_{CDW} shows a similar effect - it increases with the addition of tidal forcing, as tides increase the amount CDW intruding onto the continental shelf

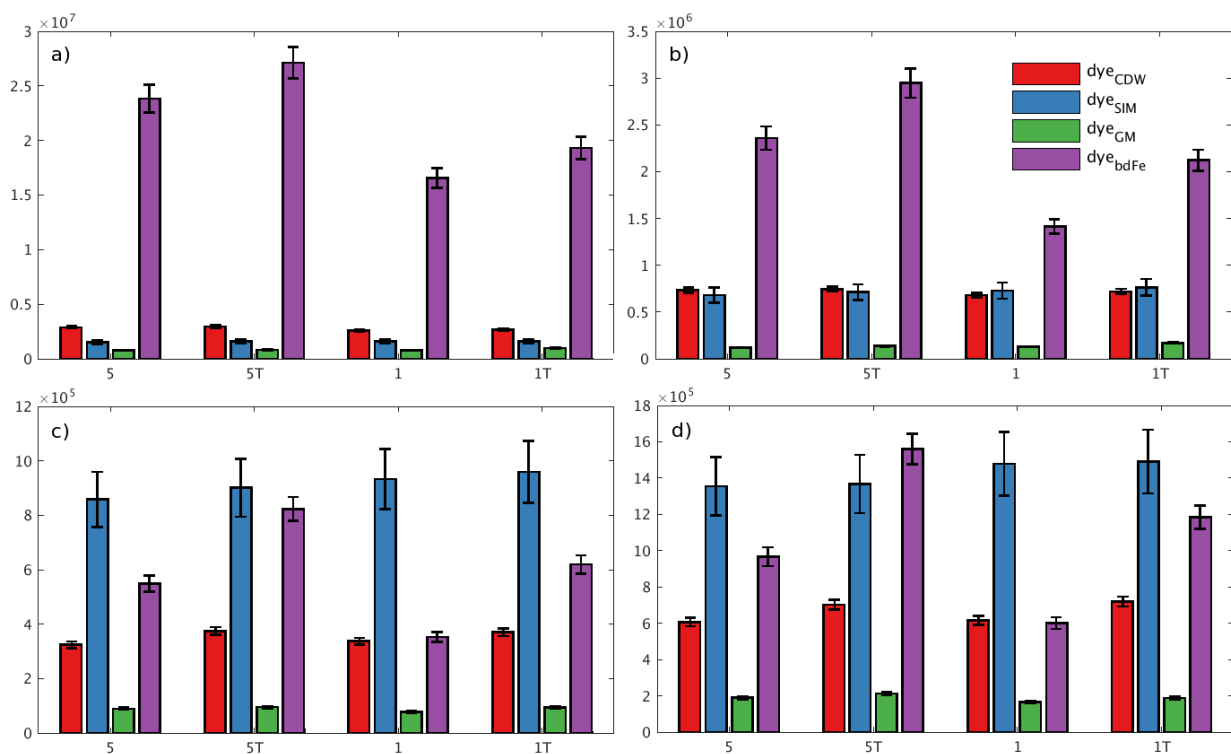


Figure 37. Bar graph showing the contribution of each dFe source to the total amount in the SML on the continental shelf (inshore of 700 m). Units are moles dFe. Error bars are SSC. a) November, b) December, c) January, d) February.

(**5T** and **1T**), although the magnitude is much less than the changes seen with dye_{bdFe} . Tidal forcing also increases the amount of dye_{GM} in all months except November, as tidal rectification induces more exchange of waters across the ice shelf front and thus more melting. However, this contribution is by far the smallest of the four sources. Dye_{SIM} does not show a significant difference in the amount of dFe supplied between different simulations. Based on this representation of dFe in the SML, January is the first month in which all dye sources are fully developed, and the ice is melted enough to allow a significant spring bloom of phytoplankton.

The spatial distribution of dFe in the mixed layer on the continental shelf (inshore of 700 m) in January illustrates specifically where the total dFe supplied differs between each simulation (Figure 38). In general, there are higher concentrations of dFe on the western side of the continental shelf, with the lowest amounts on the middle of the continental shelf. When the horizontal resolution is increased (simulations **1** and **1T**), the concentration of dFe on the eastern side of the continental shelf decreases while the smaller scale variability along the western side of the continental shelf shifts. With the addition of tidal forcing (simulations **5T** and **1T**), the amount of dFe increases over almost the entire continental shelf, and is greatest on the western edge where tides are the strongest.

Iron supply on the continental shelf in the SML separates into two distinct regions: areas on the outer portion of the continental shelf or on the western side that are dominated primarily by sea ice melt (dye_{SIM}), and areas on the inner continental shelf that are dominated by benthic iron supply (dye_{bdFe}) (Figure 39). Dye_{CDW} is the dominant source only over portions of Ross Bank in simulations **5** and **1**. Glacial melt (dye_{GM}) only dominates at locations under the ice shelf. We define dominance simply as the source that makes up the greatest percentage of dFe in each grid cell. If the threshold for the speckled areas (Figure 39) is set to 50%, the entire model domain, except for some areas along the edge of the ice shelf front, is speckled. Similarly, if it is set to 90%, only a few areas off-shelf dominated by sea ice melt, and deep under the ice shelf on the eastern side, are speckled. This indicates that even though some areas are clearly dominated by one process, there is no location on the continental shelf that is supplied by only one source. Thus, to understand the supply of dFe on the continental shelf, a comprehensive source analysis is indeed necessary.

6.4 DISCUSSION & CONCLUSIONS

The formulation of dye_{bdFe} in the model, despite the lack of information regarding direct efflux from sediment and remineralization rates, provides a reasonable representation of how

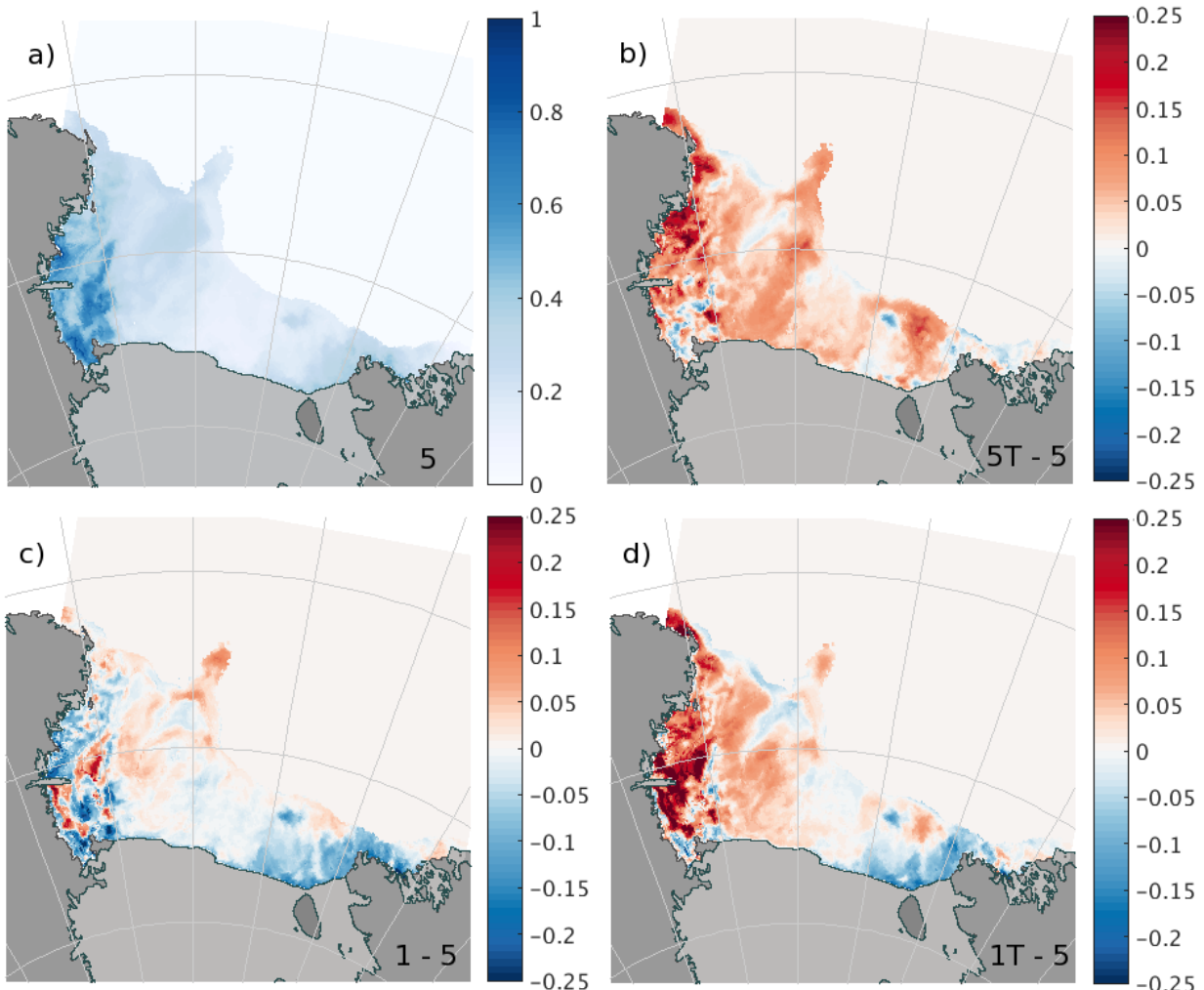


Figure 38. Dissolved iron supply (nM) in the surface mixed layer on the continental shelf (inshore of 700 m) for January. a) Simulation 5. b, c, d) Differences between simulation 5 and simulations 5T, 1, 1T, respectively. Positive values indicate more dFe in the simulation, negative values indicate less.

Source	5	5T	1	1T	SSC
<i>dye_{CDW}</i>	1.25	1.37	1.22	1.35	± 3.82%
<i>dye_{SIM}</i>	2.17	2.24	2.34	2.40	± 11.80%
<i>dye_{GM}</i>	0.30	0.33	0.28	0.33	± 4.11%
<i>dye_{bdf}</i>	2.91	4.00	1.77	2.93	± 5.35%
Total	6.63	7.95	5.60	7.01	± 3.83%

Table 10. Total dFe in the SML for each simulation from each source on the continental shelf (inshore of 700 m, averaged over DJF). Units are $\mu\text{mol m}^{-2} \text{yr}^{-1}$. Final row shows the total dFe supplied from each simulation.

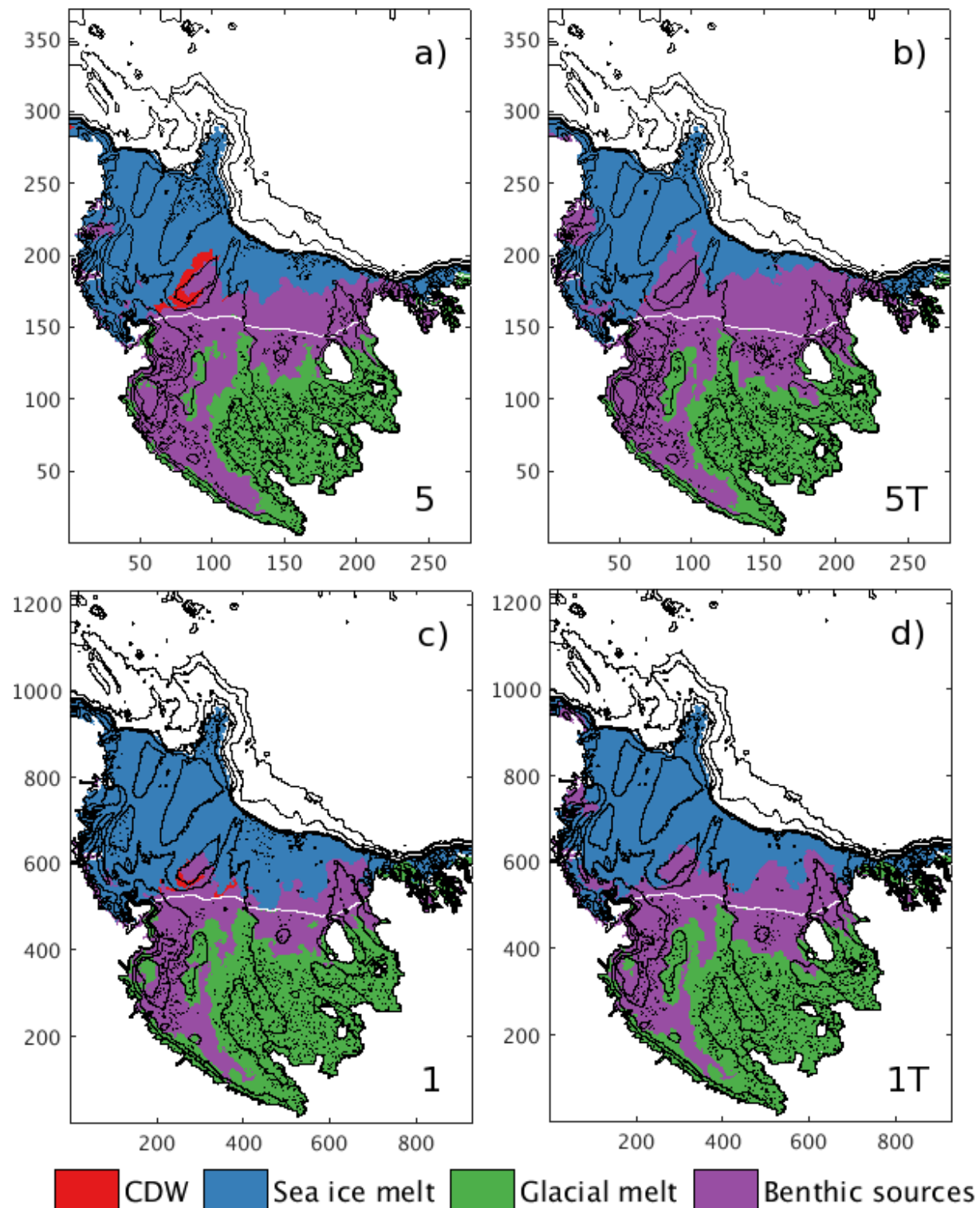


Figure 39. Color indicates dominant source of surface layer dFe for January 2012 for simulations a) 5, b) 5T, c) 1, d) 1T. Speckled areas indicate that source provides at least 75% of dFe. Solid black lines are bathymetry; white line is ice shelf front.

much benthic dFe is supplied to the SML. Results from *McGillicuddy et al.* [2015] give a total dFe supply of about $7.8 \mu\text{mol m}^{-2} \text{ yr}^{-1}$, while simulation estimates range from 5.60 to $7.95 \mu\text{mol m}^{-2} \text{ yr}^{-1}$. As the formulation developed here for dFe supply from CDW, sea ice melt, and glacial melt is similar to *McGillicuddy et al.* [2015], this close correspondence indicates that we are using a reasonable representation for benthic dFe sources. For modeling purposes, an estimate of bottom layer dFe concentration is sufficient, assuming close to steady state. The recent measurements presented by *Marsay et al.* [2014], and their suggested exponential fit of benthic dFe as a function of distance from the sea floor provides a sufficient estimate of benthic dFe concentration on the continental shelf. Similar to *Gerringa et al.* [2015], the inner continental shelf region near the Ross Sea polynya is mostly dominated by benthic sources of dFe.

Estimates of iron supply from different simulations in DJF suggest that CDW supplies 17-22% of dFe to the SML, sea ice melt 28-42%, glacial melt 4-5%, and benthic sources 32-50% (Table 10). The greatest difference between simulations is in the amount supplied by dye_{bdFe} . Tidal forcing increases the dFe supplied by dye_{bdFe} by increasing mixed layer depths and the bottom mixed layer energetics, while increasing horizontal resolution has the opposite effect. A reasonable explanation is that, as eddies were expected to affect the supply of iron from glacial melt the most and that source is an order of magnitude below the others, local effects from eddies re-stratifying the water column override any increase in dye_{GM} supply. This trend holds true for the total dFe from all sources, indicating that changes to the benthic dFe supply in simulations dominate the changes to total supply. Interestingly, the net result from adding tidal forcing and increasing horizontal resolution (**1T**) is not significantly different from the original model configuration (**5**).

Despite a non-significant change in total supply between simulations **5** and **1T**, including tidal forcing and eddy resolving horizontal resolution is necessary to capture the spatial variations in dFe surface concentrations over one year, which vary by up to $\pm 0.25 \text{ nM}$. This is particularly true for the banks and the western portion of the continental shelf, which show a significant increase in the amount of dye_{bdFe} with the addition of tidal forcing.

When considering MLD, and comparing to changes in dFe in different simulations, it is interesting to note that areas with the largest changes in MLD (Figure 34) correspond to areas with the least change in total dFe supply between simulations (Figure 38). Thus the changes to MLD between simulations have a damping effect on the changes in dFe concentration, e.g., a decrease in MLD balances an increase in dFe supply at that location. If a constant MLD is applied across simulations, the differences in dFe supply would be amplified. Also of interest

is that the locations where the model does poorest in predicting observed MLDs correspond to locations that show the greatest changes in MLDs between simulations, specifically over Ross Bank and along the front of the ice shelf. Again, atmospheric data of sufficient resolution to resolve short, high intensity storms may make a significant impact on these results.

Important next steps for this work include determining the impact of including tides and resolving mesoscale eddies for other Antarctic shelf seas when considering biogeochemical processes in a regional context. Tides are particularly strong in parts of the Ross Sea, while the neighboring Amundsen Sea shows significant effects from resolving mesoscale eddies [*St-Laurent et al., 2013*]. Another important advance would be to move past the use of dyes alone and couple a biogeochemical model [*Tagliabue and Arrigo, 2005*] to the physical model of the Ross Sea. Parameterizing biological uptake and scavenging would remove dFe from the model, and simulations run over multiple years would capture inter-annual variability and better constrain the total dFe supply.

CHAPTER 7

CONCLUSION

The primary objective of this thesis was to investigate the effects of tides and mesoscale eddies on the supply of dissolved iron (dFe) to the surface ocean from various sources in the Ross Sea using a regional ocean model. In a series of studies, different parts of this objective were addressed: description and validation of the regional ocean model, representation of mesoscale eddies in the model, the effect of tides on sea ice concentration, and the pathways of dFe to the surface ocean. This concluding chapter synthesizes the results, highlights key points of significance, and describes implications for future research.

7.1 SYNTHESIS OF STUDIES

One of the main themes of this thesis is modeling tides and mesoscale eddies in the Ross Sea and examining their effects on various processes. In general, the effect of tides varies depending on the temporal and spatial scale of the processes of interest. For example, in the water mass volumetric census that formed part of the model validation in Chapter 3, tides had no significant effect on the water mass volumes on the continental shelf. However, adding tidal forcing did significantly increase the basal melt rate of the Ross Ice Shelf to produce Ice Shelf Water (ISW) (increase in melt rate of 14% with tides). When considering the supply of dFe to the surface ocean in Chapter 6, tides affected the spatial distribution of dFe supply as well as the total dFe from all sources (20% increase with tides). Each individual source, with the exception of sea ice melt, also showed a significant increase with tidal forcing.

These examples demonstrate that tidal forcing is important over a large range of spatial scales. Tides in the Ross Sea interact strongly with bathymetry, in part due to the weak stratification. Thus tides, and processes affected by tides, show significant spatial variability over bathymetric features, such as the continental shelf break and shallow banks on the shelf. Temporally, tides have a significant effect on processes that vary at seasonal or smaller time scales, as indicated by dFe supply and ice shelf basal melt. Large, integrated quantities, such as water mass volumes, are more resilient to the effects of tidal forcing. As regional ocean models tend to address issues at scales smaller than averages over the entire continental

shelf, e.g. ice shelf basal melt rates, fluxes of water, or transport of heat across certain areas, tides of the magnitude found in the Ross Sea are a necessary component to include.

The effect of mesoscale eddies is not as clear as that of tidal forcing. Modeling mesoscale eddies in the Ross Sea is a complex endeavor, as covered in Chapter 4. The weak stratification in the Ross Sea, especially during winter months, indicates that there is not much excess energy to generate eddies, and those that form are small and short-lived. Despite this, there is a significant increase in the baroclinic Eddy Kinetic Energy and number of eddies found when the horizontal resolution was increased from 5 km to 1.5 km. Similar to tidal forcing, eddies affect the spatial pattern of dFe from different sources, and are significant at small temporal scales as well. The total effect of eddies on the supply of dFe is similar in magnitude to that of tides, but opposite in direction (15% decrease in total dFe); the combination of tides and mesoscale eddies in a simulation shows a non-significant change to the total dFe supply.

These results, indicating that tides and mesoscale eddies have a similar contribution to the total dFe supply to the surface ocean (but opposite in sign), suggest that both are important to include in models of the Ross Sea. However, if the computational cost is considered, the story changes somewhat. Adding tidal forcing to this regional ocean model increased computational run time by 40%, most of which was due to a smaller time step to account for faster velocities. Increasing the horizontal resolution from 5 km to 1.5 km increased the number of core hours needed by a factor of 36. Add to this that the changes seen with the difference in horizontal resolution may be partially attributed to sharper bathymetry contours at smaller resolution, and the benefit to resolving mesoscale eddies in the Ross Sea is low compared to the total cost.

7.2 SIGNIFICANCE OF RESULTS

One key outcome these studies demonstrate is the relative role of tides and mesoscale eddies. There is currently a push in the Antarctic shelf seas modeling community to increase horizontal resolution and resolve mesoscale eddies as the best way to improve models. This research is a check to that assumption, showing that in the Ross Sea, tides have a similar, if not greater, impact than eddies. At substantially lower computational costs, improving a model by adding tides gives a much higher benefit to cost ratio. However, not all Antarctic shelf seas are the same. The neighboring Amundsen Sea and West Antarctic Peninsula regions both tend to be more strongly stratified than the Ross Sea, increasing the size and potential impact of eddies, and suggesting that higher horizontal resolution would be

beneficial. Further along the coast, the Weddell Sea has semi-diurnal tides that can reach similar magnitudes as the diurnal tides in the Ross Sea [Robertson *et al.*, 1998], suggesting that including tidal forcing is important. In general, the heterogeneity of Antarctic shelf seas indicates that some thought needs to be taken when considering how to improve regional ocean models. Increasing horizontal resolution across the board may not be the smartest or most efficient way to improve these models.

Aside from providing an overview of the role of tides and mesoscale eddies in the Ross Sea, there are several other developments of significance to the greater oceanographic community. One of them is the development of the Simulation Significance Criterion (SSC) used to determine significance between similar simulations. Regional ocean models, like the one used here, are often finely detailed and too computationally expensive to run for ensemble statistics. Comparisons between simulations with slightly different configurations could either use observations to determine which simulation matches more closely to reality, or could simply compare simulations to each other without a measure for significance. The SSC is a way to estimate model variability at sub-annual timescales, and use the relative magnitude of the variability to establish a threshold for significance. Thus, in places with extreme conditions, like the Ross Sea, it is possible to determine the significance of differences between simulations without a reference observation for comparison. SSC has the potential to be used as a relatively simple tool for comparing and contrasting simulations from any regional ocean model.

This thesis also demonstrated the development and usefulness of passive tracer dyes. Three of the passive tracer dyes were previously developed and added to earlier versions of the Ross Sea model [Dinniman *et al.*, 2007, 2011]. In Chapter 6 the development of a fourth dye, the benthic dFe tracer (dye_{bdFe}), is detailed. The formulation of dye_{bdFe} is simplistic, as it does not include dFe specific processes, such as scavenging or uptake by phytoplankton. The pathways of dye_{bdFe} over time show where dFe from the benthic layer ascends to the surface ocean, and also the location of deep mixing over the continental shelf, deep flushing pathways under the Ross Ice Shelf, and some of the export of dense water from the shelf. The other three dyes are likewise useful in tracking water masses and transformations. For example, the water mass analysis from Chapter 3 determined the relative volumes of the water masses on the continental shelf. The amount of dye_{CDW} in each of these water masses over time illustrated the transformation of Circumpolar Deep Water (CDW) into other water masses on the shelf.

Finally, this thesis investigated the existence of what can be described as a tidal polynya

near the northwest portion of the continental shelf break. A new analysis of sea ice concentration from satellite swath data shows an area of partially open water during austral winter that is driven by tidal divergence. The opening in the sea ice allows large fluxes of heat from the ocean to the atmosphere. This heat could energize storms in the area and the loss of heat from the ocean could lead to more sea ice production, as suggested by simulations. The new analysis method can be applied to any high latitude location with any sun-synchronous satellite in a near polar orbit, and the data analyzed here confirms the existence of a polynya in the Ross Sea driven by divergence of flow. Typically, polynyas are characterized as latent heat polynyas that are driven by wind blowing ice away from a coast and have high sea ice production, such as the polynya in front of the Ross Ice Shelf, or as sensible heat polynyas that are driven by ocean heat and have low to zero ice production. This tidal polynya is similar to the characteristics of a latent heat polynya: the opening in the ice is mechanically driven, and although there may not be cold winds to quickly cool the ocean surface, sea ice can still form on the open water. The main difference is that a tidal polynya is regular in opening and closing, as it follows the tidal cycle, instead of being driven by sporadic or consistent winds.

7.3 IMPLICATIONS FOR FUTURE RESEARCH

The most obvious implications for future research from this series of studies concerns how to improve the Ross Sea model. One way to make improvements is to improve the model forcing. In Chapter 3, the deep on-shelf salinity values in the simulations are consistently saltier than the PRISM-RS CTD observations. This offset can be attributed to the freshening of the Ross Sea in recent years, as the boundary conditions are derived from climatological values that span several decades. A relatively simple fix is to adjust the boundary salinity by the estimated amount of freshening to match the hindcast time. However, the freshening would be applied as an average; there is not enough information to constrain any seasonality or spatial variability to the freshening signal.

Likewise, the analysis of mixed layer depths (MLDs) in Chapter 6 showed that the simulation MLDs are not deep enough. One possibility is that the atmospheric forcing lacks short, high intensity storms, leading to less wind-driven mixing. It is not possible with the current data available to increase the level of detail in the atmospheric forcing. Instead, improvements would most likely come from coupling an atmospheric model to the current ocean-sea ice model configuration. Another option is to use the distribution of wind speed from the PRISM-RS cruise observations to adjust the forcing values so the distributions match. This

will not improve the comparison to PRISM-RS observations, as the high intensity events in the adjusted forcing will not match where and when they occurred in reality. However, by comparing a simulation with adjusted wind forcing to one without, it is possible to estimate the impact wind forcing has on MLD and determine if this is the reason the simulation MLDs are shallower than the PRISM-RS observations. A second possibility to increase the MLDs in the simulations is to add a parameterization of wave-induced turbulence. Recent research [*Qiao et al.*, 2016] indicates that wave-turbulence interaction enhances near surface turbulence, and that including a parameterization of this interaction improves model (including ROMS) predictions of MLDs in off-shelf waters. It is possible that this parameterization will offer similar improvements to MLDs on-shelf.

Another model improvement, mentioned in Chapter 3, is adding a parameterization for frazil ice formation under the ice shelf [*Galton-Fenzi et al.*, 2012]. This would potentially improve the plume dynamics of ISW and give a better estimate of the volume of ISW on the continental shelf. A more radical approach would be to replace the static ice shelf and the parameterizations of pressure, heat, and salt fluxes with an ice shelf model. This would give the benefit of including processes such as frazil ice formation more explicitly and allow the model to be used for further investigations of ocean-ice shelf interactions. The coupling of ocean and ice shelf models is currently an active research topic, as basal melt of the ice shelves around Antarctica is thought to contribute to ice shelf thinning, instability, and even collapse [*Depoorter et al.*, 2013; *Jacobs et al.*, 2011; *Goldberg et al.*, 2009]. However the Ross Ice Shelf is relatively slow moving (about 1 km yr^{-1}), and slowly melting ($10 \pm 10 \text{ cm yr}^{-1}$), implying the computational costs of coupling another model to the current configuration may not be worth the additional benefit of explicitly modeling the melting of the ice shelf.

A final potential improvement is a further increase in horizontal resolution. Chapter 4 illustrates the weak stratification in the Ross Sea and the subsequent small baroclinic radius of deformation, especially in the winter months. Thus, while the increase in horizontal resolution used in this thesis resolved the mesoscale, it did not resolve all first mode baroclinic eddies. It is likely these small sub-mesoscale eddies are short-lived and do not play a major role in the transport of dFe. However, one way to confirm this is to explicitly resolve all first mode baroclinic eddies on the continental shelf. Given the computational expense to increasing horizontal resolution, using the current Ross Sea model configuration is not the best option. Instead, a process model (similar to the one described in *St-Laurent et al.* [2013]), with conditions mimicking those found on the Ross Sea continental shelf and a much smaller domain, could be used to investigate the possibility and potential effect of baroclinically

generated sub-mesoscale eddies. However, caution is advised in increasing resolution further using ROMS, as ROMS currently does not include a non-hydrostatic component.

The model analysis presented in these studies does more than suggest ways to build a better model. It also provides a commentary on what processes need to be further investigated and what could be done to improve observations. One of the striking results overall is the spatial heterogeneity seen in many of the simulated variables. Estimates of dFe supply from the various sources, even after being averaged over several months, show up to $\pm 50\%$ changes across the continental shelf when comparing simulations. High spatial variability is also seen in MLDs, and in the dominant source of dFe to the surface ocean. Interestingly, the areas with the largest changes to dFe supply when mesoscale eddies are considered are not the same areas that show large increases in the number of eddies (compare Figure 18 to Figure 38). This high spatial variability indicates the need to make observations sufficiently close in space to capture the small scale variability, but also spread across the shelf, as the eastern side of the shelf often does not have the same response as the western side.

Another area where specific observations could improve model estimates is with the dFe end members for the passive tracer dyes. The current numbers used are averaged over large areas (one value for the entire ice shelf, one for all sea ice, etc...), and subsequently have very large errors attached [McGillicuddy *et al.*, 2015]. More measurements could better refine these numbers and potentially provide information on their spatial or temporal variability. Similarly, it was only with the recent PRISM-RS cruise that enough data was available to make an estimate of the end member for dye_{bdFe} . The data available restricted the formulation of the dye. Instead of using two separate dyes, one input as a direct flux from the sediments, and another as a function of remineralization rate at depth, both these processes were grouped together as one source. Observational estimates of the magnitude of each would allow them to be separated in the model and their contributions to surface dFe supply could be determined individually. Finally, more observations under the ice shelf would help constrain the model. In the current configuration, dye_{bdFe} is not extended under the ice shelf, as there are no measurements. However, there is no obvious reason that dFe would not come from the sediments there just as well as from the sediments at deep locations on the shelf. Similarly, there is no estimate of the number and position of sub-glacial rivers that run under the ice sheet and meet the ocean at the grounding line. These are potentially large point sources of dFe that are not accounted for in the model, and if enough data were available, they could be analyzed as a separate source as well.

In conclusion, this thesis investigated the physical processes controlling the supply of dFe

to the surface mixed layer using a regional ocean model, with a specific focus on tides and mesoscale eddies. Eddy theory, as it applies to the Ross Sea, was detailed to explain the small, short-lived eddies seen in simulations, and the effect of tides on sea ice concentration was explored using satellite data. This thesis has implications for the future of the Ross Sea model as well as other models of Antarctic shelf seas, and illustrates areas where more observations would be useful.

REFERENCES

- Arndt, J. E., H. W. Schenke, M. Jakobsson, F. O. Nitsche, G. Buys, B. Goleby, M. Rebesco, F. Bohoyo, J. Hong, J. Black, R. Greku, G. Udintsev, F. Barrios, W. Reynoso-Peralta, M. Taisei, and R. Wigley (2013), The International Bathymetric Chart of the Southern Ocean (IBCSO) Version 1.0 - A new bathymetric compilation covering circum-Antarctic waters, *Geophys. Res. Lett.*, 40(12), 3111–3117, doi:10.1002/grl.50413.
- Arrigo, K. R., G. L. van Dijken, and S. Bushinsky (2008), Primary production in the Southern Ocean, 1997–2006, *J. Geophys. Res.*, 113(C08004), doi:10.1029/2007JC004551.
- Årthun, M., P. R. Holland, K. W. Nicholls, and D. L. Feltham (2013), Eddy-driven exchange between the open ocean and a sub-ice shelf cavity, *J. Phys. Oceanogr.*, 43(11), 2372–2387, doi:10.1175/JPO-D-13-0137.1.
- Arzeno, I. B., R. C. Beardsley, R. Limeburner, B. Owens, L. Padman, S. R. Springer, C. L. Stewart, and M. J. Williams (2014), Ocean variability contributing to basal melt rate near the ice front of Ross Ice Shelf, Antarctica, *J. Geophys. Res.*, 119(7), 4214–4233.
- Assmann, K. M., and R. Timmermann (2005), Variability of dense water formation in the Ross Sea, *Ocean Dyn.*, 55, 68–87, doi:10.1007/s10236-004-0106-7.
- Ballard, G., D. Jongsomjit, S. D. Veloz, and D. G. Ainley (2012), Coexistence of mesopredators in an intact polar ocean ecosystem: The basis for defining a Ross Sea marine protected area, *Biol. Conserv.*, 156, 72–82, doi:10.1016/j.biocon.2011.11.017.
- Boccaletti, G., R. Ferrari, and B. Fox-Kemper (2007), Mixed layer instabilities and restratification, *J. Phys. Oceanogr.*, 37, 2228–2250, doi:10.1175/JPO3101.1.
- Box, G. E., and N. R. Draper (1987), *Empirical model-building and response surfaces*, vol. 424, Wiley New York.
- Boyd, P. W. (2002), Environmental factors controlling phytoplankton processes in the Southern Ocean, *J. Phycol.*, 38(5), 844–861, doi:10.1046/j.1529-8817.2002.t01-1-01203.x.
- Boyd, P. W., A. J. Watson, C. S. Law, E. R. Abraham, T. Trull, R. Murdoch, D. C. E. Bakker, A. R. Bowie, K. O. Buesseler, H. Chang, M. Charette, P. Croot, K. Downing, R. Frew, M. Gall, M. Hadfield, J. Hall, M. Harvey, G. Jameson, J. LaRoche, M. Liddicoat,

- R. Ling, M. T. Maldonado, R. M. McKay, S. Nodder, S. Pickmere, R. Pridmore, S. Rintoul, K. Safi, P. Sutton, R. Strzepek, K. Tanneberger, S. Turner, A. Waite, and J. Zeldis (2000), A mesoscale phytoplankton bloom in the polar Southern Ocean stimulated by iron fertilization, *Nature*, *407*(6805), 695–702, doi:10.1038/35037500.
- Boyd, P. W., K. R. Arrigo, R. Strzepek, and G. L. van Dijken (2012), Mapping phytoplankton iron utilization: Insights into Southern Ocean supply mechanisms, *J. Geophys. Res.*, *117*(C06009), doi:10.1029/2011JC007726.
- Bromwich, D. H., J. F. Carrasco, Z. Liu, and R.-Y. Tzeng (1993), Hemispheric atmospheric variations and oceanographic impacts associated with katabatic surges across the Ross Ice Shelf, Antarctica, *J. Geophys. Res. Atmos.*, *98*(D7), 13,045–13,062.
- Bromwich, D. H., F. O. Otieno, K. M. Hines, K. W. Manning, and E. Shilo (2013), Comprehensive evaluation of polar weather research and forecasting model performance in the Antarctic, *J. Geophys. Res. Atmos.*, *118*(2), 274–292, doi:10.1029/2012JD018139.
- Budgell, W. P. (2005), Numerical simulation of ice-ocean variability in the Barents Sea region, *Ocean Dyn.*, *55*, 370–387, doi:10.1007/s10236-005-0008-3.
- CCAMLR (2016), CCAMLR to create world's largest Marine Protected Area, Available from: <https://www.ccamlr.org/node/92518>.
- Charney, J. G. (1947), The dynamics of long waves in a baroclinic westerly current, *J. Meteor.*, *4*(5), 136–162.
- Charney, J. G. (1971), Geostrophic Turbulence, *J. Atmos. Sci.*, *28*(6), 1087–1095.
- Chelton, D. B., R. A. DeSzoeke, M. G. Schlax, K. E. Naggar, and N. Siwertz (1998), Geographical variability of the first baroclinic Rossby radius of deformation, *J. Phys. Oceanogr.*, *28*, 433–460.
- Chelton, D. B., M. G. Schlax, R. M. Samelson, and R. A. de Szoeke (2007), Global observations of large oceanic eddies, *Geophys. Res. Lett.*, *34*(15), 1–5, doi:10.1029/2007GL030812.
- Chen, R., A. F. Thompson, and G. R. Flierl (2016), Time-Dependent Eddy-Mean Energy Diagrams and Their Application to the Ocean, *J. Phys. Oceanogr.*, *46*(9), 2827–2850, doi:10.1175/JPO-D-16-0012.1.

- Cleveland, R. B., W. S. Cleveland, J. E. McRae, and I. Terpenning (1990), STL: A seasonal-trend decomposition procedure based on Loess, *J. Off. Stat.*, 6(1), 3–73, doi:citeulike-article-id:1435502.
- Comiso, J. C. (2009), Enhanced sea ice concentrations and ice extents from AMSR-E data, *J. Remote Sensing Soc. Japan*, 29(1), 199–215.
- Comiso, J. C., R. Kwok, S. Martin, and A. L. Gordon (2011), Variability and trends in sea ice extent and ice production in the Ross Sea, *J. Geophys. Res.*, 116(C04021).
- de Boyer Montégut, C., G. Madec, A. S. Fischer, A. Lazar, and D. Iudicone (2004), Mixed layer depth over the global ocean: An examination of profile data and a profile-based climatology, *J. Geophys. Res.*, 109(C12003), doi:10.1029/2004JC002378.
- Dee, D. P., S. M. Uppala, A. J. Simmons, P. Berrisford, P. Poli, S. Kobayashi, U. Andrae, M. A. Balmaseda, G. Balsamo, P. Bauer, P. Bechtold, A. C. M. Beljaars, L. van de Berg, J. Bidlot, N. Bormann, C. Delsol, R. Dragani, M. Fuentes, A. J. Geer, L. Haimberger, S. B. Healy, H. Hersbach, E. V. Holm, L. Isaksen, P. Kållberg, M. Köhler, M. Matricardi, A. P. McNally, B. M. Monge-Sanz, J. J. Morcrette, B. K. Park, C. Peubey, P. de Rosnay, C. Tavolato, J. N. Thépaut, and F. Vitart (2011), The ERA-Interim reanalysis: configuration and performance of the data assimilation system, *Q. J. R. Meteorol. Soc.*, 137, 553–597, doi:10.1002/qj.828.
- Depoorter, M., J. Bamber, J. Griggs, J. Lenaerts, S. Ligtenberg, M. van den Broeke, and G. Moholdt (2013), Calving fluxes and basal melt rates of Antarctic ice shelves, *Nature*, 502(7469), 89–92.
- Dickey, T. D. (1991), The emergence of concurrent high-resolution physical and bio-optical measurements in the upper ocean and their applications, *Rev. Geophys.*, 29(3), 383, doi:10.1029/91RG00578.
- Dinniman, M. S., J. M. Klinck, and W. O. Smith (2003), Cross-shelf exchange in a model of the Ross Sea circulation and biogeochemistry, *Deep Sea Res. Pt II*, 50, 3103–3120, doi:10.1016/j.dsr2.2003.07.011.
- Dinniman, M. S., J. M. Klinck, and W. O. Smith (2007), Influence of sea ice cover and icebergs on circulation and water mass formation in a numerical circulation model of the Ross Sea, Antarctica, *J. Geophys. Res.*, 112(C11013), doi:10.1029/2006JC004036.

- Dinniman, M. S., J. M. Klinck, and W. O. Smith (2011), A model study of Circumpolar Deep Water on the West Antarctic Peninsula and Ross Sea continental shelves, *Deep Sea Res. Pt II*, 58, 1508–1523, doi:10.1016/j.dsr2.2010.11.013.
- Dinniman, M. S., J. M. Klinck, L.-S. Bai, D. H. Bromwich, K. M. Hines, and D. M. Holland (2015), The Effect of Atmospheric Forcing Resolution on Delivery of Ocean Heat to the Antarctic Floating Ice Shelves, *J. Clim.*, 28(15), 6067–6085, doi:10.1175/JCLI-D-14-00374.1.
- Dong, S., J. Sprintall, S. T. Gille, and L. Talley (2008), Southern Ocean mixed-layer depth from Argo float profiles, *J. Geophys. Res.*, 113(C06013), doi:10.1029/2006JC004051.
- Durski, S. M. (2004), Vertical mixing schemes in the coastal ocean: Comparison of the level 2.5 Mellor-Yamada scheme with an enhanced version of the K profile parameterization, *J. Geophys. Res.*, 109(C1), C01,015, doi:10.1029/2002JC001702.
- Eady, E. T. (1949), Long waves and cyclone waves, *Tellus*, 1(3), 33–52.
- Eisen, O., and C. Kottmeier (2000), On the importance of leads in sea ice to the energy balance and ice formation in the Weddell Sea, *J. Geophys. Res.*, 105, 14,045–14,060.
- Erofeeva, S., L. Padman, and G. Egbert (2005), Assimilation of ship-mounted ADCP data for barotropic tides: Application to the Ross Sea, *J. Atmos. Oceanic Technol.*, 22(6), 721–734.
- Ferrari, R., and C. Wunsch (2009), Ocean Circulation Kinetic Energy: Reservoirs, Sources, and Sinks, *Annu. Rev. Fluid Mech.*, 41(1), 253–282, doi:10.1146/annurev.fluid.40.111406.102139.
- Flather, R. (1976), A tidal model of the northwest European continental shelf, *Mem. Soc. R. Sci. Liege*, 10(6), 141 – 164.
- Foldvik, A., T. Gammelsrød, and T. Tørresen (1985), Hydrographic observations from the Weddell Sea during the Norwegian Antarctic research expedition 1976/77, *Polar Res.*, pp. 177–193.
- Foreman, M. (1977), Manual for tidal heights analysis and prediction, *Pacific Marine Science Report*, 79, 15–70.

Fretwell, P., H. D. Pritchard, D. G. Vaughan, J. L. Bamber, N. E. Barrand, R. Bell, C. Bianchi, R. G. Bingham, D. D. Blankenship, G. Casassa, G. Catania, D. Callens, H. Conway, A. J. Cook, H. F. J. Corr, D. Damaske, V. Damm, F. Ferraccioli, R. Forsberg, S. Fujita, Y. Gim, P. Gogineni, J. A. Griggs, R. C. A. Hindmarsh, P. Holmlund, J. W. Holt, R. W. Jacobel, A. Jenkins, W. Jokat, T. Jordan, E. C. King, J. Kohler, W. Krabill, M. Riger-Kusk, K. A. Langley, G. Leitchenkov, C. Leuschen, B. P. Luyendyk, K. Matsuoka, J. Mouginot, F. O. Nitsche, Y. Nogi, O. A. Nost, S. V. Popov, E. Rignot, D. M. Rippin, A. Rivera, J. Roberts, N. Ross, M. J. Siegert, A. M. Smith, D. Steinhage, M. Studinger, B. Sun, B. K. Tinto, B. C. Welch, D. Wilson, D. A. Young, C. Xiangbin, and A. Zirizzotti (2013), Bedmap2: improved ice bed, surface and thickness datasets for Antarctica, *Cryosph.*, 7, 375–393, doi:10.5194/tc-7-375-2013.

Fukamachi, Y., S. R. Rintoul, J. A. Church, S. Aoki, S. Sokolov, M. A. Rosenberg, and M. Wakatsuchi (2010), Strong export of Antarctic Bottom Water east of the Kerguelen plateau, *Nat. Geosci.*, 3, 327–331, doi:10.1038/ngeo842.

Galton-Fenzi, B., J. Hunter, R. Coleman, S. Marsland, and R. Warner (2012), Modeling the basal melting and marine ice accretion of the Amery Ice Shelf, *J. Geophys. Res. Oceans*, 117(C9).

Gaube, P., and D. J. McGillicuddy Jr. (2017), The Influence of Gulf Stream Eddies and Meanders on Near-Surface Chlorophyll, *Deep Sea Res. Pt I*, 122, 1–16.

Gaube, P., D. J. McGillicuddy, D. B. Chelton, M. J. Behrenfeld, and P. G. Strutton (2014), Regional variations in the influence of mesoscale eddies on near-surface chlorophyll, *J. Geophys. Res. C Ocean.*, 119(12), 8195–8220, doi:10.1002/2014JC010111.

Geiger, C. A., W. D. Hibler, and S. F. Ackley (1998), Large-scale sea ice drift and deformation: Comparison between models and observations in the western Weddell Sea during 1992, *J. Geophys. Res.*, 103(C10), 21,893–21,913.

Gent, P. R., and J. C. McWilliams (1990), Isopycnal Mixing in Ocean Circulation Models, *J. Phys. Oceanogr.*, 20(1), 150–155.

Gent, P. R., J. Willebrand, T. J. McDougall, and J. C. Mcwilliams (1995), Parameterizing Eddy-Induced Tracer Transports in Ocean Circulation Models, *J. Phys. Oceanogr.*, 25(4), 463–474.

- Gerringa, L., P. Laan, G. van Dijken, H. van Haren, H. De Baar, K. Arrigo, and A.-C. Alderkamp (2015), Sources of iron in the Ross Sea Polynya in early summer, *Mar. Chem.*, doi:10.1016/j.marchem.2015.06.002.
- Gille, S. T., M. M. Yale, and D. T. Sandwell (2000), Global correlation of mesoscale ocean variability with seafloor roughness from satellite altimetry, *Geophys. Res. Lett.*, 27(9), 1251–1254, doi:10.1029/1999GL007003.
- Goldberg, D., D. Holland, and C. Schoof (2009), Grounding line movement and ice shelf buttressing in marine ice sheets, *J. Geophys. Res.*, 114(F4).
- Gordon, A. L., A. H. Orsi, R. Muench, B. A. Huber, E. Zambianchi, and M. Visbeck (2009), Western Ross Sea continental slope gravity currents, *Deep Sea Res. Pt II*, 56, 796–817, doi:10.1016/j.dsr2.2008.10.037.
- Gruber, N., Z. Lachkar, H. Frenzel, P. Marchesiello, M. Münnich, J. C. McWilliams, T. Nagai, and G.-K. Plattner (2011), Eddy-induced reduction of biological production in eastern boundary upwelling systems, *Nat. Geosci.*, 4(11), 787–792, doi:10.1038/ngeo1273.
- Guan, X., H.-W. Ou, and D. Chen (2009), Tidal effect on the dense water discharge, Part 2: A numerical study, *Deep Sea Res. Pt II*, 56, 884–894, doi:10.1016/j.dsr2.2008.10.028.
- Hallberg, R. (2013), Using a resolution function to regulate parameterizations of oceanic mesoscale eddy effects, *Ocean Model.*, 72, 92–103, doi:10.1016/j.ocemod.2013.08.007.
- Halpern, B. S., S. Walbridge, K. A. Selkoe, C. V. Kappel, F. Micheli, C. D'Agrosa, J. F. Bruno, K. S. Casey, C. Ebert, H. E. Fox, R. Fujita, D. Heinemann, H. S. Lenihan, E. M. P. Madin, M. T. Perry, E. R. Selig, M. Spalding, R. Steneck, and R. Watson (2008), A Global Map of Human Impact on Marine Ecosystems, *Science*, 319(5865), 948–952, doi:10.1126/science.1149345.
- Hatta, M., C. I. Measures, P. J. Lam, D. C. Ohnemus, M. E. Auro, M. M. Grand, and K. E. Selph (2016), The relative roles of modified circumpolar deep water and benthic sources in supplying iron to the recurrent phytoplankton blooms above Pennell and Mawson Banks, Ross Sea, Antarctica, *J. Mar. Sys.*, doi:10.1016/j.jmarsys.2016.07.009.
- Hattermann, T., L. H. Smedsrød, O. a. Nøst, J. Lilly, and B. K. Galton-Fenzi (2014), Eddy-resolving simulations of the Fimbul Ice Shelf cavity circulation: Basal melting and exchange with open ocean, *Ocean Model.*, 82, 28–44, doi:10.1016/j.ocemod.2014.07.004.

- Heil, P., J. K. Hutchings, A. P. Worby, M. Johansson, J. Launiainen, C. Haas, and W. D. Hibler (2008), Tidal forcing on sea-ice drift and deformation in the western Weddell Sea in early austral summer, 2004, *Deep Sea Res. Pt II*, 55(8), 943–962.
- Holland, D. M., and A. Jenkins (1999), Modeling Thermodynamic IceOcean Interactions at the Base of an Ice Shelf, *J. Phys. Oceanogr.*, 29(8), 1787–1800.
- Holte, J., and L. Talley (2009), A New Algorithm for Finding Mixed Layer Depths with Applications to Argo Data and Subantarctic Mode Water Formation*, *J. Atmos. Ocean. Technol.*, 26, 1920–1939, doi:10.1175/2009JTECHO543.1.
- IOC, SCOR, and IAPSO (2010), The international thermodynamic equation of seawater - 2010: Calculation and use of thermodynamic properties, *Intergov. Oceanogr. Comm. Manuals Guid. No. 56*, p. 196.
- Isern-Fontanet, J., E. García-Ladona, and J. Font (2003), Identification of Marine Eddies from Altimetric Maps, *J. Atmos. Ocean. Technol.*, 20(5), 772–778.
- Jackett, D. R., and T. J. McDougall (1997), A neutral density variable for the world's oceans, *J. Phys. Oceanogr.*, (1968), 237–263.
- Jacobs, S. S., and C. F. Giulivi (2010), Large multidecadal salinity trends near the Pacific-Antarctic continental margin, *J. Clim.*, 23(17), 4508–4524, doi:10.1175/2010JCLI3284.1.
- Jacobs, S. S., A. Amos, and P. Bruchhausen (1970), Ross Sea oceanography and Antarctic bottom water formation, *Deep Sea Res.*, 17, 935–962.
- Jacobs, S. S., C. F. Giulivi, and P. a. Mele (2002), Freshening of the Ross Sea during the late 20th century., *Science*, 297, 386–9, doi:10.1126/science.1069574.
- Jacobs, S. S., A. Jenkins, C. F. Giulivi, and P. Dutrieux (2011), Stronger ocean circulation and increased melting under Pine Island Glacier ice shelf, *Nat. Geosci.*, 4(8), 519–523.
- JAXA (Japan Aerospace Exploration Agency) (2006), AMSR-E Data Users Handbook, 115 pp, March 2006 (http://www.eorc.jaxa.jp/en/hatoyama/amsr-e/amsr-e_handbook_e.pdf).
- Johnson, E. S., and M. L. van Woert (2006), Tidal currents of the Ross Sea and their time stability, *Antarct. Sci.*, 18(1), 141–154.
- Johnson, G. C., and H. L. Bryden (1989), On the size of the Antarctic Circumpolar Current, *Deep Sea Res.*, 36(1), 39–53.

- Kahru, M., B. G. Mitchell, S. T. Gille, C. D. Hewes, and O. Holm-Hansen (2007), Eddies enhance biological production in the Weddell-Scotia Confluence of the Southern Ocean, *Geophys. Res. Lett.*, 34(14), L14,603, doi:10.1029/2007GL030430.
- Kara, A. B., P. A. Rochford, and H. E. Hurlbert (2003), Mixed layer depth variability over the global ocean, *J. Geophys. Res.*, 108, doi:10.1029/2000C000736.
- Koentopp, M., O. Eisen, C. Kottmeier, L. Padman, and P. Lemke (2005), Influence of tides on sea ice in the Weddell Sea: Investigations with a high-resolution dynamic-thermodynamic sea ice model, *J. Geophys. Res. Oceans*, 110(C2).
- Kowalik, Z., and A. Y. Proshutinsky (1994), The Arctic ocean tides, *The Polar Oceans and their role in shaping the global environment*, pp. 137–158.
- Kustka, A. B., J. T. Kohut, A. E. White, P. J. Lam, A. Milligan, M. S. Dinniman, S. Mack, E. Hunter, M. R. Hiscock, W. O. Smith, and C. I. Measures (2015), The roles of MCDW and deep water iron supply in sustaining a recurrent phytoplankton bloom on central Pennell bank (Ross Sea), *Deep Sea Res. Pt I*, doi:10.1016/j.dsr.2015.08.012.
- Kwok, R., G. F. Cunningham, and W. D. Hibler (2003), Sub-daily sea ice motion and deformation from RADARSAT observations, *Geophys. Res. Lett.*, 30(23).
- Lannuzel, D., V. Schoemann, J. de Jong, B. Pasquer, P. van der Merwe, F. Masson, J.-L. Tison, and A. Bowie (2010), Distribution of dissolved iron in Antarctic sea ice: Spatial, seasonal, and inter-annual variability, *J. Geophys. Res.*, 115, G03,022, doi:10.1029/2009JG001031.
- Large, W. G., J. C. McWilliams, and S. C. Doney (1994), Oceanic vertical mixing: A review and a model with a nonlocal boundary layer parameterization, *Rev. Geophys.*, 32(4), 363–403.
- Lee, M.-M., and R. G. Williams (2000), The role of eddies in the isopycnic transfer of nutrients and their impact on biological production, *J. Mar. Res.*, 58, 895–917, doi:10.1357/002224000763485746.
- Li, Y., D. J. McGillicuddy, M. S. Dinniman, and J. M. Klinck (2017), Processes influencing formation of low-salinity high-biomass lenses near the edge of the Ross Ice Shelf, *J. Mar. Sys.*, 166, 108–119.

- Locarnini, R. (1994), Water masses and circulation in the Ross Gyre and environs, Ph.D. thesis.
- MacAyeal, D. R. (1984), Thermohaline circulation below the Ross Ice Shelf: A consequence of tidally induced vertical mixing and basal melting, *J. Geophys. Res.*, *89*(C1), 597–606, doi:10.1029/JC089iC01p00597.
- MacAyeal, D. R. (1985), Tidal rectification below the Ross Ice Shelf, Antarctica, *Antarct. Res. Ser.*, *43*, 109–132.
- MacCready, P., and S. N. Giddings (2016), The Mechanical Energy Budget of a Regional Ocean Model, *J. Phys. Oceanogr.*, *46*(9), 2719–2733, doi:10.1175/JPO-D-16-0086.1.
- Mack, S. L., L. Padman, and J. M. Klinck (2013), Extracting tidal variability of sea ice concentration from AMSR-E passive microwave single-swath data: a case study of the Ross Sea, *Geophys. Res. Lett.*, *40*(3), 547–552, doi:10.1002/grl.50128.
- Makinson, K., P. R. Holland, A. Jenkins, K. W. Nicholls, and D. M. Holland (2011), Influence of tides on melting and freezing beneath Filchner-Ronne Ice Shelf, Antarctica, *Geophys. Res. Lett.*, *38*(L06601), doi:10.1029/2010GL046462.
- Markus, T., and D. J. Cavalieri (2009), The AMSR-E NT2 sea ice concentration algorithm: Its basis and implementation, *J. Remote Sensing Soc. Japan*, *29*(1), 216–225.
- Marsay, C. M., P. N. Sedwick, M. S. Dinniman, P. M. Barrett, S. L. Mack, and D. J. McGillicuddy Jr. (2014), Estimating the benthic efflux of dissolved iron on the Ross Sea continental shelf, *Geophys. Res. Lett.*, *41*, 7576–7583.
- Martin, J. H. (1990), Glacial-interglacial CO₂ change: the iron hypothesis, *Paleoceanography*, *5*(1), 1–13.
- Martin, J. H., S. E. Fitzwater, and M. R. Gordon (1990), Iron deficiency limits phytoplankton growth in antarctic waters, *Global Biogeochem. Cycles*, *4*(1), 5–12.
- Martinson, D. G., and D. C. McKee (2012), Transport of warm Upper Circumpolar Deep Water onto the western Antarctic Peninsula continental shelf, *Ocean Sci.*, *8*, 433–442, doi:10.5194/os-8-433-2012.

- Mathiot, P., N. C. Jourdain, B. Barnier, H. Galée, J. M. Molines, J. L. Sommer, and T. Penduff (2012), Sensitivity of coastal polynyas and high-salinity shelf water production in the Ross Sea, Antarctica, to the atmospheric forcing, *Ocean Dyn.*, 62(5), 701–723.
- McDougall, T. J., and P. M. Barker (2011), Getting started with TEOS-10 and the Gibbs Seawater(GSW) oceanographic toolbox, *SCOR/IAPSO WG*, 127, 1–28.
- McGillicuddy, D., P. N. Sedwick, M. S. Dinniman, K. R. Arrigo, T. S. Bibby, B. J. W. Greenan, E. Hofmann, J. M. Klinck, W. O. Smith Jr., S. L. Mack, C. M. Marsay, B. M. Sohst, and G. L. van Dijken (2015), Iron supply and demand in an Antarctic shelf ecosystem, *Geophys. Res. Lett.*, 42, doi:10.1002/2015GL065727.
- McGillicuddy Jr., D. J. (2016), Mechanisms of Physical-Biological-Biogeochemical Interaction at the Oceanic Mesoscale, *Ann. Rev. Mar. Sci.*, 8, 13.1–13.36, doi:10.1146/annurev-marine-010814-015606.
- McWilliams, J. C. (2008), The nature and consequence of oceanic eddies, *Ocean Modeling in an Eddying Regime*, pp. 5–15.
- Moffat, C., B. Owens, and R. C. Beardsley (2009), On the characteristics of Circumpolar Deep Water intrusions to the west Antarctic Peninsula Continental Shelf, *J. Geophys. Res.*, 114, C05,017, doi:10.1029/2008JC004955.
- Moholdt, G., L. Padman, and H. A. Fricker (2014), Basal mass budget of Ross and Filchner-Ronne ice shelves, Antarctica, derived from Lagrangian analysis of ICESat altimetry, *J. Geophys. Res.*, 119(11), 2361–2380.
- Muench, R. D., A. Wåhlin, T. M. Özgökmen, R. Hallberg, and L. Padman (2009), Impacts of bottom corrugations on a dense Antarctic outflow: NW Ross Sea, *Geophys. Res. Lett.*, 36(23), L23,607, doi:10.1029/2009GL041347.
- Nansen, F. (1898), *Farthest North: Being the Record of a Voyage of Exploration of the Ship "Fram" 1893-96, and of a Fifteen Months' Sleigh Journey by Dr. Nansen and Lieut. Johansen*, George Newnes.
- Niiler, P. P. (1969), On the Ekman divergence in an oceanic jet, *J. Geophys. Res.*, 74(28), 7048, doi:10.1029/JC074i028p07048.

Nøst, O. A., M. Biuw, V. Tverberg, C. Lydersen, T. Hattermann, Q. Zhou, L. H. Smedsrød, and K. M. Kovacs (2011), Eddy overturning of the Antarctic Slope Front controls glacial melting in the Eastern Weddell Sea, *J. Geophys. Res.*, *116*, C11,014, doi: 10.1029/2011JC006965.

Ohshima, K. I., Y. Fukamachi, G. D. Williams, S. Nihashi, F. Roquet, Y. Kitade, T. Tamura, D. Hirano, L. Herráiz-Borreguero, I. C. Field, M. A. Hindell, S. Aoki, and M. Wakatsuchi (2013), Antarctic Bottom Water production by intense sea-ice formation in the Cape Darnley polynya, *Nat. Geosci.*, *6*(3), 235–240, doi:10.1038/ngeo1738.

Orsi, A. H., and C. L. Wiederwohl (2009), A recount of Ross Sea waters, *Deep Sea Res. Pt II*, *56*, 778–795, doi:10.1016/j.dsr2.2008.10.033.

Orsi, A. H., G. C. Johnson, and J. Bullister (1999), Circulation, mixing, and production of Antarctic Bottom Water, *Prog. Oceanogr.*, *43*, 55–109.

Orsi, A. H., W. M. Smethie, and J. Bullister (2002), On the total input of Antarctic waters to the deep ocean: A preliminary estimate from chlorofluorocarbon measurements, *J. Geophys. Res.*, *107*(C8), 3122.

Ou, H.-W., X. Guan, and D. Chen (2009), Tidal effect on the dense water discharge, Part 1: Analytical model, *Deep Sea Res. Pt II*, *56*, 874–883, doi:10.1016/j.dsr2.2008.10.031.

Padman, L., and C. Kottmeier (2000), High-frequency ice motion and divergence in the Weddell Sea, *J. Geophys. Res. Oceans*, *105*(C2), 3379–3400.

Padman, L., H. A. Fricker, R. Coleman, S. Howard, and L. Erofeeva (2002), A new tide model for the Antarctic ice shelves and seas, *Ann. Glaciol.*, *34*(1), 247–254.

Padman, L., S. L. Howard, A. H. Orsi, and R. D. Muench (2009), Tides of the northwestern Ross Sea and their impact on dense outflows of Antarctic Bottom Water, *Deep Sea Res. Pt II*, *56*, 818–834, doi:10.1016/j.dsr2.2008.10.026.

Parkinson, C. L. (2003), Aqua: An Earth-observing satellite mission to examine water and other climate variables, *IEEE Trans. Geosci. Remote Sens.*, *41*(2), 173–183.

Pawlowicz, R., B. Beardsley, and S. Lentz (2002), Classical tidal harmonic analysis including error estimates in MATLAB using T_TIDE, *Comput. Geosci.*, *28*(8), 929–937.

- Phillips, H. E., and S. R. Rintoul (2000), Eddy variability and energetics from direct current measurements in the Antarctic Circumpolar Current south of Australia, *J. Phys. Oceanogr.*, *30*, 3050–3076.
- Qiao, F., Y. Yuan, J. Deng, D. Dai, and Z. Song (2016), Wave-turbulence interaction-induced vertical mixing and its effects in ocean and climate models, *Phil. Trans. R. Soc. A*, *374*(2065), 20150,201.
- Rasch, P. J. (1994), Conservative Shape-Preserving Two-Dimensional Transport on a Spherical Reduced Grid, *Mon. Weather Rev.*, *122*(6), 1337–1350.
- Rignot, E., S. S. Jacobs, J. Mouginot, and B. Scheuchl (2013), Ice-shelf melting around Antarctica., *Science*, *341*(6143), 266–70, doi:10.1126/science.1235798.
- Rintoul, S., C. Hughes, and D. Olbers (2001), *The Antarctic Circumpolar Current System*, 271–301 pp., doi:10.1002/ajp.20122.
- Robertson, R., L. Padman, and G. Egbert (1998), Tides in the Weddell Sea, *Antarct. Res. Ser.*, *75*, 341–369.
- Robinson, J., E. Popova, A. Yool, M. Srokosz, R. Lampitt, and J. R. Blundell (2014), How deep is deep enough? Ocean iron fertilization and carbon sequestration in the Southern Ocean, *Geophys. Res. Lett.*, *41*, 2489–2495, doi:10.1002/2013GL058799.
- Schmidt, G. A., C. M. Bitz, U. Mikolajewicz, and L.-B. Tremblay (2004), Ice-ocean boundary conditions for coupled models, *Ocean Model.*, *7*(1-2), 59–74, doi:10.1016/S1463-5003(03)00030-1.
- Scott, R. B., and F. Wang (2005), Direct Evidence of an Oceanic Inverse Kinetic Energy Cascade from Satellite Altimetry, *J. Phys. Oceanogr.*, *35*(9), 1650–1666, doi:10.1175/JPO2771.1.
- Sedwick, P. N., G. R. DiTullio, and D. J. Mackey (2000), Iron and manganese in the Ross Sea, Antarctica: Seasonal iron limitation in Antarctic shelf waters, *J. Geophys. Res.*, *105*(C5), 11,321, doi:10.1029/2000JC000256.
- Sedwick, P. N., C. M. Marsay, B. M. Sohst, A. M. Aguilar-Islas, M. C. Lohan, M. C. Long, K. R. Arrigo, R. B. Dunbar, M. A. Saito, W. O. Smith, and G. R. DiTullio (2011), Early season depletion of dissolved iron in the Ross Sea polynya: Implications

- for iron dynamics on the Antarctic continental shelf, *J. Geophys. Res.*, *116*(C12019), doi: 10.1029/2010JC006553.
- Shchepetkin, A. F., and J. C. McWilliams (1998), Quasi-Monotone Advection Schemes Based on Explicit Locally Adaptive Dissipation, *Mon. Weather Rev.*, *126*(6), 1541–1580.
- Shchepetkin, A. F., and J. C. McWilliams (2005), The regional oceanic modeling system (ROMS): a split-explicit, free-surface, topography-following-coordinate oceanic model, *Ocean Model.*, *9*, 347–404, doi:10.1016/j.ocemod.2004.08.002.
- Smith, C., K. Richards, and M. Fasham (1996), The impact of mesoscale eddies on plankton dynamics in the upper ocean, *Deep Sea Res. Pt I*, *43*(11-12), 1807–1832, doi: 10.1016/S0967-0637(96)00035-0.
- Smith, K. S., and G. K. Vallis (2001), The scales and equilibration of midocean eddies: Freely evolving flow, *J. Phys. Oceanogr.*, *31*(2), 554–571.
- Smith, K. S., and G. K. Vallis (2002), The Scales and Equilibration of Midocean Eddies: ForcedDissipative Flow, *J. Phys. Oceanogr.*, *32*(6), 1699–1720.
- Smith, W. O., P. N. Sedwick, K. R. Arrigo, D. G. Ainley, and A. H. Orsi (2012), The Ross Sea in a Sea of Change, *Oceanography*, *25*(3), 90–103.
- Smith, W. O., M. S. Dinniman, E. E. Hofmann, and J. M. Klinck (2014), The effects of changing winds and temperatures on the oceanography of the Ross Sea in the 21st century, *Geophys. Res. Lett.*, *41*(5), 1624–1631, doi:10.1002/2014GL059311.
- Smith Jr., W. O., D. G. Ainley, and R. Cattaneo-Vietti (2007), Trophic interactions within the Ross Sea continental shelf ecosystem, *Philos. Trans. R. Soc. B*, *362*, 95–111, doi: 10.1098/rstb.2006.1956.
- Song, Y., and D. Haidvogel (1994), A semi-implicit ocean circulation model using a generalized topography-following coordinate system, *J. Comp. Phys.*, *115*(1), 228–244.
- St-Laurent, P., J. M. Klinck, and M. S. Dinniman (2013), On the Role of Coastal Troughs in the Circulation of Warm Circumpolar Deep Water on Antarctic Shelves, *J. Phys. Oceanogr.*, *43*, 51–64, doi:10.1175/JPO-D-11-0237.1.
- Stammer, D. (1998), On Eddy Characteristics, Eddy Transports, and Mean Flow Properties, *J. Phys. Oceanogr.*, *28*, 727–739.

- Stammerjohn, S. E., D. G. Martinson, R. C. Smith, X. Yuan, and D. Rind (2008), Trends in Antarctic annual sea ice retreat and advance and their relation to El NiñoSouthern Oscillation and Southern Annular Mode variability, *J. Geophys. Res.*, 113(C3), 1–20, doi:10.1029/2007JC004269.
- Stern, M. E. (1965), Interaction of a uniform wind stress with a geostrophic vortex, *Deep Sea Res.*, 12, 355–367, doi:10.1016/0011-7471(65)90007-0.
- Stewart, A. L., and A. F. Thompson (2015), Eddy-mediated transport of warm Circumpolar Deep Water across the Antarctic Shelf Break, *Geophys. Res. Lett.*, 42, 432–440, doi:10.1002/2014GL062281.1.
- Tagliabue, A., and K. R. Arrigo (2005), Iron in the Ross Sea: 1. Impact on CO₂ fluxes via variation in phytoplankton functional group and non-Redfield stoichiometry, *J. Geophys. Res. Ocean.*, 110(3), 1–15, doi:10.1029/2004JC002531.
- Thompson, A. F., and K. J. Heywood (2014), Eddy transport as a key component of the Antarctic overturning circulation, *Nat. Geosci.*, 7(December), doi:10.1038/NGEO2289.
- Vallis (2006), *Atmospheric and Oceanic Fluid Dynamics*, Cambridge University Press, Cambridge.
- Wang, Q., S. Danilov, H. Hellmer, D. Sidorenko, J. Schröter, and T. Jung (2013), Enhanced cross-shelf exchange by tides in the western Ross Sea, *Geophys. Res. Lett.*, 40(21), 5735–5739, doi:10.1002/2013GL058207.
- Whitworth, T., and A. H. Orsi (2006), Antarctic Bottom Water production and export by tides in the Ross Sea, *Geophys. Res. Lett.*, 33, L12,609, doi:10.1029/2006GL026357.
- Williams, G. D., S. Aoki, S. S. Jacobs, S. R. Rintoul, T. Tamura, and N. L. Bindoff (2010), Antarctic Bottom Water from the Adélie and George V Land coast, East Antarctica (140149E), *J. Geophys. Res.*, 115, C04,027, doi:10.1029/2009JC005812.
- Zhang, Y., J. Pedlosky, and G. R. Flierl (2011), Cross-Shelf and Out-of-Bay Transport Driven by an Open-Ocean Current, *J. Phys. Oceanogr.*, 41, 2168–2186, doi:10.1175/JPO-D-11-08.1.

APPENDIX A

ACRONYMS & VARIABLES

A.1 VARIABLES

a - Rossby radius of deformation

c - Speed

C_{ice} - Sea ice concentration

f - Coriolis parameter/frequency

g - Gravity (9.8 m s^{-2})

H - Height of the water column (positive)

h_{ice} - Sea ice thickness

N - Buoyancy frequency

S_A - Absolute Salinity

t - Time

T - Potential temperature

T_{tide} - Tide period

u, v - Velocity

V - Volume

z - Depth (negative)

Δx - Model grid spacing

Θ - Conservative Temperature

ρ - Potential density

ρ_0 - Reference potential density

ϕ - Latitude

Ω - Angular velocity of Earth

σ - Standard deviation

ζ - Relative vorticity

A.2 ACRONYMS & ABBREVIATIONS

AABW - Antarctic Bottom Water

AASW - Antarctic Surface Water

ACC - Antarctic Circumpolar Current

AMPS - Antarctic Mesoscale Prediction System

AMSR-E - Advanced Microwave Scanning Radiometer - EOS

CATS2008 - Circum-Antarctic Tidal Simulation (2008)

CCAMLR - Commission for the Conservation of Antarctic Marine Living Resources

CDW - Circumpolar Deep Water

CTD - Conductivity Temperature Depth (sensor)

dFe - Dissolved iron

DJF - December, January, and February

dye_{bdFe} - passive tracer dye for benthic dissolved iron

dye_{CDW} - passive tracer dye for CDW

dye_{GM} - passive tracer dye for Glacial Melt

$dyes_{SIM}$ - passive tracer dye for Sea Ice Melt

EKE - Eddy Kinetic Energy

HSSW - High Salinity Shelf Water

IBCSO - International Bathymetry Chart of the Southern Ocean

ISCCP - International Satellite Cloud Climatology Product

ISW - Ice Shelf Water

KE - Kinetic Energy

KPP - K-Profile Parameterization, a vertical mixing parameterization

LSSW - Low Salinity Shelf Water

MCDW - Modified Circumpolar Deep Water

MLD - Mixed Layer Depth

MPA - Marine Protected Area

MSW - Modified Shelf Water

MVP - Moving Vessel Profiler

OCCAM - Ocean Circulation and Climate Advanced Model

OW09 - *Orsi and Wiederwohl* [2009]

PRISM-RS - Processes Regulating Iron Supply at the Mesoscale - Ross Sea (project)

psu - Practical Salinity Units

RIS - Ross Ice Shelf

RMS - Root Mean Square

ROMS - Regional Ocean Modeling System

- RossTIM - Ross Tidal Inverse Model

SML - Surface Mixed Layer

SNR - Signal to Noise Ratio

SSC - Simulation Significance Criterion

SSH - Sea Surface Height

SSM/I - Special Sensor Microwave Imager

STL - Seasonal Trend using Loess [*Cleveland et al.*, 1990]

SW - Shelf Water

TEOS-10 - The Equation of State of Seawater (2010) [*IOC et al.*, 2010]

VPR - Video Plankton Recorder

APPENDIX B

GLOSSARY

B.1 OCEANOGRAPHIC TERMS

baroclinic - State of a fluid in which lines of constant density are not parallel to lines of constant pressure. Density variations cause changes in the horizontal pressure gradient with depth, causing changes in velocity.

barotropic - State of a fluid in which lines of constant density are parallel to lines of constant pressure. In this case, horizontal velocity does not vary with depth.

basal melt - Melt at the bottom of an ice shelf.

bathymetry - Topography of the ocean floor.

CTD - Refers to a conductivity (or salinity), temperature, depth sensor that typically takes a vertical profile.

frazil ice - Free floating ice crystals in the water, slush-like.

hydrostatic - Pressure at any point in the ocean is balanced by the weight of water above that point. The assumption is that vertical velocities and accelerations are small.

ice sheet - Large ice mass over land.

ice shelf - Extension of an ice sheet floating on the ocean.

polynya - Area of open water surrounded by ice.

VITA

Stefanie Lynn Mack
 Department of Ocean, Earth, & Atmospheric Sciences
 Old Dominion University
 Norfolk, VA 23529

Education

Westminster College	New Wilmington, PA, USA
<i>B.S. Physics; Mathematics minor; magna cum laude</i>	2010

Relevant Publications

- S.L. Mack**, M.S. Dinniman, D.J. McGillicuddy Jr., P.N. Sedwick, J.M. Klinck (2017), Dissolved iron transport pathways in the Ross Sea: Influence of tides and mesoscale eddies in a regional ocean model, *J. Mar. Syst.*, **166**, 73-86.
- D.J. McGillicuddy, Jr., P.N. Sedwick, M.S. Dinniman, K.R. Arrigo, T.S Bibby, B.J.W. Greenan, E.E. Hofmann, J.M. Klinck, W.O. Smith, Jr., **S.L. Mack**, C.M. Marsay, B.M. Sohst, G.L. van Dijken (2015), Iron supply and demand in an Antarctic shelf ecosystem, *Geophys. Res. Lett.*, **42**(19), 8088-8097.
- A. Kustka, J.T. Kohut, A. White, P.J. Lam, A.J. Milligan, M.S. Dinniman, **S.L. Mack**, E. Hunter, M. Hiscock, W.O. Smith, Jr., C.I. Measures (2015), The role of Modified Circumpolar Deep Water as an iron source to productive mid-summer phytoplankton in the Ross Sea, *Deep Sea Res I*, **105**, 171-185.
- C.M. Marsay, P.N. Sedwick, M.S. Dinniman, P.M. Barrett, **S.L. Mack**, D.J. McGillicuddy, Jr. (2014), Estimating the benthic efflux of dissolved iron on the Ross Sea continental shelf, *Geophys. Res. Lett.* **41**(21), 7576-7583.
- S. Mack**, L. Padman, J. Klinck (2013), Extracting tidal variability of sea ice concentration from AMSR-E passive microwave single-swath data: A case study of the Ross Sea, *Geophys. Res. Lett.* **40**(3), 547-552.